ROTOR BALANCING
of a
10 MVA SUPERCONDUCTING GENERATOR

by
WILLIAM T. TOWNSEND
B.S.M.E., NORTHEASTERN UNIVERSITY, 1982

SUBMITTED IN PARTIAL FULFILLMENT
OF THE REQUIREMENTS FOR THE
DEGREE OF
MASTER OF SCIENCE
at the
MASSACHUSETTS INSTITUTE OF TECHNOLOGY
AUGUST 1984

Signature of Autho _____
Department of Mechanical Engineering
August 10, 1984

Certified by _____
Joseph L. Smith
Thesis Supervisor

Accepted by _____
Chairman, Department Committee on Graduate Degrees

ROTOR BALANCING
OF A 10 MVA SUPERCONDUCTING GENERATOR

by
WILLIAM T. TOWNSEND

Submitted to the Department of Mechanical Engineering
on August 10, 1984, in partial fulfillment of the
requirements for the degree of
Master of Science in Mechanical Engineering

ABSTRACT

Predictions are made of the instabilities and balancing problems unique to the 10MVA rotor. A balance procedure, supporting hardware, and instrumentation are designed for extended, safe operation.

Thesis Supervisor: Dr. Joseph L. Smith, Jr.
Title: Professor of Mechanical Engineering

Acknowledgments

I am indebted to my mentor, Prof. J. L. Smith, whose input was essential to my practical and theoretical education.

In addition, I wish to acknowledge the substantial assistance of David Otten, who gave me valuable advice on circuit designs for the instrumentation.

Moreover, I wish to thank the members of the Cryogenic Engineering Laboratory for their friendship and suggestions.

Finally, I thank my parents and grandparents for their love and support.

Table of Contents

Appendices

List of Figures

List of Tables

I INTRODUCTION

I.1 BACKGROUND OF THE 10 MVA SUPERCONDUCTING GENERATOR

The history of superconducting generators began at MIT in 1968 with the successful demonstration of a rotating superconducting field winding. In 1976, MIT produced a 3 MVA superconducting generator. At this time MIT began designing a 10 MVA superconducting generator which could reliably contribute power to an electric grid. At the present time the Cryogenic Engineering Laboratory and the Electric Power Systems Engineering Laboratory at MIT have completed assembling the 10 MVA rotor. The next steps are to high-speed balance, and test the rotor. A heavy (1850-pound) flywheel will be added to the rotor for later tests to increase system inertia. Finally, the rotor-armature system driven by a gas turbine will be connected to the local electric grid.

Superconducting generators have advantages over conventional generators. They are smaller, lighter, and more efficient. These

advantages make the superconducting generator potentially more economical for large power-plants.

The 10 MVA superconducting rotor of this project is much different from conventional rotors. Generators of the past have evolved slowly. In conventional generators the same basic design is generally employed -- a single iron-forging rotor core with two or more integral poles. The 10 MVA rotor is built up from several parts (see figure I.3.1). Dynamically speaking, a built up rotor presents some beneficial possibilities and some problems. For instance, component balancing may be employed where it cannot be used for solid rotors, allowing a more accurate final balance. Unfortunately, the internal hysteresis damping which may be introduced by relative motion of the built-up parts can cause rotor-bearing system instabilities above the first critical speed. For this reason, difficulties may arise in the high-speed balance.

There are further reasons why instabilities are a potential problem in this rotor. For example, instabilities can arise in liquid filled rotors and the 10 MVA rotor has three liquid-helium reservoirs. Further, the onset of an instability from any source and the degree of resonance at critical speeds will be worsened because the rotor employs tilting pad bearings which have less damping to ground than conventional journal bearings.

This rotor also employs bearing supports with replaceable springs to trim the overall system dynamics.

I.2 REASONS FOR BALANCING

Balancing is important for the following reasons. The prevention of:

* rubs in the bearings, seals, and stator,
* support-spring failure,
* rotor structural failure,
* drive coupling misalignment due to dynamic rotor bending,
* helium coupling misalignment due to dynamic rotor bending,
* foundation damage.

The initial unbalance in the 10 MVA rotor is likely to be worse than conventional generator rotors for two reasons. First, the rotor has several assembly planes and slight misalignment is possible at each plane. Second, there is much more unmachined mass than a similar conventional rotor due to the existence of the damper winding, copper shields and baffles, and composite support tube.

In order to quantify our design goals for balancing, we tabulated the vibration magnitudes which, if exceeded would cause damage to the rotor (see table I.2.1).

TABLE I.2.1

VIBRATION LIMITS OF ROTOR-BEARING SYSTEM DEFLECTIONS

ITEM	LOCATION	CONSEQUENCE OF EXCEEDING LIMIT	LIMIT (Zero-to-peak amplitude)
Bearings	Free end	Bearing rub	5.0 mils
	Drive end	Bearing rub	8.0 mils
Seals	Free end	Seal rub	9.0 mils
	Drive end	seal rub	9.0 mils
Stator	Active section	Stator rub	197.0 mils
Springs (without flywheel)	Free end	Spring fatigue	3.5 mils
	Drive end	Spring fatigue	4.0 mils
Springs (with flywheel)	Free end	Spring fatigue	3.7 mils
	Drive end	Spring fatigue	3.1 mils
Drive coupling misalignment	Drive end	Wear	0.5 degrees
Helium coupling misalignment	Free end	Coupling seize	To be decided

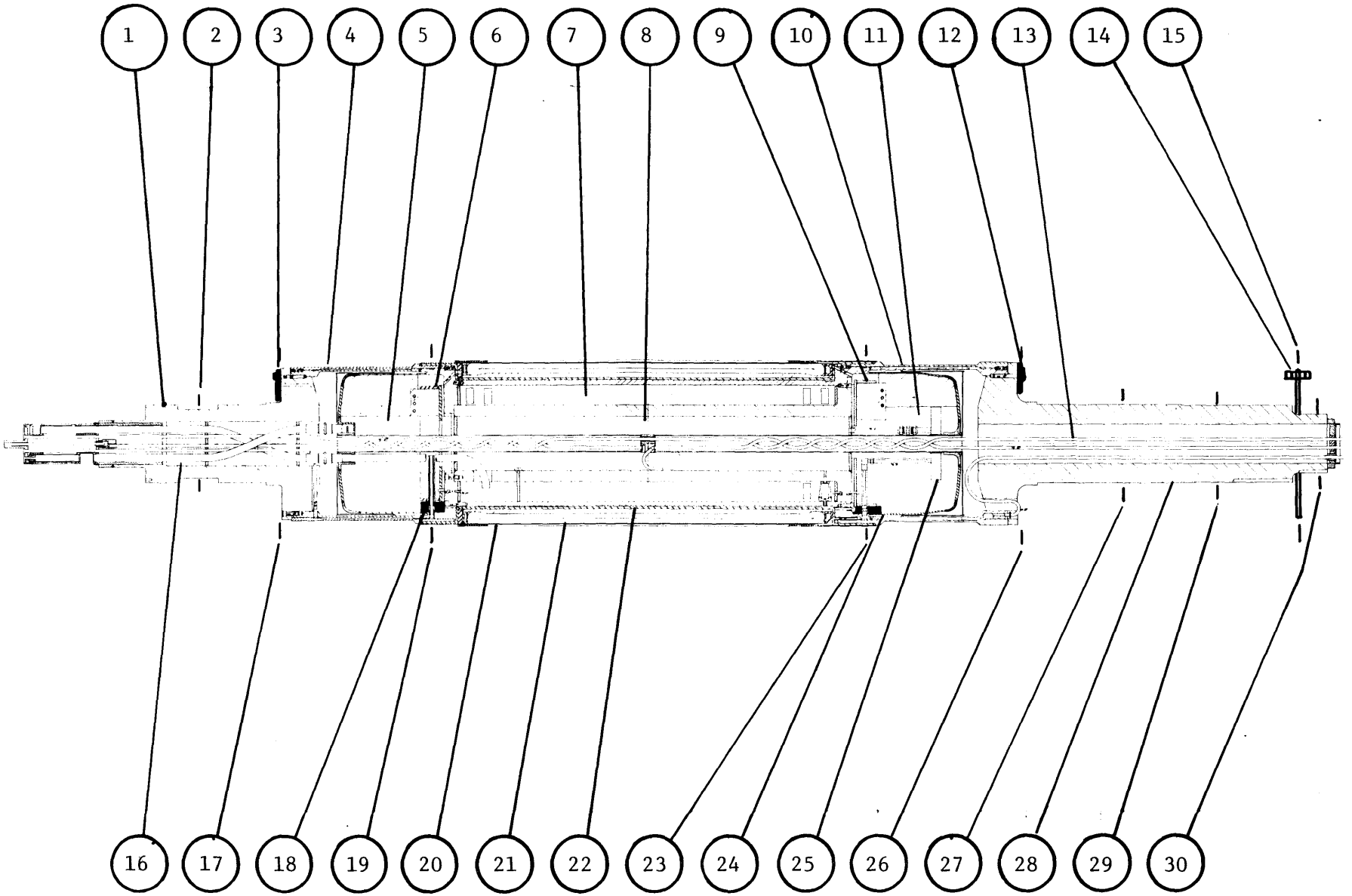

FIGURE I.3.1 ROTOR LAYOUT

TABLE I.3.2

LEGEND FOR FIGURE I.3.1

ITEM NUMBER	DESCRIPTION
1	Free End Stub Shaft
2	Free End Bearing Center-Plane, Measuring Plane a
3	Free End External Balance Weight
4	Free End Torque Tube
5	Free End Helium Reservoir
6	Free End Copper Heat Exchanger
7	Field Winding and Location of Balance Weights for Static Balance
8	Central Helium Reservoir
9	Drive End Heat Exchanger
10	Drive End Torque Tube
11	Drive End Helium Reservoir
12	Drive End External Balance Weight
13	Helium Tubes
14	Third Plane Balance Weight
15	Balance Plane III
16	Helium Tubes Supporting Field Winding Leads
17	Balance Plane I
18	Free End Internal Balance Weight
19	Balance Plane A
20	Wound Stainless-Steel Fiber/Epoxy Support Tube
21	Wound Copper Damper Winding
22	Copper Can Shield
23	Balance Plane B
24	Drive End Internal Balance Weight
25	Check Valve with Moving Plate
26	Balancing Plane II
27	Drive End Bearing Center-Plane, Measuring Plane b
28	Drive End Stub Shaft
29	Flywheel Center-Plane
30	Measuring Plane c

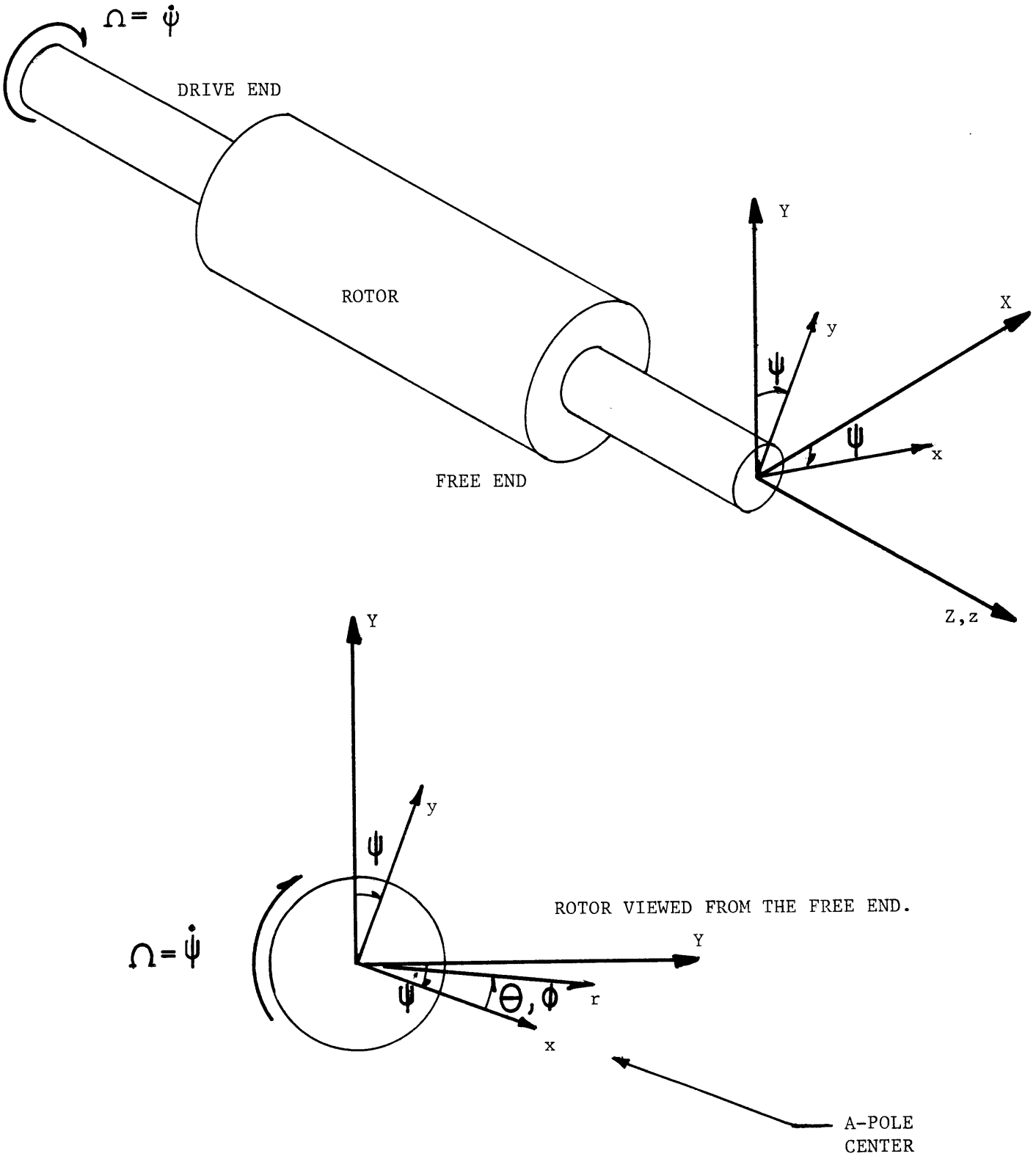

FIGURE I.3.2 COORDINATE CONVENTIONS

I.3 ROTOR LAYOUT

The rotor layout is shown in figure I.3.1. This scale drawing of the rotor identifies the important balancing and measuring planes as well as rotor components which are significant to rotor balancing.

Coordinate systems to be referenced in this thesis are indicated in figure I.3.2. The X-Y-Z axes form a right-handed stationary coordinate system. The X- and Z-axes are parallel to the horizontal direction. The Z-axis points from the drive end to the free end and passes through the static center of the bearings. The Y-axis points upward. The x-y-z axes form a right-handed coordinate system that rotates with the rotor. The x-axis passes through the A-pole and the z-axis is parallel to the Z-axis.

To describe the angular position of an arbitrary vector, $\vec{r}$, rotating with the rotor, we use a phase lag, ϕ , measured against rotation from the A-pole. The rotation of the rotor is always in the negative Z-direction (counter-clockwise when viewing the rotor from the free end).

II SOURCE OF ROTOR VIBRATION

II.1 INTRODUCTION

Rotor vibrations have many sources. The primary source of rotor vibration is mass unbalance. It is impossible to completely eliminate mass unbalance in a rotor due to machining and assembly tolerances. The unbalance in a rotor must be reduced though to the point where the vibrations and induced stresses are below given limits for the range of rotor operating speeds.

The list of other sources of vibration (those sources not directly the result of mass unbalance) in the literature grows continuously as rotor designs continue to change. Some sources are less known and some are less important. In a given rotor many of these sources simply do not exist. A list of sources relevant to the 10 MVA rotor is presented

and discussed in section II.3 while the contents of section II.2 focus on the fundamental vibration due to mass unbalance.

II.2 UNBALANCE

II.2.1 DEFINITION OF UNBALANCE

Mass unbalance is said to exist when at any section along the rotor the mass center of that section does not coincide with the bearing to bearing center line. The rotor has an infinity of orthogonal mode shapes occurring at an infinity of critical speeds. By concerning ourselves with only the modes up to and near the operating speed, we should be able to reduce the vibration caused by unbalance to an acceptable level [36].

II.2.2 MODELS USED FOR BALANCING

The most general model developed for the 10 MVA rotor-bearing design and balancing is a finite element model used in conjunction with ADINA, a finite element program which solves the eigenvalue problem and determines the mode shapes and critical speeds. With this information the number and location of balancing and measuring planes can be selected and the balancing method can be designed.

Jeff Simpson's thesis [40:pp21-40] outlines how each element of the 85 node rotor-bearing system is modeled. Each element is assigned a given stiffness and mass. ADINA assumes that the system is linear and that the matrix elements are constant. Since the rotor with a flywheel will have variable stiffness which is a function of rotor speed, mode shapes and undamped critical speeds are corrected for specific speeds by modeling the angular stiffness of the flywheel angular momentum as a torsional spring. The ADINA model though assumes no damping. Therefore, it cannot be used to quantify the magnitude of a damped vibration or to predict rotor instability. This model limitation is discussed in the next section.

The first two mode shapes and critical speeds for the cases of the rotor with and without the flywheel show relatively large deflections in the rotor supports and small bending deflections along the rotor itself.

The first mode is essentially a rigid rotor shaking on compliant supports, and the second mode may be modeled as a rigid rotor rocking on its supports.

These approximate rigid rotor models simplify balancing in the first two modes when modal balancing is used and are an aid to understanding when the influence coefficient balance method is used. A simple two plane dynamic balance will eliminate the excitation of these modes and reduce vibrations at the first two rotor resonances.

Using the rocking and shaking models we can excite either mode separately. Exciting a mode and observing rotor response in the form of a Bode plot below resonance can help us estimate damping for that mode.

$$F = m \cdot e\{[\frac{\Omega^2 - \omega_n^2 (1 - 2\xi^2)}{\omega_n^2}]^2 + 4\xi^2(1 - \xi^2)\} \quad , \qquad \text{(II.2.1)}$$

where,

F = unbalance induced force,
m = unbalance mass,
e = distance between bearing/bearing centerline and mass center,
ξ = damping ratio for a given mode
Ω = rotor rotation speed
ω_n = critical speed.

Since we know that the excitation force is a square function of speed, the before resonance slope of the log-magnitude Bode plot is 40 decibels per decade. To this may be added the predicted resonant peak vibration, M_r, from a standard Bode plot [33:p386] which is a function of the estimated damping in a given mode.

$$M_r = \frac{|F(j\Omega)|}{m \cdot e} = \frac{1}{2\xi^2\sqrt{1 - \xi^2}} \qquad \text{(II.2.2)}$$

From the resulting log-magnitude plots we have an estimation of the resonance vibration level as a function of existing unbalance. This estimation lets us know apriori whether we can pass through a given resonance without rotor damage.

The third mode is the first mode above the operation speed. Since the ADINA model predicts an increased degree of rotor flexing in the third mode, we may need to extend the simplified rigid rotor model to include flexing. The mode for this case is approximated by a bent rotor.

The rotor vibration running at an arbitrary speed below the third critical speed may be viewed as a superposition of the shaking, rocking, and bent modes. If our model is adequate then balancing in three planes will be adequate.

II.2.3 NON-LINEAR AND VARIABLE COEFFICIENT EFFECTS IN THE UNBALANCE RESPONSE

The ADINA model assumes that rotor vibrations are described by the eigenvalue equation.

$$[m]\{\ddot{x}\} + [k]\{x\} = 0 \quad , \qquad \text{(II.2.3)}$$

where,

$[m]$ = mass matrix,

$[k]$ = stiffness matrix,

$\{x\}$ = nodal deflection matrix.

This equation is linear. Further, as mentioned in the previous subsection, ADINA assumes that the coefficient matrices are constant. Therefore, sources of non-linearities and varying coefficients may affect balancing in a manner which the ADINA model does not predict. The two largest sources of non-linearities are:

1) loose or moving parts,
2) non-linear damping and stiffness of the bearing.

The only moving part in the rotor is the one-pound check valve plate which moves axially 0.25 inches maximum if there is a fault transient. This effect of moving a one-pound plate 0.25 inches axially is negligible in a 3200-pound, 12-foot rotor.

Some components within the rotor are allowed to flex. An example of this type of component are the helium tubes which flex between supports. The maximum deflection of the helium tubes is calculated in Appendix D.1. These relatively low mass tubes are expected to deflect on the order of 5 mils between supports at 3600 RPM [10:p128]. Since these light-weight-tubes are designed for symmetric changes, the

resulting unbalance is negligible. Other deflections in the 10 MVA rotor are considered to be of second order as well due to symmetry.

It has been found in practice at the General Electric Co. generator assembly plant in Lynn, Massachusetts that at overspeed the large centrifugal forces occasionally cause limited yielding in the field winding. Since the yokes in the 10 MVA rotor were designed to allow no such yielding, we do not expect this problem. However, at high speeds the dynamic rotor characteristics will be monitored carefully to determine net changes in rotor dynamics which indicate yielding.

Non-linearity in the bearings is a major source of system non-linearity. Damping and stiffness in the bearings are highly non-linear [31,32] and are functions of many factors such as oil viscosity. It is therefore difficult to make generalizations about bearing characteristics. It is known from experiments, such as those performed by Dr. E. J. Gunter at the University of Virginia [17], that vibration amplitudes in the bearings are confined to be within a given limit cycle due to bearing non-linearities. The limit is caused by spring hardening at large rotor/bearing deflection amplitudes. At intermediate amplitudes the bearing could also be spring softening. Non-linear stiffness has the effect of making the magnitude-versus-speed curve different for an accelerating and decelerating rotor. The explanation for this difference is included in most literature on vibration [6:pp40-4, 14:pp370-9, 30] and is not repeated here.

The primary sources of varying coefficients in the eigenvalue differential equation are:

* gyroscopic effects--a function of rotor speed,
* unequal rotating stiffness--a function of rotor angle.

Gyroscopic effects were discussed in the previous sub-section and become significant only after the flywheel is added to the rotor. Provisions for balancing with the flywheel attached are given in sub-section III.7.4.

Unequal rotating stiffness appears as a varying stiffness in stationary coordinates. Unequal rotating stiffness is a source of double frequency, asynchronous vibration, and is usually present in generator rotors which have non-symmetric stiffness due to the poles. This vibration source is described further in section II.3.

II.3 OTHER VIBRATIONS

There are several sources of rotor vibration other than unbalance. Many sources originate from self-excitations, or instabilities, where the vibration is self-sustaining. Other sources are due to "secondary" effects such as uneven rotor stiffnesses. A list of vibration sources

in various rotor-bearing systems follows:

* oil whirl and windage whirl,
* hysteretic rotor damping,
* entrapped rotating fluid,
* bearing misalignment,
* asymmetric support stiffness,
* asymmetric shaft stiffness,
* gravity effect.

A brief description of each mechanism and its significance to the 10 MVA rotor is given later in this section.

One generalization may be made at this point. Second order systems such as the 10 MVA rotor (which is second order with respect to each of its modes) cannot become unstable if the mass, stiffness, and damping are positive. The general equation of motion for this system is,

$$[m]\{\ddot{x}\} + [c]\{\dot{x}\} + [k]\{x\} = 0 \quad , \qquad \text{(II.3.1)}$$

where,

[c] = damping matrix.

According to the Routh stability criteria [33:pp252-8] if all of the coefficients in a second order system have the same sign, then the system is stable. The mass and stiffness for this system are always positive. A situation can arise, however, where the damping is negative. "Negative damping" is technical shorthand for a mechanism

which couples the whirl motion to another motion in such a way that the whirl motion is driven proportional to the degree of coupling. In this case, the instability is driven by the damping. Damping may couple the kinetic rotor spin energy to an unstable whirl. This coupling is dangerous because the maximum potential energy in the form of elastic strain which can be stored in a whirl motion without destroying the rotor is orders of magnitude less than the available rotational kinetic energy of the rotor [12].

Generally, in order to drive an instability, the spin or rotation speed of the rotor must be faster than the natural whirl modes which orbit at the natural frequencies of the rotor-bearing system. This fact means that instabilities do not occur unless the rotor rotates supercritically. System damping to ground cannot drive an unstable whirl. In fact, when the damping to ground which retards unstable whirl dissipates more energy than the energy channeled to the instability by the rotor spin, the system will be stable [7]. Therefore, two solutions are available to eliminate a given instability. The first is to remove or diminish the mechanism which causes the whirl. The second is to add system damping relative to ground. Examples of adding positive damping to the system include the use of squeeze film dampers [18] and the use of active dampers [39].

Many of the vibration sources listed at the beginning of this section are the result of unstable whirl. Oil whirl and windage whirl are instabilities caused by negative viscous damping. The whirl occurs at one-half of the rotation speed and does not become unstable until the

operating speed reaches at least twice the natural frequency of the rotor [9, 12, 15:pp295-9, 17]. Windage whirl is rare. The windage friction on this rotor is negligible since the active section rotates within a vacuum. Oil whirl is a hydrodynamic mechanism predicted and sometimes found in rotor-bearing systems with plain journal bearings.

Tilting pad bearings were used in place of plain journal bearings in the 10 MVA rotor. Tilting pad bearings break up the instability mechanism. No literature could be found which documented an oil whirl when these bearings were used.

Hysteretic rotor damping is another negative damping phenomenon which couples the rotor spin to an unstable whirl. The calculation of the magnitude of this damping is done by integrating around the hysteresis loop [7]. The numerical calculation is almost impossible in a complicated build-up rotor such as the 10 MVA rotor because the rotor friction is so hard to quantify.

Entrapped rotating fluid is a negative damping phenomenon. This source is examined since our rotor uses liquid helium as a coolant. A calculation developed by Dr. J. A. Wolf [47] applied to the 10 MVA rotor determines at what operating speed this instability might occur (see Appendix D.2). The range of instability is from 3170 RPM to 3190 RPM. To determine if an instability will actually occur, we need to know the system damping which is very difficult to calculate. However, the probability that an instability will occur is proportional to the fluid mass which, in the case of helium, is very small.

Bearing misalignment can cause yet another negative damping unstable whirl. The instability generally occurs when a poorly lubricated thrust bearing, journal bearing, or sliding seal rubs the rotor. Usually the rub is caused by gross misalignment which we have been careful to avoid through careful bearing alignment and the use of tilting bearings. J. P. Den Hartog [15:pp293-4] gives a good intuitive explanation of the mechanism involved.

Gravity effect is a double-operating-frequency vibration induced in horizontally mounted rotors. Since the unbalanced rotor whirls about the rotation center with orbit radius, e, gravity will alternately accelerate and decelerate the rotor during each full cycle. The effect is a vertical sinusoidally varying force at the bearings equal to the mass times acceleration of the rotor,

$$F = \frac{W}{2} \left(\frac{e}{\rho} \right)^2 \sin(2\Omega t), \qquad \text{(II.3.2)}$$

where,

W = rotor weight,

ρ = radius of gyration of the rotor.

Vibration induced as a result of asymmetric shaft stiffness (not "gravity effect") is also partly due to gravity and is only seen in horizontally mounted shafts [15:p248]. By "asymmetric shaft stiffness" we mean a shaft stiffness which is different for different principle axes perpendicular to the rotor axis. If the stiffness, as seen from a stationary reference, has two maximums and two minimums for each shaft rotation (as is the case with our two pole rotor), then the rotor will

vibrate at twice the operating frequency. The rotor will also experience a resonance at half the normal unbalance resonance. The force is sinusoidally varying.

$$F = W\left(\frac{\Delta k}{k}\right) \sin(2\Omega t) \quad , \tag{II.3.3}$$

where,

Δk = amplitude of varying stiffness,

k = average stiffness.

Since,

$$\frac{\Delta k}{k} \cong \frac{e}{\rho} \cong (0.001), \tag{II.3.4}$$

$$\frac{\Delta k}{k} >> \left(\frac{e}{\rho}\right)^2 \quad . \tag{II.3.5}$$

and, therefore if we compare II.3.3 and II.3.4, we see that the gravity effect is negligible compared to the variable stiffness effect.

Asymmetrical support stiffness can cause reversing stress in the rotor as well as doubling the number of critical speeds. If the horizontal and vertical stiffnesses are spread far apart, then the rotor may experience reverse whirl between the two resonances. The bearing housing supports were designed so that the combined rotor/bearing-and-bearing/ground stiffness would be equal in the horizontal and vertical directions. We therefore expect that this source of reversing stress in the rotor will be minimal.

Constrained lateral vibration occurs when the situation in figure II.3.1 arises. This is the case with the helium tubes in the rotor. These tubes can be thought of as having their own natural frequency independent of the rotor natural frequency. Crandall proves [12] that the arrangement of figure II.3.1 is unstable at supercritical speeds due to the imposed constraint. Therefore, the tubes will become unstable in their own supercritical range. The result is that the tubes must be designed to operate subcritically only. In Appendix D.1 the calculated rotor speed for instability threshold of the worst case helium tube is 50,000 RPM. Therefore, the tubes remain stable at all normal rotor operating speeds.

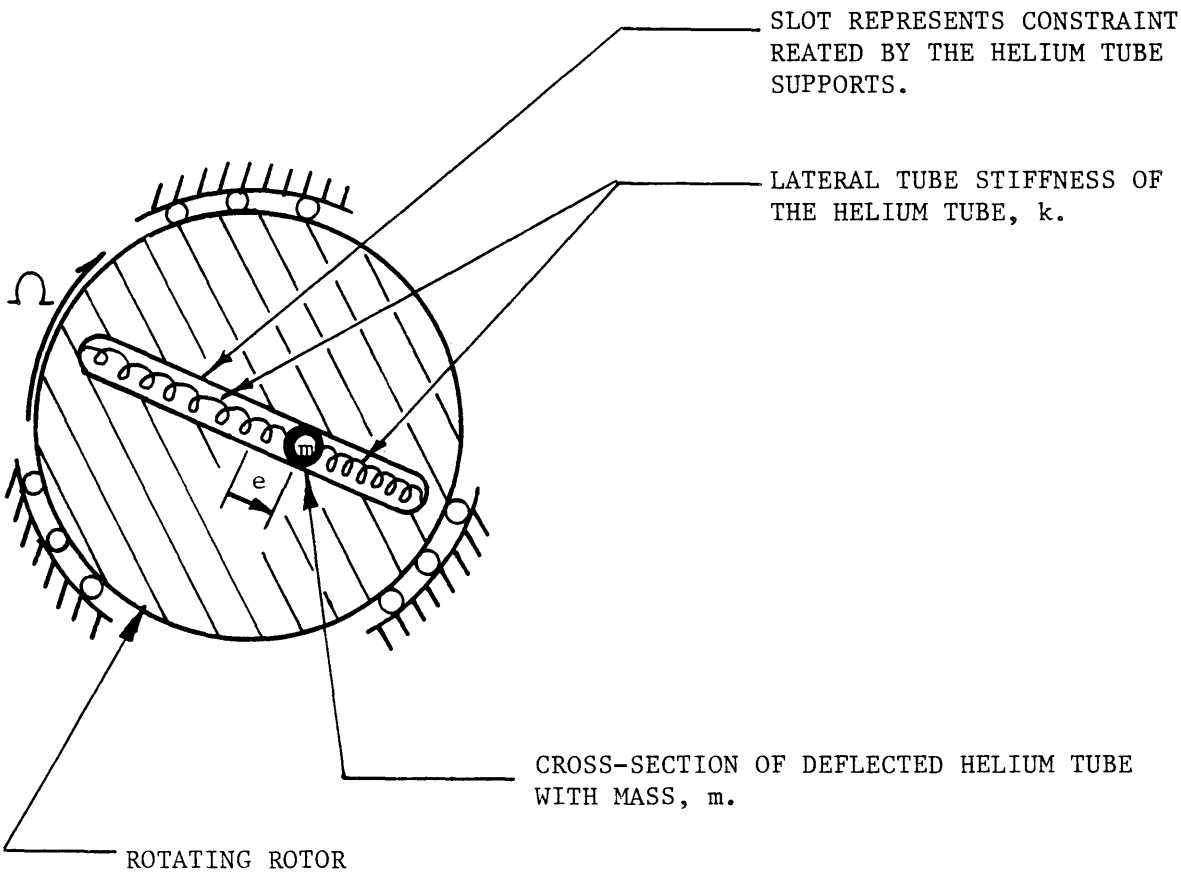

FIGURE II.3.1 MODEL OF A HELIUM TUBE AS A CONSTRAINED ROTATING MASS

III DESIGN OF A BALANCE PROCEDURE

III.1 INTRODUCTION

In order for the rotor to be used as a part of the generator to produce electric power, it must behave well dynamically at all speeds from initial standstill to overspeed (4140 RPM). Poor dynamic operation may cause damage to some part of the system. Generally, several aspects of dynamic operation must be studied. For instance, the turbine-generator system must be torsionally stable. The overall system of many generators connected by a large electric grid must be stable [19]. The rotor-bearing system must be stable and experience limited lateral motion, resulting from rotor unbalance or other disturbances. Optimization of these rotor dynamics began with the initial rotor designs and has been a criterion at all stages of design and construction.

In this chapter we are concerned with balancing. In order to complete the rotor balance it must be turned at supercritical speeds (sub-section III.5.3). In doing so rotor instability becomes a possibility as discussed in section II.3. Therefore, balancing must include methods for detecting and eliminating instabilities.

As stated in sub-section II.2.1, balancing is the process of keeping the axial mass center line collinear with the bearing/bearing center line. If, at each infinitesimal slice of the rotor along its axis, the mass center coincides and remains coincident with the bearing/bearing center line, then by definition the rotor is balanced at all speeds. Because of manufacturing tolerances the rotor can never be completely balanced. As a result, at each infinitesimal section perpendicular to the rotor axis, the center of mass, dm, will be removed from the bearing/bearing center line by a distance of $\vec{e}(z)$. If the rotor and rotor supports are infinitely stiff, then at a rotational speed, Ω , an outward pointing radial force,

$$\vec{dF}(z) = \Omega^2 \vec{e}(z) dm \quad , \qquad \text{(III.1.1)}$$

will rotate with the rotor. We may sum these infinitesimal forces through integration in orthogonal (i.e.-- x and y) directions along the rotor. The forces can be described by vectors or complex quantities. We choose the x-y rotating reference frame whose origin is at the center of rotation and let a real x-axis be the radius attached to the rotor at the A-pole. The imaginary y-axis will then be 90 degrees against

rotation or lagging the A-pole. See figure I.3.2 for the coordinate conventions. If flexibilities are allowed in the system model then the rotor will deflect into mode shapes when excited by these rotating forces.

Rotor unbalance therefore may cause bending of the rotor and cyclic forces at the bearings and bearing supports. In order to eliminate unbalance it is necessary to bring each infinitesimal mass coincident with the center of rotation. Obviously, one must approximate the balancing process until the vibration and bending levels are below acceptable limits. The models introduced in sub-section II.2.2 and others developed earlier [26, 40] are used to achieve an acceptably balanced rotor. In each model we iteratively perturb the rotor-bearing system.

The balancing procedure can be broken into five stages which will be discussed in the next sections. These five stages are:

1) initial design,
2) component balance,
3) low-speed balance,
4) high-speed balance,
5) post balance monitoring.

III.2 INITIAL ROTOR DESIGN

III.2.1 DESIGN SYMMETRY

It is standard practice to make most of the rotating parts axisymmetric. Some parts, such as the pole windings cannot be axisymmetric, although they are nearly diametrically symmetric in order to maintain mass balance. There are several reasons for axisymmetric design. One reason is manufacturing ease. Another reason is that the centrifugal load creates only hydrostatic stress similar to axisymmetric pressure vessel designs which eliminate closed shell bending moments. Another reason for making axisymmetric parts, however, is to eliminate a double frequency rotor vibration as defined in sub-section II.2.3. This phenomenon is due to asymmetric stiffness in the rotor. From the results of the low-speed balance tests we found this vibration, the non-resonant magnitude of which is independent of speed, to be approximately 0.03 mils zero-to-peak measured from ground to the bearing housing.

Gross thermal asymmetries could also cause unbalance in a rotor design which allowed large diametric temperature differences. If, for instance, one pole of the rotor were warm while the other was cold, the rotor would contract unevenly at cool-down. The difference in

temperature induced strain (0.25 inches) would cause the rotor to bow out between the bearings thus creating a mass unbalance. The 10 MVA rotor was designed to be thermally axisymmetric. Furthermore, near absolute-zero temperatures the coefficient of heat expansion for stainless steel is almost zero. Therefore, small diametric temperature asymmetries on the order of 0.1 degrees Kelvin should have a negligible effect on mass unbalance.

III.2.2 BEARING AND DRIVE ALIGNMENT

As discussed in sub-section II.2.3, the system components must be aligned. Alignment is necessary for two reasons. First, if components rub because of misalignment, rubbing may drive a self-excitation. Second, if the rotor is not aligned with the axis of the spin motor shaft which supplies torque to the rotor for balancing (section IV.1), then a force and moment will be transmitted to the drive end of the rotor shaft.

The bearings and balancing spin motor were all aligned with respect to the prime mover. Using a taut wire for alignment, the bearings, bearing supports, and spin motor mounting foot were pinned in their proper positions. The error of alignment was reported to be 10 mils maximum deviation radially. The calculations estimating the

maximum bending moment and shear transmitted from the torque source to the drive end of the rotor are presented in Appendix A.

III.2.3 TILTING PAD BEARINGS

Many times with large rotors such as the 10 MVA rotor a self-excited vibration phenomenon known as oil whirl occurs. This phenomenon is common in plain journal bearings above the first critical speed and appears as an asynchronous vibration. Tilting-pad journal bearings do not exhibit this problem. Although more expensive, they are valuable in eliminating oil whirl, a possible source of asynchronous vibration.

A side effect to using tilting pad journal bearings is that they generally have less damping than plain journal bearings [31, 32]. Less damping has two consequences. The first is that the rotor can be operated with a higher efficiency. Unfortunately, the second consequence is higher vibration levels for a given dynamic unbalance at resonance; and a greater probability that the rotor will experience a given supercritical instability other than oil whirl (sub-section II.2.3).

III.2.4 VIBRATION OF ROTOR COMPONENTS

A rotor component which is not integrally attached to the rest of the rotor may vibrate at its own natural frequency. An example of this phenomenon was investigated by G. J. Shevchuk [41]. At operating speed the 3 MVA superconducting rotor at MIT experienced large vibrations. The vibration was unexpected since its frequency was not near an expected critical frequency of the rotor. A separate shell within the 3 MVA rotor but with its own vibration mode had been excited by asynchronous armature fields. This vibration is avoided though in the design of the 10 MVA rotor by attaching all major rotor components stiffly. In the 10 MVA rotor, the stiffness and mass matrices of the ADINA model were not set up to predict the vibration of rotor components with separate structural modes; but, if the problem does occur, we can alter the model in order to aid in the elimination of the vibration.

III.2.5 CRITICAL SPEED ESTIMATION AND BEARING SUPPORT REDESIGN

The design of flexible supports for the rotor bearings is a good example of the iterative sequence in the design stages. The rotor was designed to the point where the stiffness and mass matrices could be calculated for a finite element model. Next, the first rotor critical speeds were estimated. It was found that for the present rotor in journal bearings the first critical speed would occur near the operating speed of 3600 RPM. A small unbalance would therefore cause large vibrations. If the rotor were made stiffer, it would not experience any critical speeds and avoid resonance and supercritical instabilities. Unfortunately, the rotor and supports were already very stiff designs. To make either stiffer would have been prohibitive.

Another possible design action was to make the rotor and support system less stiff and thereby move critical speeds downward below the operating speed [40]. Beam-like springs, therefore, were added between the bearing and ground. The springs were tuned with different horizontal and vertical stiffnesses so that the combined bearing oil film compliance and spring compliance could be added to give identical critical speeds in the vertical and horizontal directions. This design reduced the number of rotor critical speeds by one-half. Also the additional support compliance makes the rotor appear more rigid in the

first two modes and thereby allows us to use rigid rotor dynamic balancing for the first two modes.

A large gap between critical speeds was placed around the operating speed by allowing the rotor to become supercritical. Two critical speeds were placed below the operating speed at 2000 RPM and 2700 RPM while the next highest was at 5800 RPM. A second set of springs was also designed for use with the flywheel attached. The critical speeds predicted for the rotor with the flywheel were almost identical to those without.

III.3 COMPONENT BALANCE

Before assembly, the 10 MVA rotor was component balanced. In component balancing the parts may be balanced dynamically (or statically if the parts are very short axially). The assembled rotor would theoretically have all of its mass centers collinear with the bearing/bearing center line. The difficulty with applying this method is that assembly tolerances allow the geometrical center line to deviate from the bearing/bearing center line.

The following method was employed on the 10 MVA rotor to component balance most of the heavy parts. The carefully machined parts such as

the stub shafts, which had strict machining tolerances, were considered to have small unbalance compared to unmachined parts of the rotor. Other parts such as the field and damper windings had relatively gross irregularities. Since nearly all of the unmachined, heavy mass was in the short active section, it was deemed necessary to balance this section separately as a component. At this early stage in assembly it would have been difficult to balance this section dynamically in bearings at even a low speed of a few hundred RPM. Instead an estimation was made of the probable unbalance distribution along that section. The result of our estimation was that the highest probability of unbalance was in the winding ends.

Referring to figure III.3.1 one can see areas between the ends of the poles where there are free spokes. These spokes are one quarter of an inch in diameter with 2.065 inches of radial length between the inner and outer support tubes. With over half an inch clearance around most of the free spokes, we had ample room for balance weights. The weights were bored into assorted lengths from one-inch round bar stock. Then one quarter inch holes were cut axially through the center of these pieces so that they could be slipped over the spokes. Any weight to be attached permanently could be tack welded to the spoke to keep it from sliding after installation.

The static balance (effectively a rail balance) was performed by placing a two-inch diameter round bar through the center of the inner support tube. On the bar were mounted two ball bearing assemblies. The rotor was allowed to rotate freely. The bar was supported horizontally

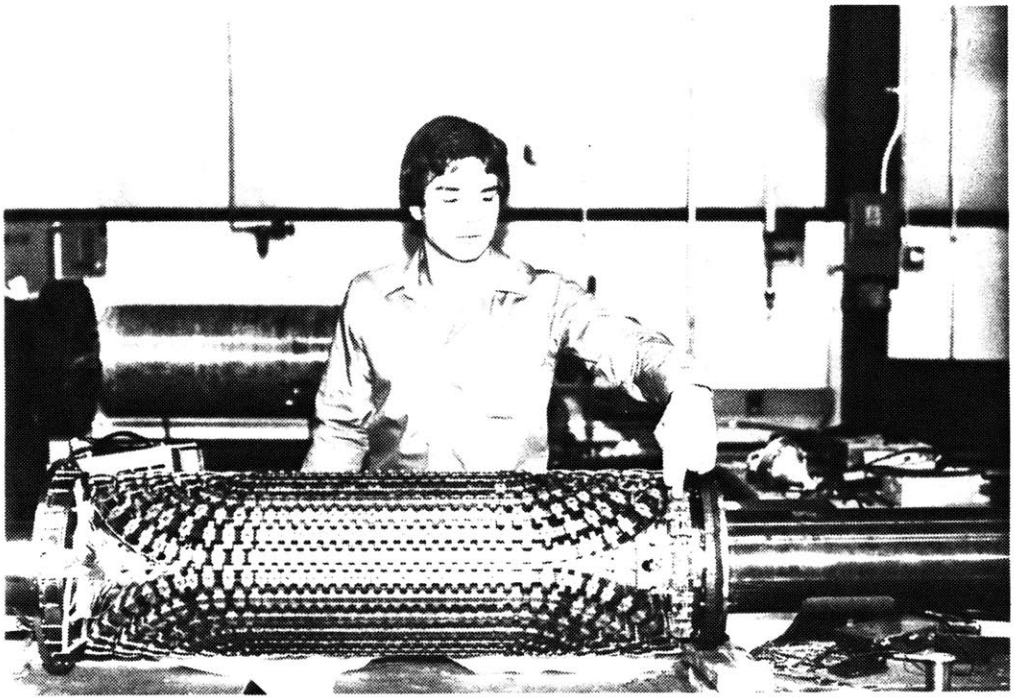

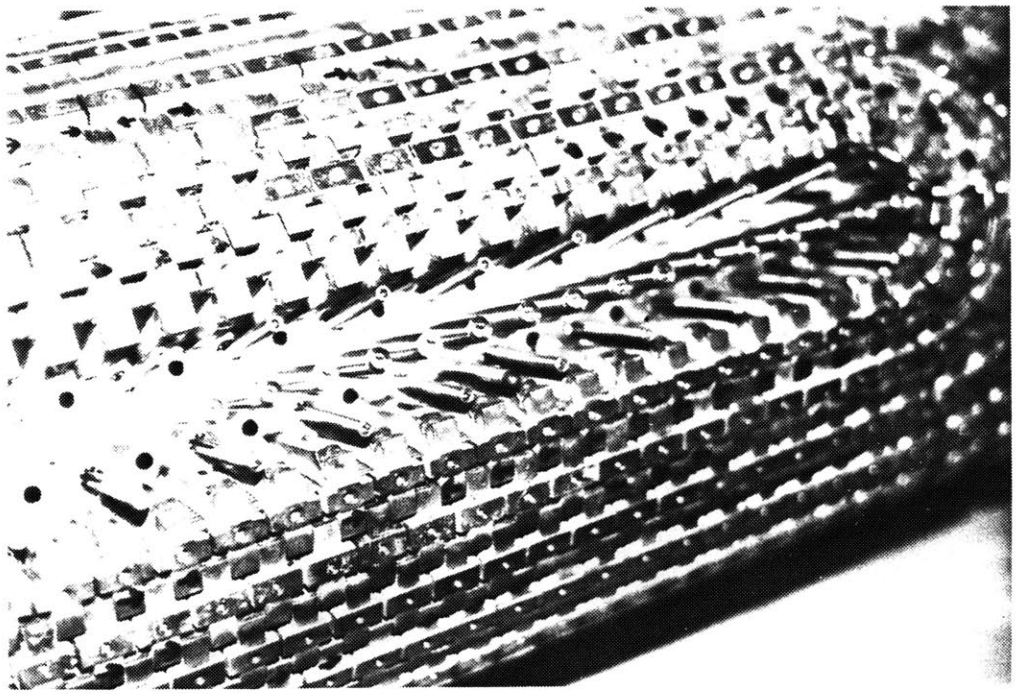

FIGURE III.3.1 SPOKE LOCATIONS FOR STATIC BALANCE WEIGHTS

on blocks. Weights were added to the spokes until the rotor component reached indifferent equilibrium. The unbalance measured in this way was so small (0.73 inch-pounds) that it was considered negligible compared to other parts of the rotor which would not be component balanced. We decided to add no balance weights.

III.4 LOW-SPEED BALANCE

III.4.1 INTRODUCTION

In the low-speed balance the rotor was turned in its bearings at speeds up to 1000 RPM. Since the first and second resonances occur at 2000 RPM and 2700 RPM respectively, it was unlikely that excessive vibration would occur due to a resonance. The first two modes resemble shaking and rocking modes (sub-section II.2.2) with relatively little rotor flexing. Therefore, we decided to model the system as a rigid rotor mounted on two springs. In essence we planned a dynamic balance where only shaking and rocking modes are examined. These approximation modes and related notation are shown in figure III.4.1. We have modeled the distributed unbalance, e(z)m(z), as being lumped into balancing planes I and II. The shaking mode is caused by a rotating force,

$$F = (m_1 r_1 + m_2 r_2)\Omega^2 = (k_1 + k_2)x \qquad \text{(III.4.1)}$$

and is commonly excited by an initially bowed rotor. The rocking mode is excited by a rotating moment

$$n = (m_3 r_3 \ell_1 + m_4 r_4 \ell_2)\Omega = k_1 x_1 L_{LB} + k_2 x_2 L_{RB} \qquad \text{(III.4.2)}$$

The summation of these modal unbalances were found by the method used in sub-section III.4.2. Correcting balance weights were then added to the rotor 180 degrees away from the unbalance locations in the end planes, I and II, of the active section.

Unfortunately, the true unbalance is not lumped conveniently at two end planes but is distributed along the rotor. This fact is of no consequence at low speeds but at high speeds the distribution may excite a bending mode as shown in figure III.4.2. A bending moment is created in this case.

$$M_B = m_1 e_1 \Omega^2 \ell = m_2 e_2 \Omega^2 \ell_2 \quad , \qquad \text{(III.4.3)}$$

where,

M_B = bending moment .

Figure III.4.2 approximates the mode shape in the third mode of our rotor. The major mass of the rotor is in the stub shafts and the

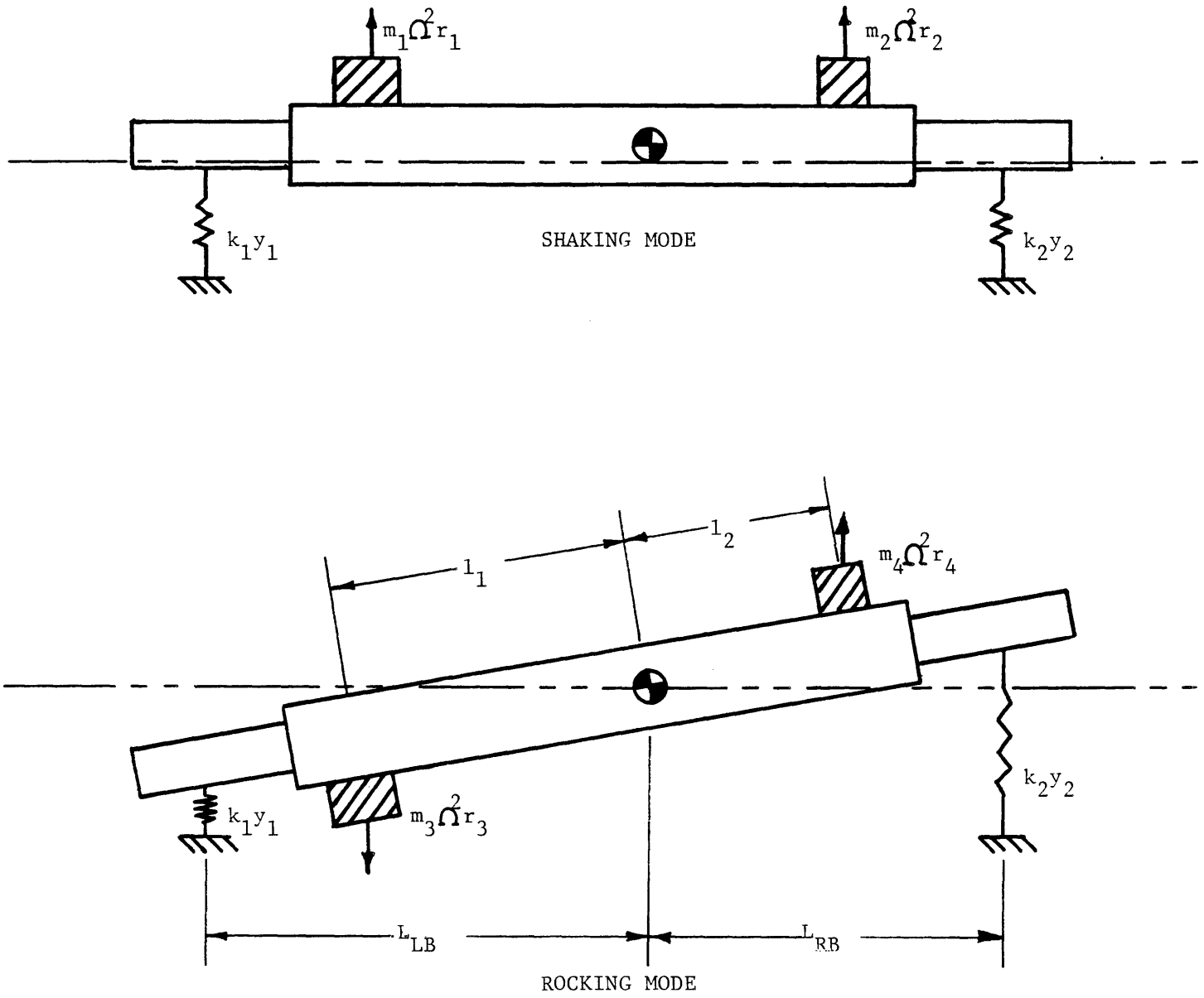

FIGURE III.4.1 EXCITATION OF FIRST TWO MODES

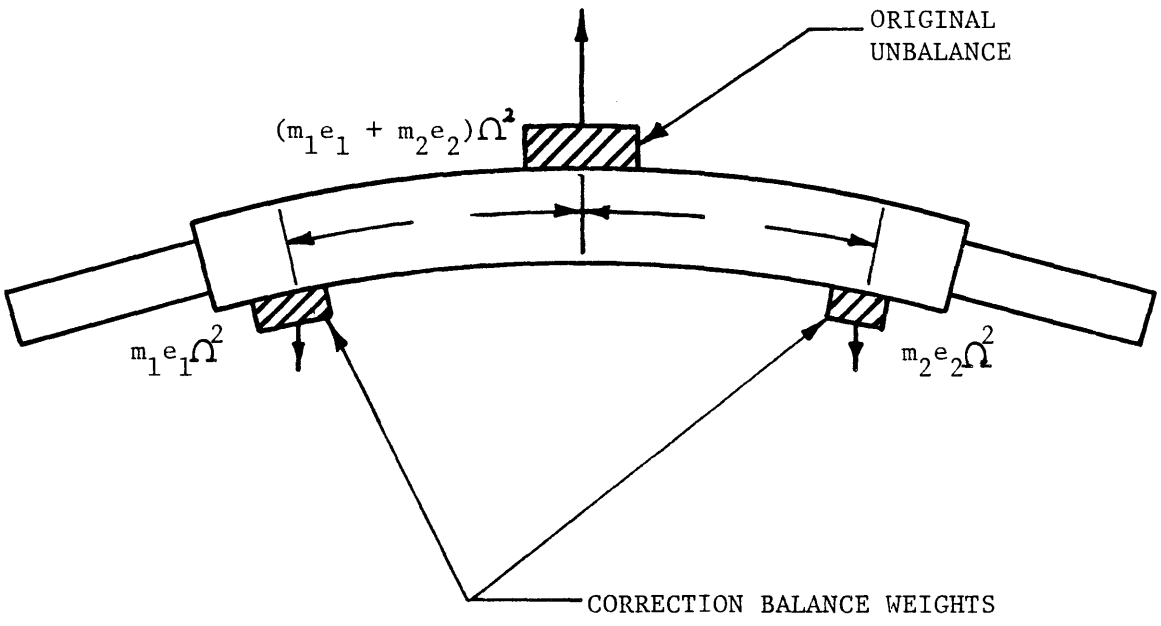

FIGURE III.4.2 EXCITATION OF THIRD MODE

active section. The stub shafts are: 1) machined and 2) virtually concentric with the bearings and therefore have little unbalance. The active center section: 1) has many asymmetries in the field and damper windings (the damper winding has a 30-mil runout in places) and 2) will have the greatest runout due to rotor bowing. It is probable that this section is highly out of balance. Therefore, balance weights were transferred inside the rotor to the planes adjacent to the active section. By placing the corrective weights closer to the actual source of unbalance we hope to minimize the third mode excitation due to unbalance and the correction weights.

III.4.2 INFLUENCE COEFFICIENT METHOD

In this section we follow the coordinate conventions established in figure I.3.2.

Runout at a measuring plane can have two representations depending upon the selection of coordinates. If the stationary coordinates X and Y are used, then runout appears to be a sinusoidal vibration, the amplitude of which is one half of the runout. If X denotes horizontal motion or vibration and Y denotes the vertical motion, then we expect to see that

$$X = A \sin(\Omega t) \qquad \text{(III.4.4a)}$$

$$Y = B \sin(\Omega t - \psi) \qquad \text{(III.4.4b)}$$

where A is one half of the runout measured in the X-direction and B is one half of the runout in the Y-direction. When the system is far from system resonances and with light damping, the phase angle, ψ , equals 90 degrees.

Another way of expressing the same runout is by using the rotating coordinates x and y. We assume that the runout is synchronous with the rotor rotation. The runout can be represented by a phasor, lagging by phi degrees from a phi equal to zero reference direction. The zero reference is arbitrarily set at the rotor A-pole center. The magnitude of the phasor is either A or B if A equals B, otherwise it is the vector sum of A and B. Phasor representation may also be used for the rotating force associated with a mass unbalance. The force phasor, $\vec{F}$, is

$$\vec{F} = m\Omega^2 \, r \, e^{i\phi} \qquad \text{(III.4.5)}$$

where r is the distance from the bearing/bearing center line to the deflected mass center line.

The phasors, which are described by a magnitude and a constant angle, ϕ , from the A-pole, are represented by complex numbers. For

example, the vibration at plane a in rotating x-y coordinates is

$$\vec{V}_a = Ae^{i\phi} = A(\hat{i}\cos\phi + \hat{j}\sin\phi) \qquad \text{(III.4.6a)}$$

and the unbalance in plane I for example is

$$\vec{U}_I = m_1 r_1 e^{i\phi} = m_1 r_1(\hat{i}\cos\phi + \hat{j}\sin\phi) \qquad \text{(III.4.6b)}$$

Let $[\alpha]$ be the influence coefficient matrix. Each of the two unbalances in planes I and II will influence the vibration and therefore the runout phasors at planes a and b. The four complex components of the matrix will be α_{mn} where m is the plane of vibration and n is the plane of unbalance. Then,

$$\begin{Bmatrix} \vec{V}_a \\ \vec{V}_b \end{Bmatrix} = \begin{bmatrix} \alpha_{aI} & \alpha_{aII} \\ \alpha_{bI} & \alpha_{bII} \end{bmatrix} \begin{Bmatrix} \vec{U}_I \\ \vec{U}_{II} \end{Bmatrix} \qquad \text{(III.4.7)}$$

By pre-multiplying each side of this equation by $[\alpha]^{-1}$ we get,

$$\begin{Bmatrix} \vec{U}_I \\ \vec{U}_{II} \end{Bmatrix} = \begin{bmatrix} \alpha \end{bmatrix}^{-1} \begin{Bmatrix} \vec{V}_a \\ \vec{V}_b \end{Bmatrix} \qquad \text{(III.4.8)}$$

So by experimentally obtaining the components of the influence coefficient matrix and taking its inverse, the unbalance for a rigid rotor can be located.

To measure vibration (section V.2) we used the X and Y strain gages instead of the proximity probes because the bearing compliance across which the probes measure can become highly non-linear. The strain gage signals were processed by an analog computer. The DC offset was removed from the signal. Gain was added to the signal so that the analog computer output was 200 millivolts per mil of bearing-to-ground motion.

Several cycles of the signal were then digitalized and temporarily stored on RAM in a Nicolet digital oscilloscope. Both the processed analog signal and a zero phase marking trace were simultaneously fed into the Nicolet. The information in the scope could be internally transferred to floppy disk for longer term storage. The Nicolet was then connected to the Joint Computer Facility at MIT by modem. The vibration data was fed into a program which converted the binary data into floating decimal point form and stored the information onto data files which were then backed up on magnetic tape. In this manner the original strain gage information could be handled by Fortran computer programs. Programs available could then be used to plot the signal, filter the signal, do a fast fourier analysis, and combine signals for lissajous construction (see essential program listings in Appendix C).

At a given rotational speed, 600 RPM in the first iteration, 1000 RPM in the second iteration, the X-direction vibration was measured at planes a and b. Then a trial weight of 1.00 pound at a radius of 6.875 inches was attached to the free end of the rotor at a fixed angular

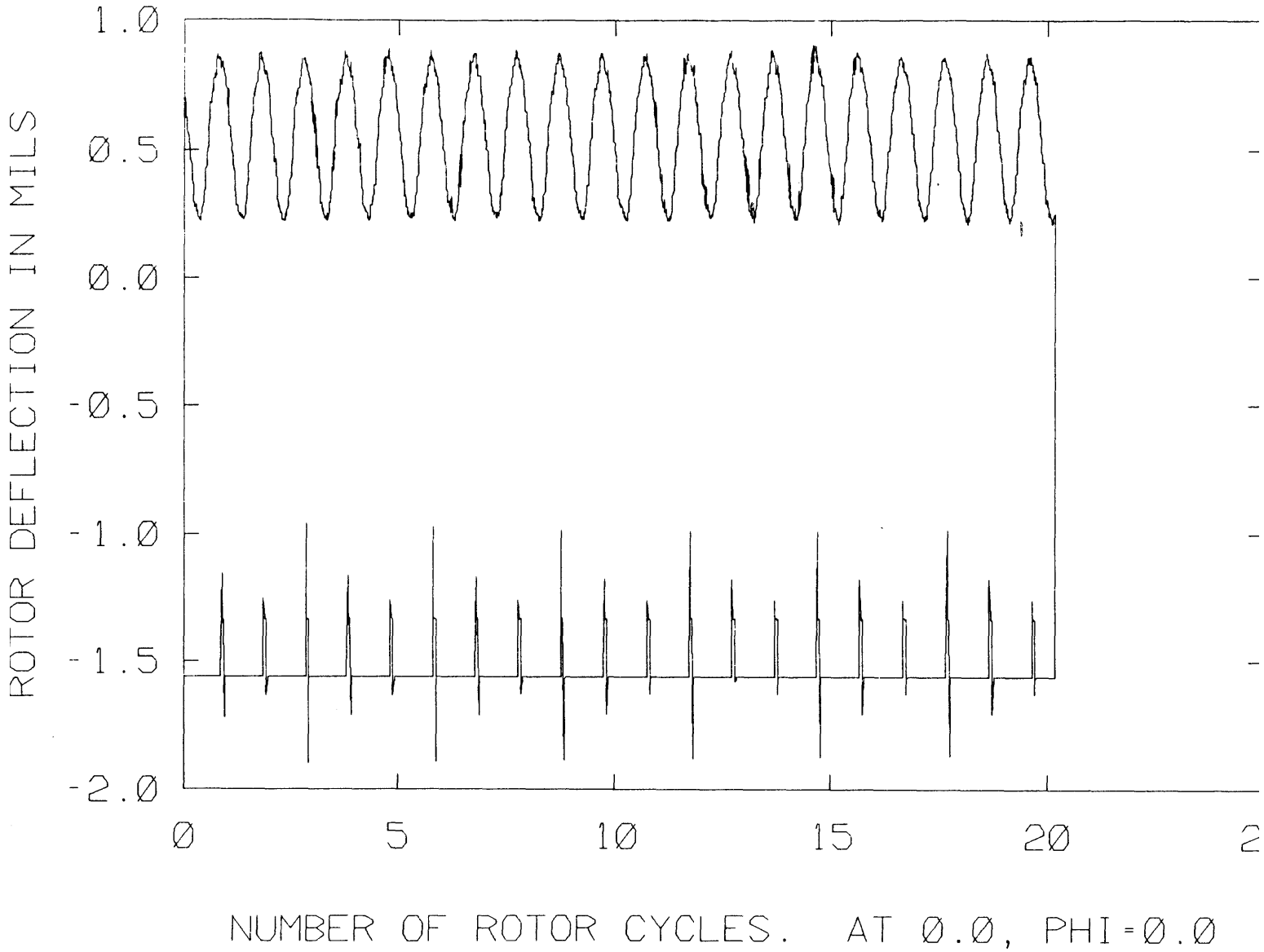

FIGURE III.4.3 VIBRATION SIGNAL OF FREE END, X-DIRECTION, BEARING/GROUND MOTION AT 600 RPM BEFORE LOW-SPEED BALANCING

location of phi equal to 285 degrees. The resulting vibrations at 600 RPM were measured at each bearing with the X-direction strain gages. A sample of the plotted vibration from the X-direction strain gage at the free end is shown in figure III.4.3 for the unbalanced condition. The phase and magnitude are read from this plot.

By vectorially subtracting the original unbalance vibration from the vibration with the weight attached, the effect of the weight alone on a balanced shaft could be deduced. This calculation led to the complex influence coefficients α_{aI} and α_{bI} . The weight was then removed and attached to the drive end at a radius of 6.875 inches and a fixed angle of phi equal to 278 degrees. The same calculations gave the influence coefficients α_{aII} and α_{bII} .

Using a Hewlett-Packard-15 hand held calculator, the coefficient matrix was entered in complex form, inverted, and multiplied by the unbalance in planes I and II. Then the balance weights to be added were of the same magnitude as the unbalanced calculated but 180 degrees around the shaft. With this process the zero-to-peak vibration magnitude was reduced from 0.43 mils at the free end and 0.37 mils at the drive end to 0.09 mils and 0.12 mils respectively. Finally, we collected response information at 1000 RPM. At this speed the zero-to-peak X-direction free and drive end vibration magnitudes were 0.20 mils and 0.22 mils respectively.

The process was iterative. In order to amplify the effect of an unbalance we needed to run at a high speed (1000 RPM). But in order to

run at high speed without excessive vibration the rotor had to be already balanced at a lower speed (600 RPM).

The major limitation of a two plane balance is that it assumes the rotor to be rigid. The rigid rotor assumption becomes less true as the balancing speed increases. At maximum rotor speed (4140 RPM), and even at normal operating speed (3600 RPM), the third mode, which we did not expect to see at low speeds, may become a factor. Therefore, another balance may have to be performed which takes into account rotor flexing in the third mode.

III.4.3 SELECTION OF MEASURING AND BALANCE PLANES

Selection of these planes requires a review of the mode shapes to be measured and excited along with the physical constraints involved. Two planes are required for measuring and two for balancing so long as the rotor remains essentially rigid.

As discussed further in sub-section III.7.2, instrumentation is required to measure bearing/shaft clearance to help prevent bearing rubs; and measurement of bearing support spring deflection is required to help prevent spring failure. This instrumentation was designed to measure shaft motions in the vertical and horizontal directions. From

figures 2.4 and 2.5 in J. Simpson's thesis [40:pp16-7] one can see that these are axial positions of relatively high deflections in the first and second modes. The second mode node is located between the bearings, roughly 41 inches inboard from the drive end bearing. In other words, the measuring planes for the low speed balance are far removed from any displacement nodes.

The balancing planes must be at accessible locations on the rotor which do not coincide with modal nodes and which allow secure attachment of masses around the circumference of the rotor. Also, since the effect of the balance weight is measured in terms of a mass multiplied by a radial distance, a small mass may be attached if the balancing plane has a large radius.

It will be important that these planes show large deflections in the third mode if they are to be used again for the third mode balance. If these planes are near nodes of the third mode shape, their influence will be small in the third mode.

Since the clearance between the rotor and stator is less than 200 mils it would be difficult to add permanent weights in the active section between the free and drive end stub shafts. A weight added 100 mils in thickness and wrapped around one half the rotor circumference would only have the balancing equivalent of 3.8 in-lbs.

In addition, traditional weight attachment by drilling and tapping holes on the rotor surface would be impossible due to the composite heat

insulating structure of the rotor in the active section. Weight attachments at or near the bearing journals are geometrically inaccessible because of the bearings, oil seals, vacuum seals, and brush rings. Exposed sections of the rotor are the large diameters of the stub shafts and the outboard ends of the stub shafts. Balancing forces could also be transferred through the gear coupling which transmits shear. The coupling, however, is not a permanent part of the rotor and the balancing forces might excite coupling or gearbox modes.

Among the possible balance planes, the large diameter flat ends of the rotor were selected. These planes have the following advantages:

* large attachment radius,
* distance from the nodes in the first two mode shapes,
* geometrical accessibility,
* solid steel sections for conventional attachments,
* can be used later as two planes of the third mode balance.

The design of the weights for this plane is discussed in sub-section III.4.4.

The low speed balance tests and an estimation of the required balance weights were completed. The weights were then position and magnitude scaled for attachment inside the rotor before the rotor was finally welded closed. This allowed us the freedom of putting the balance forces axially within the active section of the rotor. Since the greatest unbalance in the rigid rotor model is probably in the winding area, and since the winding supports are rigid relative to the thin-walled torque tubes, it would be best to transfer the balance

weights to the winding area. Weights were added to the outermost (radially) and innermost (axially) regions of the helium reservoirs (see figure I.3.1 and sub-section III.4.4). The weights are located within two inches of the support tube ends. In summary, we have identified six planes for the low-speed balance: two planes, one at each bearing (planes a and b) for measuring vibration; and two more pairs of planes, one external pair (planes I and II) and one internal pair (planes A and B) for attaching balance weights (see figure I.3.1).

III.4.4 BALANCE WEIGHT DESIGN

Balance weights had to be designed for two pairs of planes, the outer planes and the inner planes as discussed in the previous sub-section. Rotor symmetry allowed each pair of planes to have a similar design.

For the outer pair of planes, the weights could be attached by axial bolts. The bolt holes in the rotor were made by tapping threads in the existing pin holes. The pins were simply cut one inch shorter since the outer one inch of the pins carried no direct shear load (see figure III.4.4).

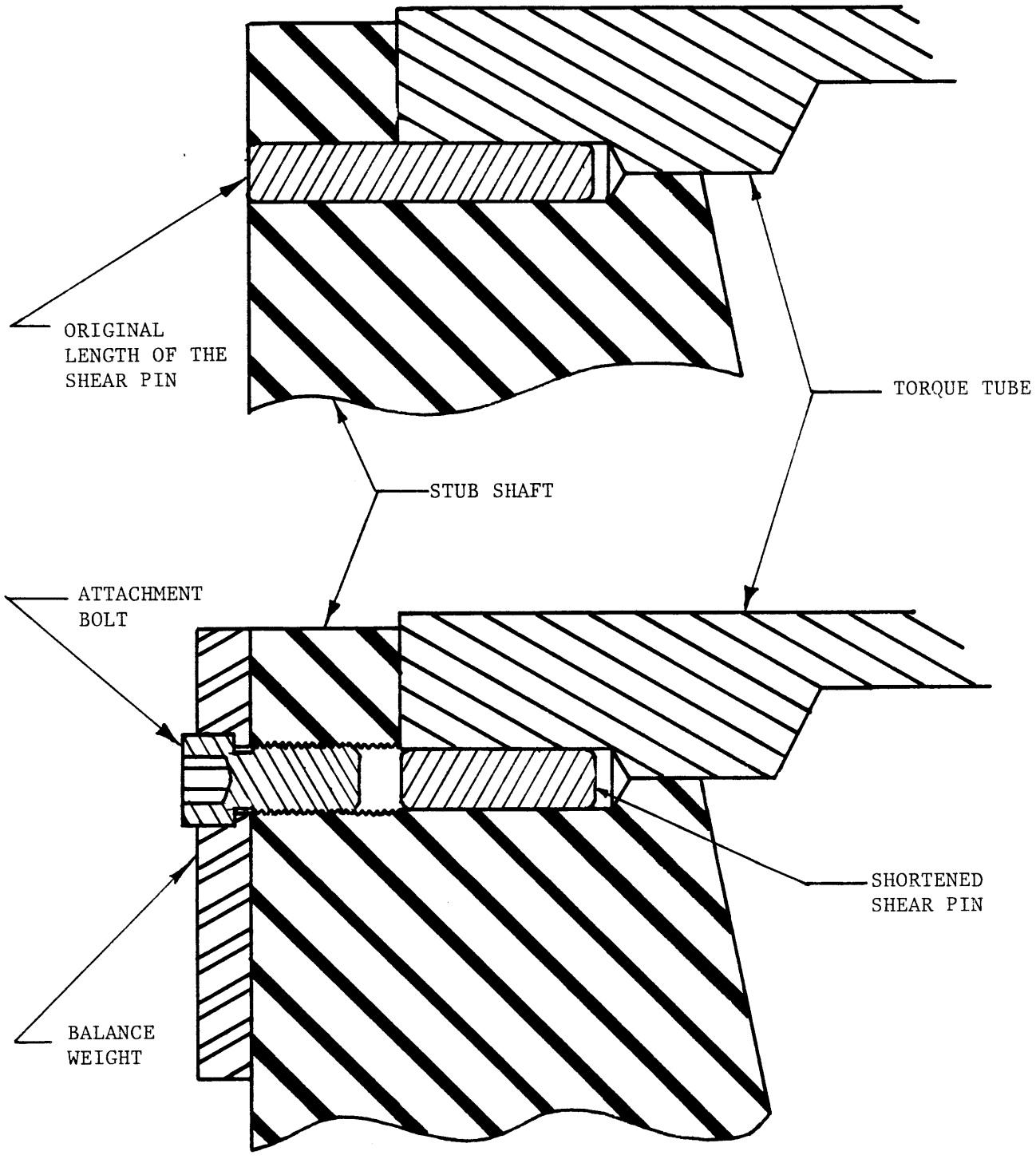

FIGURE III.4.4 WEIGHT ATTACHMENT TECHNIQUE AT PLANES I AND II

Geometrically, the weights had to clear the vacuum seals which are just over 0.9 inches distant (axially) from the face of the rotor. The outer part of the weights (radially) could not exceed the outer diameter of the rotor so that the rotor could be removed from the stator with the weights still attached. The inner part of the weight was dictated by the radius at the smaller diameter of the stub shaft. The weights, if attached permanently, also had to clear a ring of helium transfer ports on this face. The final weights appear as pie slices of an annular section.

To adjust the magnitude of the weights, the weight thicknesses vary from near zero to 0.9inches. The effect of the weight is

$$\frac{F}{\Omega^2} = \frac{\rho t \theta}{2\pi} (r_0^2 - r_i^2) e \quad , \qquad \text{(III.4.9)}$$

where,

F = centrifugal force exerted by an attached balance mass,

ρ = 0.28 lbm/in^3 = density of steel,

t = thickness of the weight,

θ = included angle of the weight,

r_i = inner radius,

r_0 = outer radius.

In (III.4.9) e is calculated by summing the effect of integrating differential masses over the volume of the weight.

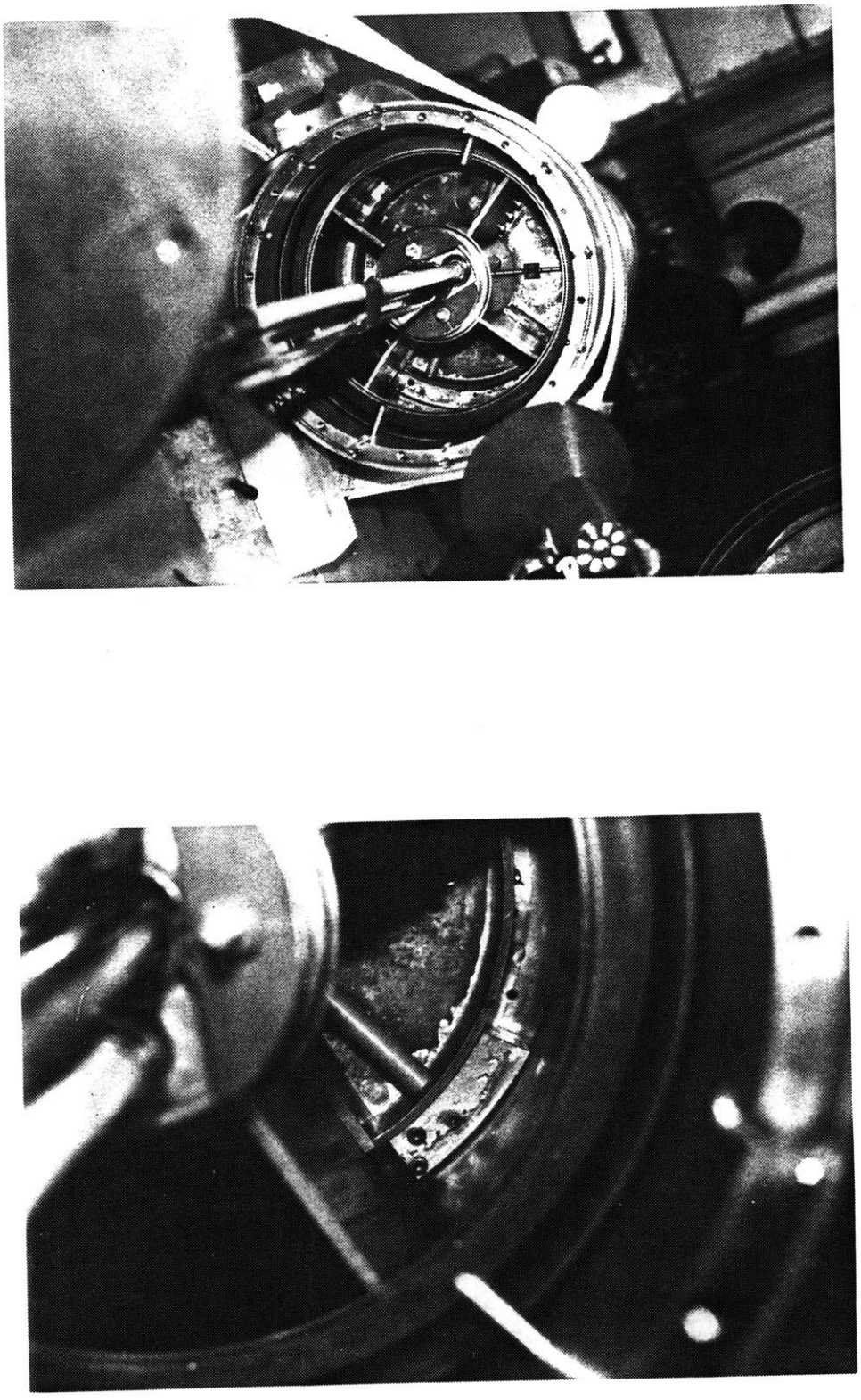

FIGURE III.4.5 FREE END INTERNAL BALANCE WEIGHT

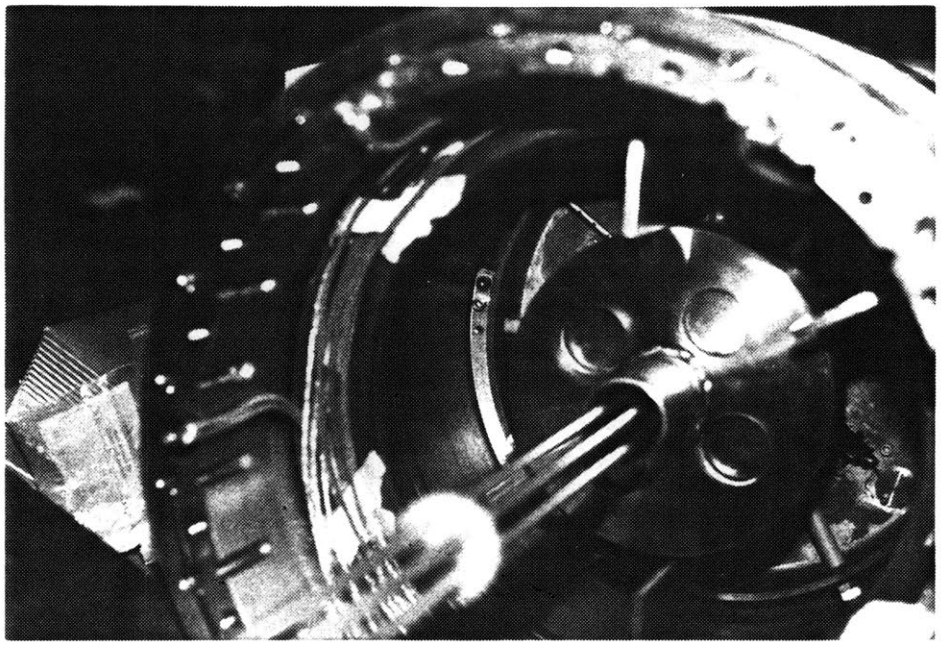

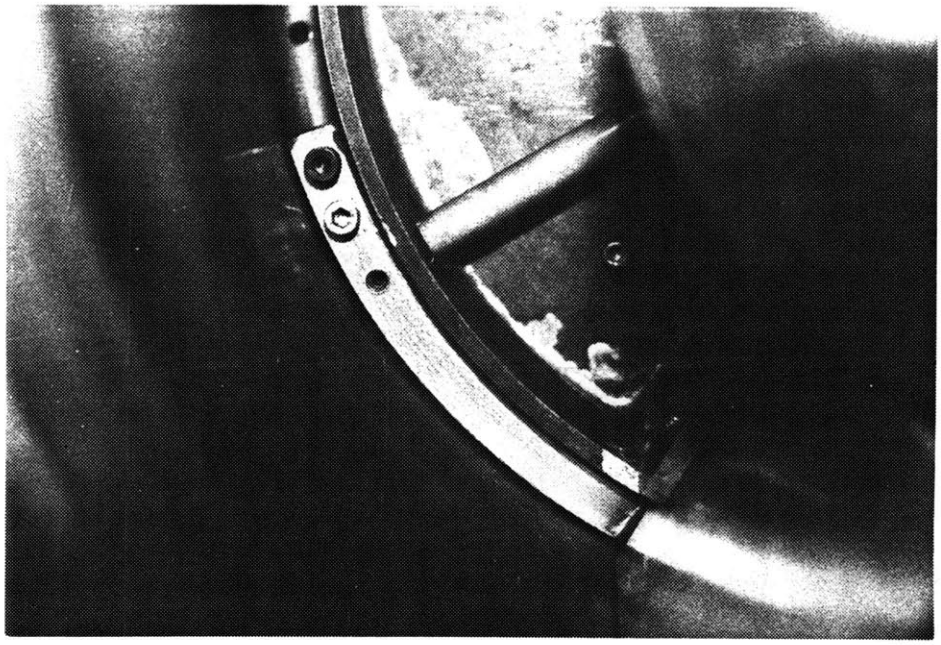

FIGURE III.4.6 DRIVE END INTERNAL BALANCE WEIGHT

$$e = \frac{2r \sin(\frac{\theta}{2})}{\theta} \quad , \qquad \text{(III.4.10)}$$

where

$$r = \frac{r_0 + r_1}{2} = \text{average radius} .$$

The angle of effect is along the radial line bisecting the angle θ .

The weights attached to the interior of the rotor (see figures III.4.5 and III.4.6) are at the outermost radial and innermost axial positions within the end reservoirs. The weights were constrained to have a flattened annular geometry between the helium reservoir and the copper, ring-shaped heat exchangers at either rotor end. The free and drive end positions are shown in figure I.3.1.

At each inner plane the radial helium flow tubes passed conveniently through the weight allowing the weight to be attached to the tube by a set screw.

III.4.5 RESULTS

The final correction weights added for the low-speed balance in planes I and II were 11.6 in-lbs at phi equal to -41 degrees and 10.8

in-lbs at phi equal to -42 degrees respectively. These weights were then replaced by weights inside the rotor at planes A and B (figure I.3.1) by preserving the effects to the first two modes. The correction weights installed at A and B were 11.8 in-lbs at phi equal to -41 degrees and 10.5 in-lbs at phi equal to -42 degrees respectively. These correction weights suggest a nearly pure shaking component probably caused by a simple lack of concentricity of the rotor as the source of unbalance.

At 600 RPM the free and drive end X-direction spring vibrations were reduced from 0.43 and 0.44 to 0.09 and 0.10 mils zero-to-peak respectively and approached the noise and double frequency levels. Without filtering the double frequency waveform and attenuating noise, further balancing would become impossible. By increasing speed, the amplitude of the fundamental frequency for a fixed unbalance increases as Ω^2. It is therefore clear why further balancing may have to be performed at higher speeds to obtain a more accurate balance.

In addition to the fundamental frequency vibration there was a double frequency vibration. The double frequency phenomenon is important if its magnitude becomes large because it is an asynchronous vibration. This sinusoidal waveform, possibly caused by asymmetrical rotating stiffness, was about 0.03 mils zero-to-peak at 600 RPM. The harmonic waveform makes fundamental waveform phase angle measurements difficult. If the double frequency is in fact caused by asymmetrical rotating stiffness then, as shown in section II.3, the magnitude of this vibration should not increase with rotational speed except at one-half

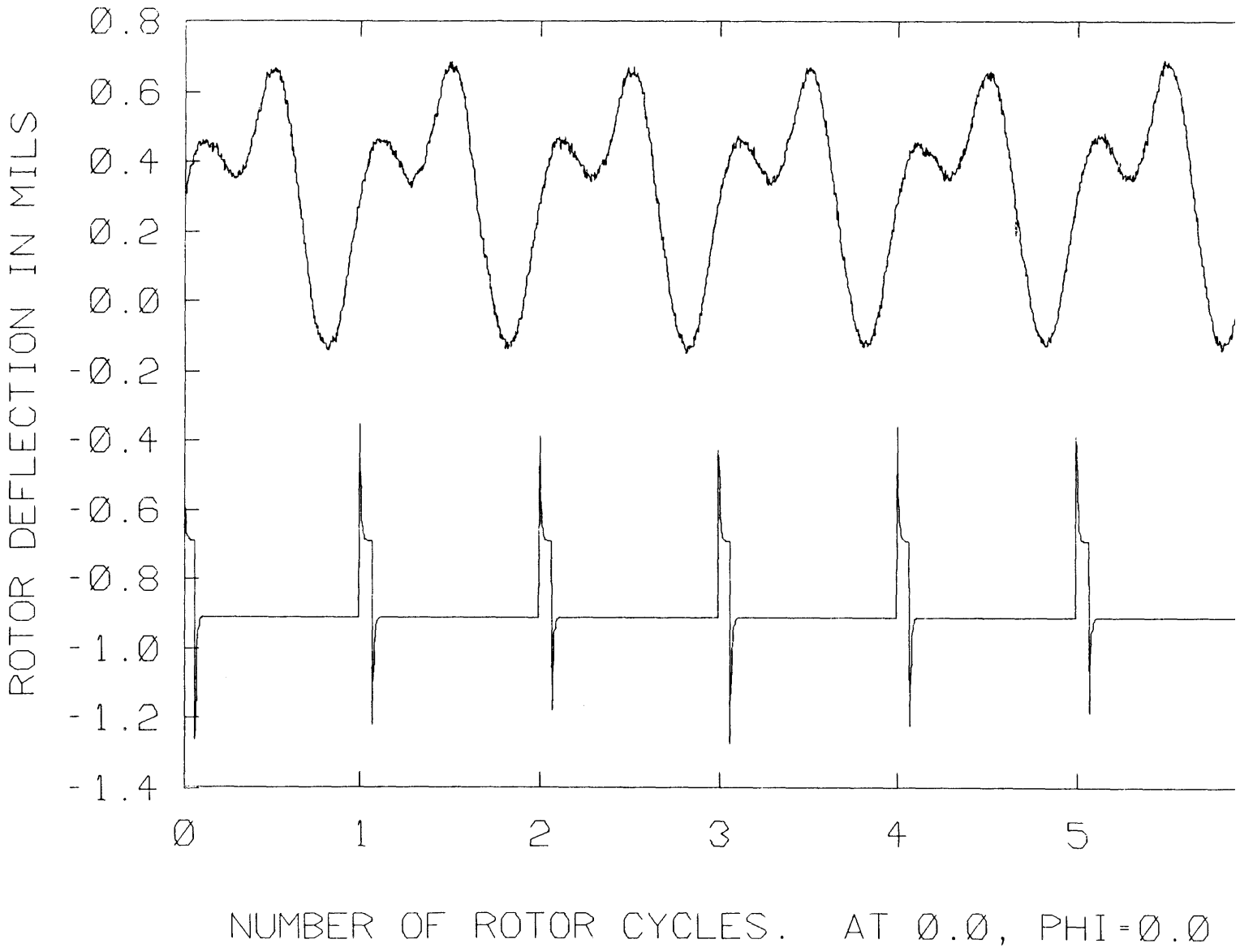

FIGURE III.4.7 RESONANT DOUBLE FREQUENCY

the first critical speed of the rotor. In fact, this secondary critical speed should occur at 1000 RPM, at which speed we measured a 0.05-mil zero-to-peak double frequency component. The free end X-direction bearing/ground vibration is shown in figure III.4.7. As predicted, the plot in figure III.4.7 shows a double frequency waveform superimposed on the primary frequency waveform, the magnitude of which is much larger than it was at other speeds.

III.4.6 MODAL EXCITATION

In order to run the rotor at its supercritical operating speed it must pass through two lightly damped resonances. The rotor system model (including springs and bearings) is a second order system with mass, stiffness and finite damping with respect to each given mode. Therefore, for a fixed excitation of a given mode we would expect the rotor lateral vibration magnitude and phase shift to follow the standard pattern of second order Bode plots.

Modal excitation and the construction of Bode plots are important for two reasons. First, the after-resonance Bode plots for the first two modes will quantify the effect from the first two modes at operating speed (3600 RPM) so that we can use the influence coefficient method to add balance weights in three planes at that speed without disturbing the first two balanced modes.

Second, we want to predict the vibration amplitudes for resonance in the first two modes. Documented experiences have shown that passing through a resonance can be catastrophic. A rotor must have low unbalance and sufficient damping to pass through a resonance without excessive vibration. In industry, many rotors of a given general design are manufactured; and the manufacturer knows from experience what level of unbalance is acceptable before passing through resonance. Our rotor is dynamically much different than conventional rotors and has no previous balancing experience to draw on.

A need exists to predict the vibration as a function of speed in a given mode. By building a Bode plot and using data collected below the resonance, we could measure damping and therefore predict the level of vibration at and beyond resonance speed. In the low-speed balance, rotor speed was restricted to 1000 RPM because the outer support hoop had not been added. Ideally we would want to run the rotor closer to resonance to build an accurate Bode plot. As an example, we constructed the magnitude portion of the Bode plot to estimate the damping in the first mode.

To construct the Bode plot we did the following. Using data from the trial weight responses at 1000 RPM, we predicted new weights which would be able to excite the shaking and rocking modes separately. The shaking mode weights were attached and vibration and phase information collected. Since the excitation magnitude increases as Ω^2 , we subtracted 40 decibels per decade from our log-magnitude plot (see

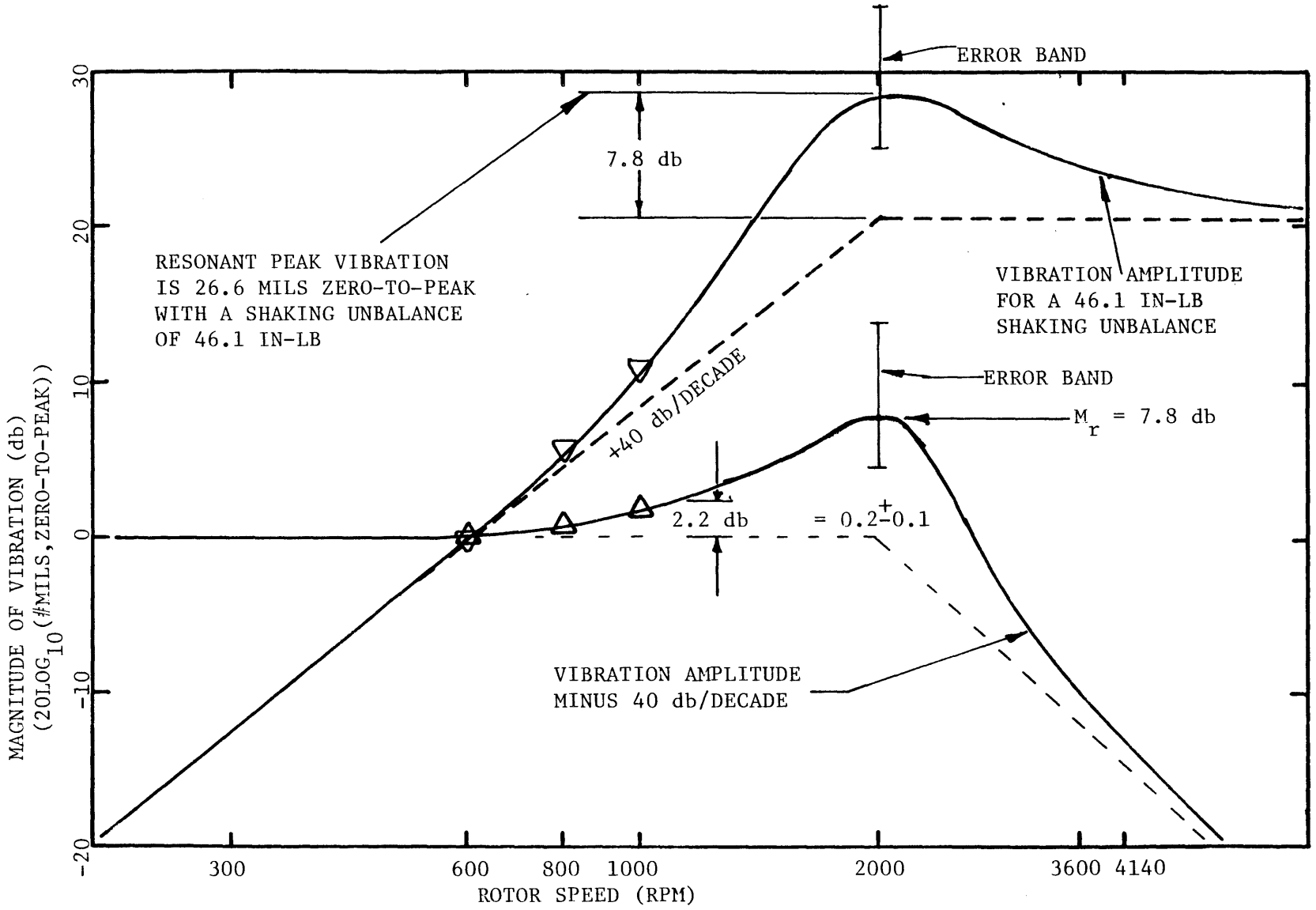

FIGURE III.4.8 ESTIMATION OF RESONANT VIBRATION

figure III.4.8). Comparison with second order textbook Bode plots showed that the damping ratio, ξ , was 0.2, with an error of plus-or-minus 0.10 for the shaking mode. Then by using equations II.2.1 and II.2.2 we extrapolated the log-magnitude curve through resonance. For the imposed 46.1-in-lb shaking unbalance we would have a 26.6 mil zero-to-peak vibration at the springs. Our residual unbalance had a shaking component of 4.7 in-lbs which translates to a 2.7-mil zero-to-peak vibration at resonance. However, if ξ equals 0.1 (due to error) then the vibration would be greater in general and a prohibitive 5.6 mils zero-to-peak at resonance. Uncertainty in the damping ratio must be reduced by collecting more log-magnitude data at higher speeds than 1000 RPM.

III.5 HIGH-SPEED BALANCE

III.5.1 INTRODUCTION

The high-speed balance has three goals: 1)to keep the vibration level caused by the synchronous unbalance forces below preset vibration limits, 2) to keep asynchronous vibration levels below a second set of vibration limits, and 3) to detect and eliminate instabilities. The

first goal is straight forward and may be accomplished by extending the influence coefficient method to more balance planes using our knowledge of the mode shapes. The other two goals are related because instabilities generally appear as asynchronous rotor vibration. Instabilities are not formally an unbalance problem but their appearance may damage the rotor system. It is important that, while attempting to eliminate synchronous rotor vibration, the rotor does not experience asynchronous rotor vibration discussed in section II.3.

At a given speed, vibration due to mass unbalance in a flexible rotor causes the rotor to assume a bent shape stationary in the rotating reference frame. The stress level due to bending at a given point in the rotor remains constant at a fixed speed. However, in asynchronous vibration the rotor shape changes with time in the rotating reference frame. The stress level at any point is always changing even at a fixed rotor speed. This cyclic stress change may cause fatigue even at vibration levels well below the safe limits for synchronous vibration. Generally the stress reversal frequency is on the order of the rotor speed. The rotor may experience a million cycles in five hours leading to possible rotor fatigue failure. Detection of these asynchronous vibrations is discussed in sub-section III.5.6.

For the static and low-speed (dynamic) balances we did not attempt to predict instabilities since, as discussed in sub-section III.5.6, instabilities which were likely to occur in this rotor have stability threshold speeds above the first critical speed of the rotor system. For balancing purposes it was acceptable to assume as a first order

approximation that the rotor vibration was a purely harmonic synchronous vibration. Above the first critical speed, however, methods must be applied to detect vibrations not originating from unbalance. A given instability will be eliminated before any further attempts at balancing.

The rotor assembly will be completed at the time of the high-speed balance. However, since the low-speed balance, the large stainless steel helium seal tube and the heavy, grouted, stainless steel fiber-epoxy support tube have been assembled to the rotor. In addition the rotor may have a slightly different shape upon reassembly if, for example, the bolts attaching the stub shafts are torqued to different levels than before the low-speed balance. The induced unbalance could be as high as 10 in-lbs (see Appendix D.3 for the related calculation).

For the above two reasons it may be necessary to repeat the low-speed balance before proceeding to pass through the first critical speed.

III.5.2 BALANCING METHODS AVAILABLE

Historically there are two balance methods used on assembled super-critical rotor systems:

1) the influence coefficient method [3, 4, 28, 43, 44, 45], and

2) the modal balance method [14, 22, 35, 36].

Many variations on these methods exist as well as optimized techniques which are discussed in the literature [1, 5, 23, 36, 46]. A third method, component balancing, exists only for preassembled built-up rotors with short axial sections.

Once the unbalanced rotor is assembled it must be balanced by either the modal or the influence coefficient method. The modal method requires a prior knowledge of the mode shapes which were found analytically using the finite element program ADINA. Since in this method the modes are balanced directly, the resonant vibrations should be low. The unbalance vibrations away from resonances are the result of remaining unbalanced modes. If enough modes above operation speed are balanced, the rotor should run smoothly at 3600 RPM.

The influence coefficient method makes no initial assumptions about the rotor except that an understanding of the general mode shapes can aid in planning measuring and balancing planes which do not coincide with nodes of vibration. One attempts to reduce rotor vibration at specific speeds and specific planes along the rotor. The matrix equations are [35],

$$\begin{bmatrix} \alpha_{11}^{(1)} & \alpha_{12}^{(1)} & \cdots & \alpha_{1q}^{(1)} \\ \alpha_{21}^{(1)} & \alpha_{22}^{(1)} & \cdots & \alpha_{2q}^{(1)} \\ \vdots & \vdots & & \vdots \\ \alpha_{n1}^{(1)} & \alpha_{n2}^{(1)} & \cdots & \alpha_{nq}^{(1)} \\ \alpha_{11}^{(2)} & \alpha_{12}^{(2)} & \cdots & \alpha_{1q}^{(2)} \\ \vdots & \vdots & & \vdots \\ \alpha_{n1}^{(2)} & \alpha_{n2}^{(2)} & \cdots & \alpha_{nq}^{(2)} \\ \vdots & \vdots & & \vdots \\ \alpha_{n1}^{(m)} & \alpha_{n1}^{(m)} & \cdots & \alpha_{nq}^{(m)} \end{bmatrix} \begin{Bmatrix} U_1 \\ U_2 \\ \vdots \\ U_n \\ U_{n+1} \\ \vdots \\ U_{2n} \\ \vdots \\ U_{qn} \end{Bmatrix} = \begin{Bmatrix} V(x_1, \Omega_1) \\ V(x_2, \Omega_1) \\ \vdots \\ V(x_n, \Omega_1) \\ V(x_1, \Omega_2) \\ \vdots \\ V(x_n, \Omega_2) \\ \vdots \\ V(x_n, \Omega_m) \end{Bmatrix} \quad \text{(III.5.1)}$$

and

$$\{U\} = [\alpha]^{-1} \{V\} \quad \text{(III.5.2)}$$

The influence coefficient matrix of equation III.5.2, $[\alpha]^{-1}$ is found by inverting the $[\alpha]$ matrix of equation III.5.1. In order to invert the $[\alpha]$ matrix by standard methods it must be a square matrix. Therefore, if the rotor is run at M speeds in N measuring planes, the number of balance corrections, q, must be such that

$$q = (m)(n) \quad \text{(III.5.3)}$$

This represents the number of balance planes in which to add trial and final balance weights.

The literature discusses the merits of each method extensively. In the practical case where the balance speeds of the influence coefficient method are chosen at the rotor critical speeds it is shown [35] that the two methods have the same effect. We will apply the influence coefficient method near the critical speed as in the low-speed balance. Then the influence coefficient method can be extended to a third plane at 3600 RPM. By using the Bode plots to scale the influence coefficients of the first two modes to 3600 RPM, we can calculate the addition of weights at this speed which will be orthogonal to the first two modes. In this way we avoid disturbing the low-speed balance. In balancing the rotor therefore a hybrid of the two methods may be used.

III.5.3 PROCEDURE

At the writing of this thesis the high-speed balance has not been made. Due to the iterative nature of balancing the procedure is mapped in block diagram form in figure III.5.1.

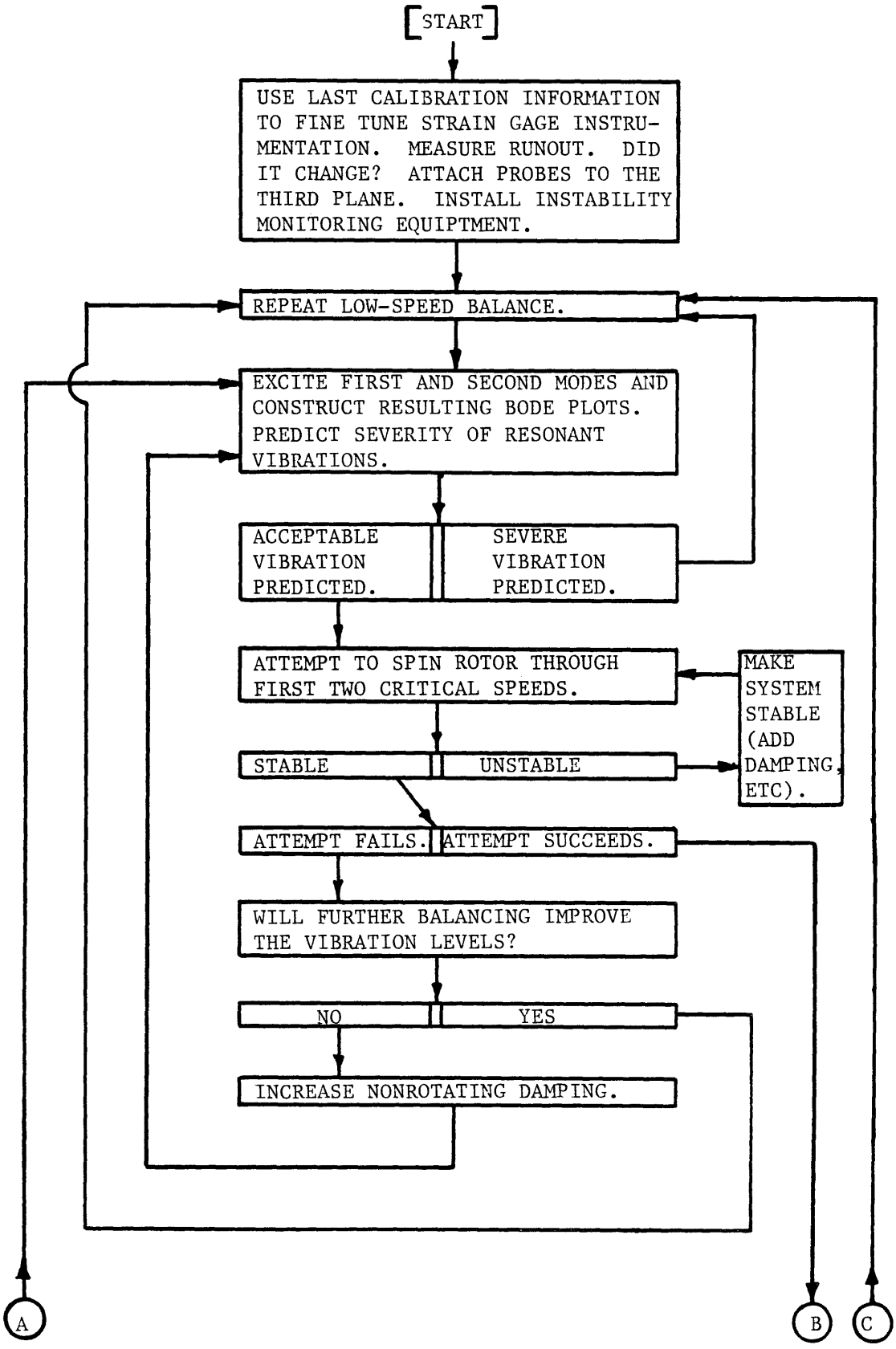

FIGURE III.5.1 BLOCK DIAGRAM OF THE HIGH-SPEED BALANCE (PART A)

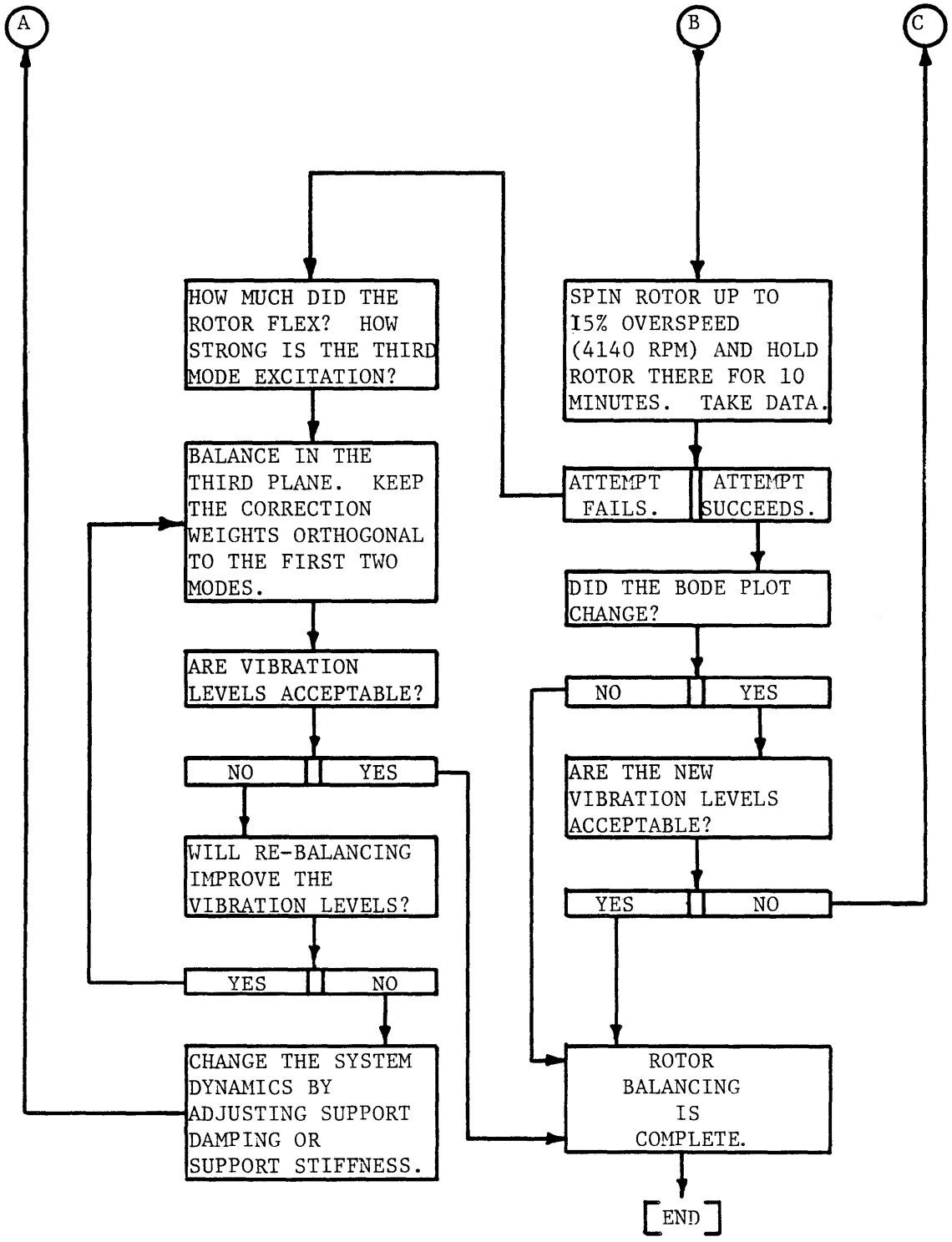

FIGURE III.5.2 BLOCK DIAGRAM OF THE HIGH-SPEED BALANCE (PART B)

III.5.4 SELECTION OF A THIRD BALANCING PLANE

Third balancing and measuring planes were chosen on the drive end in the drive coupling area. This plane is an axial location of high amplitude deflection in the third mode and is separated far enough from the other balancing and measuring planes to give independent data for measuring and a large bending moment for balancing.

The rotor runout will be measured from ground using a Bently-Nevada Co. proximitor. An inherent problem with the proximitor is that it reads low-speed rotor runout as a rotor center line runout, which is false if the outside surface is not concentric with the rotor center line. Two methods may be used to eliminate static surface runout. The first method is to subtract the low-speed runout from high-speed runout data as explained in Chapter V. The second method is to turn the rotor in its bearings at very slow speed (on the order of 20 RPM) and grind the coupling surface concentric with a tool-post grinder.

The balancing weights are temporarily attached to a 12-inch-diameter plate. The plate is an annulus which is fitted over the 6-inch-diameter coupling portion of the rotor. The plate can be attached to the balance coupling (or for later balancing to the rotor shaft next to the gear coupling) with screws. The plate has holes bored at equally spaced locations around its periphery. Half-inch bolts with nuts and a

variable number of washers are attached to these holes and act as trial and balance weights.

Once the balance is complete the weight may be transferred to the shaft or to the gear coupling by metal removal. If balance weights are transferred to the coupling, they will be attached to the coupling half which is rigidly attached to the shaft.

III.6 DETECTION OF ASYMMETRICAL VIBRATIONS

III.6.1 INTRODUCTION

The need for identifying asynchronous vibration has been outlined earlier in this chapter. Briefly, asynchronous vibrations introduce stress cycles in the rotor which can cause rotor fatigue.

Forced vibration occurs at the frequency of the cyclic input force. In the case of rotor vibration this force is caused by unbalance which is a synchronous excitation. Self-excited vibrations occur at the free vibration frequencies of the rotor (the critical speeds). If any mechanism exists to couple the rotating rotor motion to an unstable

whirl, then the rotor will either destroy itself or reach a limit cycle before the bearing rubs. Even if the limit cycle prevents rubs between the rotating and stationary parts, the rotor will be whirling at the first critical speed while the rotor is turning at some other speed, and the result is asynchronous whirl.

Three ideas are outlined in the following sub-sections for detecting asynchronous rotor vibrations. Two similar ideas involve using filters. Professor S. Crandall at MIT suggested the direct application of tracking filters. This method has been used in industrial applications where the critical speed was known. Digital tracking filters are available for this application. The second filtering method employs a spectrum analyzer.

The third idea is unique and is used specifically to detect a backwards synchronous whirl. A backwards synchronous whirl is an asynchronous whirl with respect to forward rotation. Backwards synchronous whirl causes reversing rotor stresses at twice the rotor frequency.

III.6.2 SPECTRUM ANALYSIS

A spectrum analyzer which continuously and quickly analyzes the frequency spectrum over the 10 to 100 hertz range is a useful tool for locating the position of the first critical speed and detecting asynchronous vibration [11]. This method has an advantage over fixed narrow band filters. If the critical speed is a function of rotor speed then narrow band filters will not detect the instability. This statement is especially true with the addition of the flywheel which makes the system critical speeds more speed dependent.

See figure III.6.1. (A) shows the spectrum analyzer response at low rotor speed. As the speed increases, (B) and (C), the synchronous vibration reaches a resonance which indicates the critical speed. As the speed is increased still further the synchronous vibration amplitude remains roughly constant (at least for that mode) as seen in (D), (E), and (F). However, a stability threshold is reached in (E) which occurs at or near the critical speed measured earlier. At this point the rotor drive would be manually cut off. This method of detecting asymmetrical vibrations requires constant human monitoring and would be inadequate for long term use.

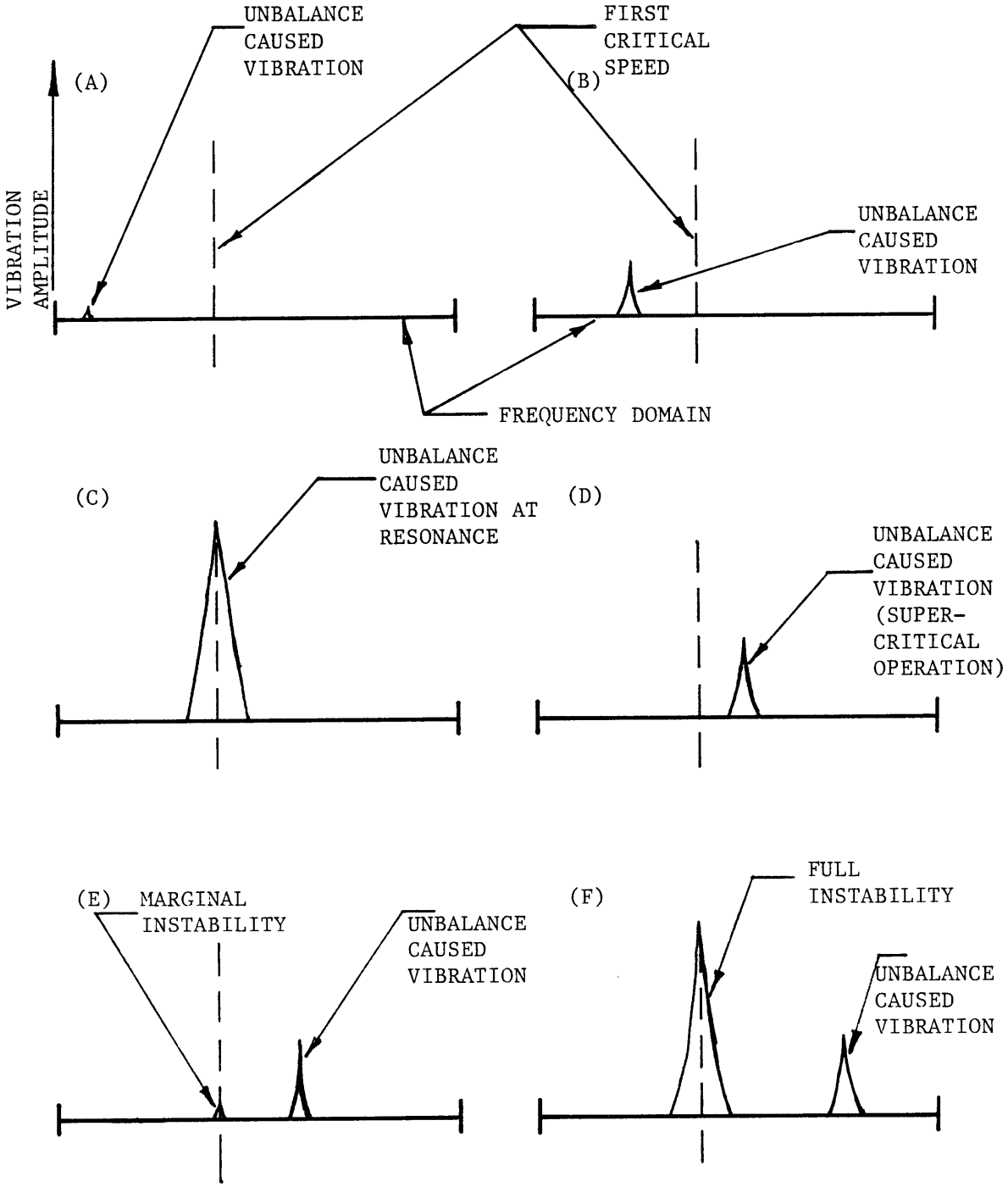

FIGURE III.6.1 SPECTRUM ANALYSIS

III.6.3 FILTERS

Filters will be installed for monitoring the first two critical speed frequencies of the rotor. By building our own filters we can design the bandpass characteristics of the filter to exclude the operating frequency and neighboring critical speeds. Then vibration limiters of the design of sub-section V.4.8 can monitor these specific frequencies at several points along the rotor.

Since we will tolerate no vibration at these frequencies when the rotor turns at 3600 RPM, the vibration limits will be set just above the maximum noise level. The noise levels after these filters should be quite low compared to the unfiltered vibration signals due to the relatively low band width and the exclusion of 60-hertz noise. It is therefore expected that the sensitivity of these circuits will be a function of transducer sensitivity and limit circuit drift. Transducer sensitivity for both strain gages and proximitors is on the order of microinches. Due to the complexity of the limit circuits, it is suggested that the temperature induced drift for this circuit be measured experimentally if the limits are set very low relative to the noise level.

If a tracking filter can be used to follow the synchronous vibration and another fixed filter used to measure the critical speed

vibration, then lissajous traces from filtered X- and Y-direction vibration signals might appear as seen in figure III.6.2. If the rotor is on a stability threshold (marginally stable), then the lissajous would spiral in and out to its limit cycle given the slightest disturbance, as seen in (B) of the figure. When the rotor is stable, (B) should remain a point. (A) is a trace of the runout phasor of the rotor due to unbalance and will be a circle if the horizontal and vertical stiffnesses to ground were equal and linear.

III.6.4 Z-AXIS LISSAJOUS PATTERNS

By using the oscilloscope z-axis circuitry discussed in subsection V.4.6, a lissajous pattern can be traced which distinguishes between backward and forward whirl. Basically, the circuitry we designed attaches a virtual arrow to the X-Y lissajous pattern indicating the direction of the X-Y orbital motion of the rotor whirl. By viewing the trace on an oscilloscope we can observe the lissajous pattern, direction, and phase.

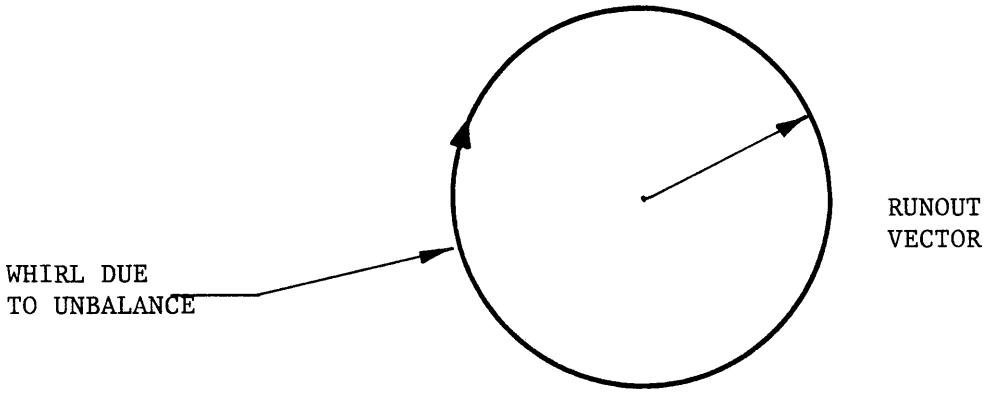

A) SYNCHRONOUS FILTERING

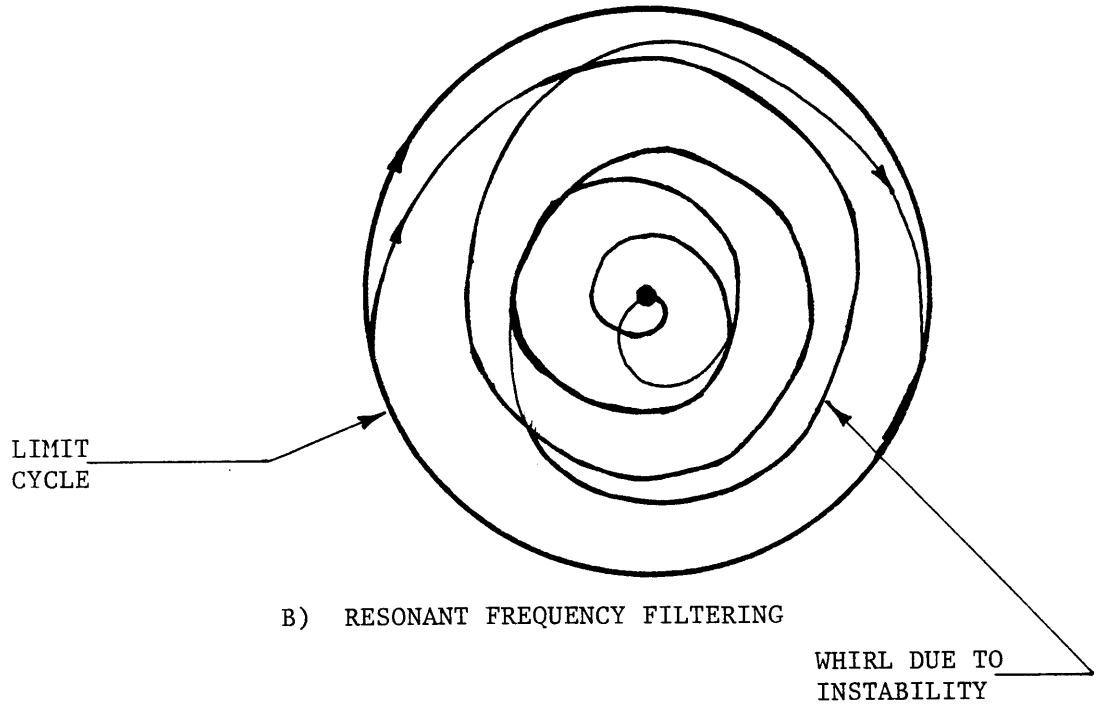

B) RESONANT FREQUENCY FILTERING

FIGURE III.6.2 LISSAJOUS PATTERNS USING FILTERS

III.7 POST BALANCING OPERATION

III.7.1 SIGNATURE ANALYSIS

Professor R. Lyon at MIT suggested that two forms of signature analysis may be used to monitor the rotor. The first is a vibration log-magnitude versus rotor speed curve to be traced at rotor start-up and shut-down. A change in this trace from one run to another may indicate a change in the system, which is a warning sign that the rotor-bearing system has been altered. A difference in the curve between deceleration and acceleration indicates nonlinearities such as the spring hardening phenomenon or a change in mass unbalance.

The second form of signature analysis is the familiar frequency spectrum. This form of signature analysis has the advantage that it can be done continuously while the rotor is operating at 3600 RPM. In this way a change in rotor dynamics can be detected between shut-downs.

While any change in the signature analysis may indicate problems with the rotor, signature analysis is generally not specific enough to identify the particular problem.

III.7.2 VIBRATION LIMITS

The vibration limits discussed in sub-section V.4.8 will continuously monitor vibrations and shut the rotor down if dangerous vibrations appear. Two modifications will be made to the present system used for balancing. First, the limit circuits presently drive a relay which shuts down the spin motor. Some minor rewiring in the control booth will enable the relay to instead shut down the prime mover. Second, filters must be built which monitor the critical frequencies along with additional limit circuits.

III.7.3 ADDITION OF LIQUID HELIUM

Cooling to liquid helium temperature will contract the rotor 0.25 inches axially. The thrust bearing is located at the free end bearing. Therefore, upon cooling, the rotor will move inboard through the drive end bearing by 0.25 inches. The most significant change will occur when the flywheel is attached. The flywheel overhang will be decreased by 1.7 percent. Since this is a small change, it is suggested that the rotor (with the flywheel) be balanced warm, then tested cold. If

vibration levels with the cold rotor are unacceptable, an ADINA analysis may be used to determine the change in system dynamics due to rotor shrinkage.

The rotor should not bow (sub-section III.2.1) due to small temperature asymmetries at liquid helium temperature.

III.7.4 ADDITION OF THE FLYWHEEL

An 1850-pound pre-balanced flywheel will be overhung on the rotor outboard of the drive end bearing for some of the later generator tests. The purpose of the flywheel is to: 1) protect the coupling, gearbox, and power turbine stage from large, short-duration fault torque; and 2) match the present gas-turbine-generator inertia to that of a steam-turbine-generator system. When the flywheel is installed the spring mounts must be replaced. New strain gages must then be mounted and calibrated.

Two potential problems arise when the flywheel is added. First, the rotor critical speeds become speed dependent because the flywheel angular momentum increases with speed. In modes where the angular momentum changes, the rotor stiffness and therefore the critical speeds increase with rotor speed.

Second, under certain conditions, rotor-flywheel systems are predicted to experience reverse whirl. Professor L. Bucciarelli of MIT proved this to be a stable dynamic state for a flywheel [8]. However, it has been difficult to sustain a reverse whirl in the laboratory, and the amplitude is generally very small compared to forward whirl when it does occur. This phenomenon may be detected with the z-axis lissajous method.

The bearing support springs will be exchanged when the flywheel is added. The new support springs are designed to keep the critical speeds and mode shapes similar to the rotor without the flywheel. However, the flywheel does change the system somewhat. For example, the second critical speed increases because the flywheel makes angular (rocking mode) motions stiffer [38]. If the system dynamics are changed significantly then the procedures outlined for the low- and high-speed balances should be repeated.

IV HARDWARE DESIGN

IV.1 DRIVE MOTOR

This chapter is limited to hardware designed to turn the rotor while balancing. The chapter is divided into two sections, one on the drive motor and one on the drive coupling.

When the hardware design began, a hydraulic drive motor had already been selected and purchased for the low-load generator spin tests that are planned. Since the balancing runs have nearly the same drive requirements, the motor installment was designed so that both the balancing and the spin tests could be done with little change of hardware.

A rigid stand was built with 4-inch-square, 1/4-inch-wall, box beams to support the motor foot (motor mount) at the right height. The

geometry of the stand had to allow clearance for the flywheel and the instrument coupling in later tests. The geometry also had to include a means for supporting the instrument coupling transformer primary coils and a flywheel shield. The motor is supported directly by a foot in the form of an angle plate which we designed to accommodate the instrument coupling. Flat ground plates are provided at the stand-to-foot interface to facilitate later alignment and pinning. Drawings and photos of the foot and stand are in Appendix A.

The motor itself is a Dynapower Co. 3-cubic-inch displacement hydraulic motor. The hydraulic fluid is supplied by tapping the supply lines from the hydraulic pump for the turbine starter motor. (See the piping schematics in Appendix A. We plan to only use a fraction of the flow from this system.) At low power a series throttling valve and a bypass valve are used to avoid unnecessary losses.

IV.2 DRIVE COUPLING

A schematic of the drive coupling is shown in figure IV.2.1. The drive coupling was designed to handle 40 HP at 3600 RPM. It has a torsional stiffness of 3204 in-lbs/radian while being relatively flexible in the lateral directions. The coupling (see Appendix A) has the following calculated shear and moment for a unit parallel

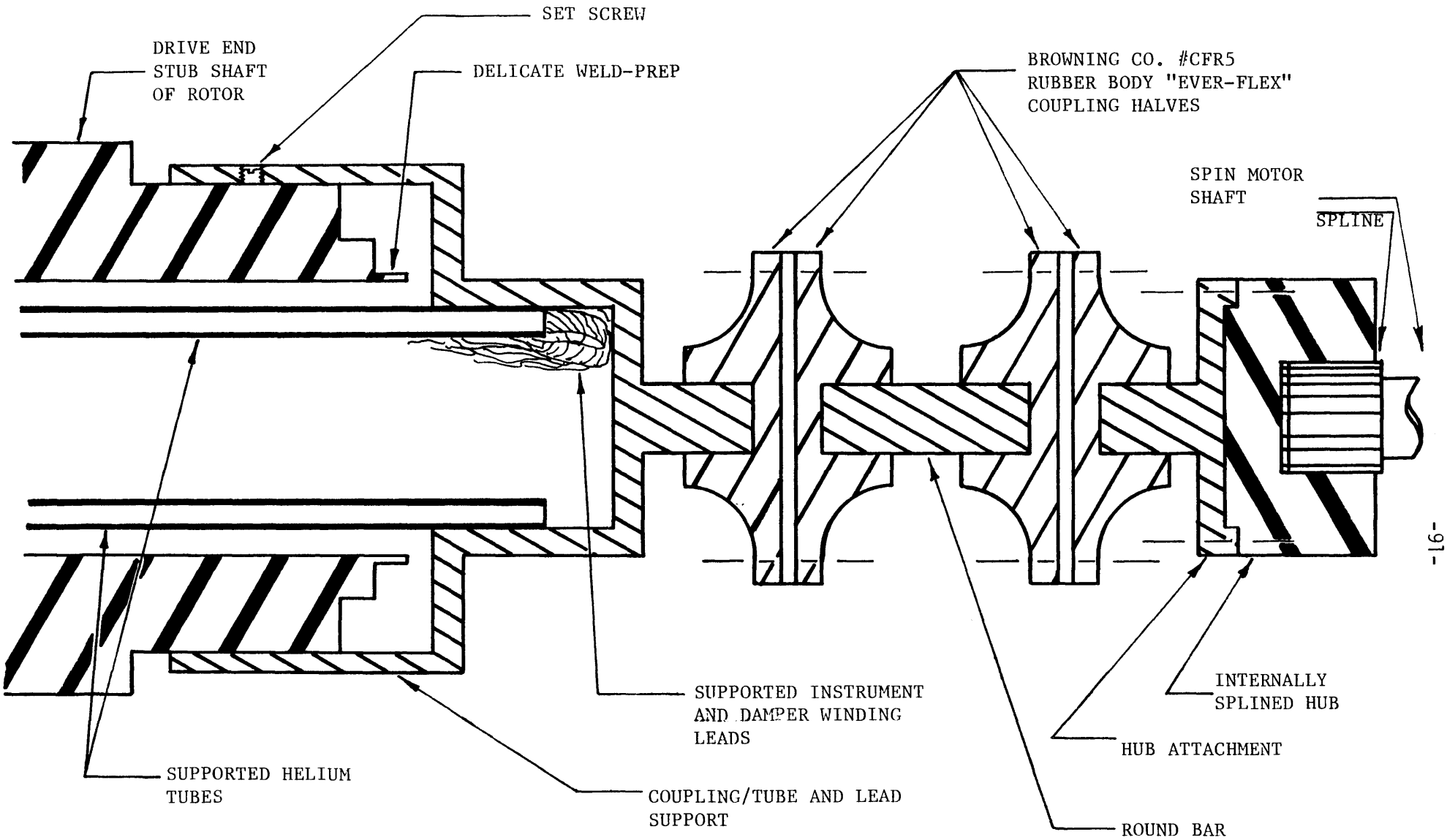

FIGURE IV.2.1 SPIN-MOTOR-TO-SHAFT DRIVE COUPLING

displacement: 220 lbs/in and 1200 in-lbs/in respectively at the drive end. These stiffnesses mean that for a maximum misalignment of 10 mils we will have a transmitted shear and moment of 0.40 lbs and 2.2 in-lbs respectively at the drive end. These superimposed forces are independent of speed and cause a negligible drive end spring deflection of 0.002 mils (see Appendix A for the related calculation).

In order to connect the coupling to the drive motor, we cut a mating, internally-splined hub to fit the splined motor shaft (see Appendix A). Connecting the coupling to the rotor was more difficult. For the balancing runs both ends of the rotor have unsupported tubes and wires coming out of the center of the shaft ends. The drive end also has a delicate weld prep extending on the shaft end. The coupling was designed to protect the rotor end and support the plumbing at the drive end. (See Appendix A for the coupling drawing.)

The free end plumbing also had to be supported to keep the heavy copper field leads from flying out under centrifugal body forces. A phenolic laminate tube was machined to extend beyond the rotor shaft end and support these wires (see Appendix A).

V INSTRUMENTATION

V.1 INTRODUCTION

Instrumentation installed to monitor rotor dynamics has two uses:

1) to monitor vibrations which are dangerous and shut the system down if these vibrations become excessive, and

2) to be an aid in balancing where dynamic response to given perturbations must be accurately measured.

In both cases the instrumentation must be accurate. Our design goals were set to an error of less than five percent of total motion amplitude and a phase shift of less than one degree of rotor rotation. The criteria in section I.2 helped dictate where the instrumentation had to be placed to prevent rotor damage. To prevent bearing rub, instrumentation must measure the oil film clearance or rotor bearing displacement at every instant of time. To prevent spring fatigue

failure, the bearing/ground motion, which is virtually all in the spring, can be measured and the instantaneous state of stress deduced from elastic beam theory. Finally, in order to determine whether the bearings rub, due for example to dirt in the bearing oil, accelerometers may be attached to the bearing housings.

To measure the degree of flex in the rotor at high speeds, probes will be mounted in a third plane for determining rotor/ground motion. In order to measure rotational speed and phase angles, angular position instrumentation has been installed.

Finally, the instrumentation signals must be processed into a usable form. Some of the information must be used to detect dangerous vibrations. Circuitry must be built which decides if the machine should be shut down and then do so automatically.

In addition to the above specifications, the electric circuitry to be built must be inexpensive compared to similar equipment used industrially. It is hoped that by custom designing the instrumentation a cost savings can be realized. In fact, all of the circuits built to the above specifications cost about $1000.00 (not including proximity probes which cost $3000.00) compared to about ten times that for industrial circuitry performing the same task. In general, analog operational amplifier based circuits were used in place of more expensive digital circuits. Digital circuits are generally more easily adapted to a wider range of systems; however, if one knows the requirements (such as response time, expected operating speed, and

location of critical speeds) in advance, then good inexpensive analog circuitry can be built and permanently installed.

V.2 VIBRATION TRANSDUCERS

V.2.1 BEARING/GROUND MOTION

Virtually all of the bearing/ground motion occurs in the beam-type springs (see figure V.2.1) which support the bearing housing. Since the beams have a rectangular cross-section, it is convenient to install strain gages which measure the X- and Y-direction motions separately. The strain gages used were Micro-Measurements #CEA-06-125UW-350 350.0-ohm gages bonded with Micro-Measurements AE-10 epoxy compound. This choice of strain gage and bonding compound is known particularly for ease of application. The bonding compound was cured for six hours at fifty degrees celsius. This cure gives the bond excellent fatigue properties without annealing the AISI 4140 steel springs. There can be zero shift with this gage due to temperature changes and long term cyclic use. However, we are only interested in dynamic motion. By filtering DC offset, zero shift, which has a time constant orders of magnitude greater than the bearing/ground motion, is also filtered.

The gages, as seen in figure V.2.1, are mounted in half bridge pairs. The inactive half of the bridge consists of precision, military specification, 350.0 ohm resistors. (For excitation and calibration see sub-section V.4.2). Four sets of strain gages were mounted which indirectly measure displacement in the X- and Y-directions at the free and drive end bearings.

The major source for error is cross-coupling which can introduce phase and magnitude error in determining the runout phasor for influence coefficient balancing. Cross-coupling can occur if a strain gage is not centered properly. If the motion is separated into X and Y components, then the rectangular beam-type spring will have a neutral axis for each motion (see figure V.2.2). Since both motions occur simultaneously, it is important that each gage measures one type of motion only.

For example, vertical bearing motion strains all of the top spring fibers evenly. A strain gage placed on the bottom or top will measure vertical bearing motion. If the gage is mounted aligned with the neutral axis for horizontal motion as shown in figure V.2.3; then, while half of the gage is increased in length, the other half is compressed by an equal amount. To first order, there is no change in the gage resistance due to horizontal motion. If, however, the strain gage were mounted off center by an amount, δ , on a spring two times Δ wide (see figure V.2.4), then the error could be quantified as a percentage of the horizontal motion detected in a vertical motion strain gage. For an elastic beam obeying Hooke's law, the strain distribution increases

linearly from zero at the neutral axis as shown in figure V.2.3. Therefore, the error is

$$\% \text{ error} = \frac{\text{horizontal motion detected}}{\text{maximum vertical deflection}} \times 100\% \qquad (V.2.1)$$

$$= \frac{\delta}{\Delta} \times 100\% \quad .$$

After the strain gages were installed, the maximum δ measured was 0.010 inches. Δ equals 0.25 inches in this case. The numerical error using equation V.2.1 is,

$$\% \text{ error} = \frac{0.010}{0.25} \times 100\% = 4\% \quad . \qquad (V.2.2)$$

The phase error was found experimentally using the set-up in figure V.2.5. The rotor was run at 1000 RPM in the shaking mode. The proximitor and strain gage traces were examined on the Nicolet digital oscilloscope for a phase difference. No phase error could be found.

Another source of strain gage error is non-linearity in the springs. It has been predicted [40] that the springs will remain linear even at the maximum peak-to-peak motion of eight mils. That is to say that phenomena such as yielding or superimposed spring tension should not occur to first order. There is little that can be done about non-linearities except to balance the rotor iteratively until the amplitudes are low enough that the system approximates a linear system.

In order to design the excitation circuit of sub-section V.4.2, it was necessary to approximate the transfer function, voltage-in divided by voltage-out, of the strain gage as a linear function of bearing deflection. The different strain gage circuits should have slightly different transfer functions, but they are all on the same order. We would first like to maximize this gain in order to reduce signal noise between the gages and the voltage measuring device. The moment along the beam (see figure V.2.6) is

$$M(x) = EI \frac{d^2y}{dx^2} = p(x - \frac{L}{2}) \quad . \qquad (V.2.3)$$

Integrating V.2.3 twice and applying the boundary conditions, zero slope at each end and zero deflection at x=0, we obtain the vertical deflection

$$y = \frac{PL^3}{12EI} \qquad (V.2.4)$$

The maximum bending moment occurs equally at either end of the beam but with opposite sign. We therefore wanted to locate the strain gages as closely as possible to one end of the spring. Since the strain gage length is 0.440 inches, the closest that the gage center could be located to one end is 0.220 inches from the base of the end radius of the spring. As a representative numerical example we may analyze the drive end, vertical spring deflection.

We solve V.2.5 for the loading shear force, P.

$$P = \frac{-12EI}{L^3} y \qquad \text{(V.2.5)}$$

The moment at x inches from one end is

$$M(x_0) = \frac{-12EI}{L^3} (x_0 - \frac{L}{2}) y \qquad \text{(V.2.6)}$$

The stress for a unit deflection would then be

$$\sigma(x_0) = \frac{M(x_0)c}{I} = - \frac{12E}{L^3} (x_0 - \frac{L}{2}) yc \qquad \text{(V.2.7)}$$

By Hooke's law the strain is then

$$\varepsilon(x_0) = \frac{\sigma(x_0)}{E} = - \frac{12}{L^3} (x_0 - \frac{L}{2}) cy \qquad \text{(V.2.8)}$$

If L equals 3.5 inches, c equals 0.225 inches, and x equals 0.22 inches, then the strain is 0.096 inches-per-inch per inch of vertical bearing deflection.

The gage factor for this gage is 2.08. Therefore the change in resistance for each gage will be

$$\Delta R = (2.08)\, \varepsilon(x_0) R \quad . \qquad \text{(V.2.9)}$$

Then the transfer function [20:pp368-9] for small strains is

$$\frac{V_{out}}{V_{in}} = \frac{2\Delta R}{R} = 2(2.08)(\varepsilon) \qquad \text{(V.2.10)}$$

$$= 0.40\ y\ \frac{\text{volts}}{\text{volt}} \quad \text{per inch of bearing/ground deflection.}$$

Micro-Measurements Co. suggests a maximum excitation voltage (voltage-in) of 10 volts to prevent overheating in this application. Multiplying this voltage-in by the transfer function we arrive at a voltage-out value of 17.8 volts for each inch of deflection or 4 millivolts per mil of deflection. Since we plan to use an industry standard of 200 millivolts per mil we need to amplify our signal on the order of 1000. We multiply the voltage-out signal by a gain of 1000 using an inexpensive precision decade amplifier to give 4,000 millivolts per mil and then adjust the voltage-in downwards using a trim-pot.

A circuit diagram of the strain gage wiring is given in Appendix B. Calibration of and signal processing for the strain gages is discussed in sub-section V.4.2.

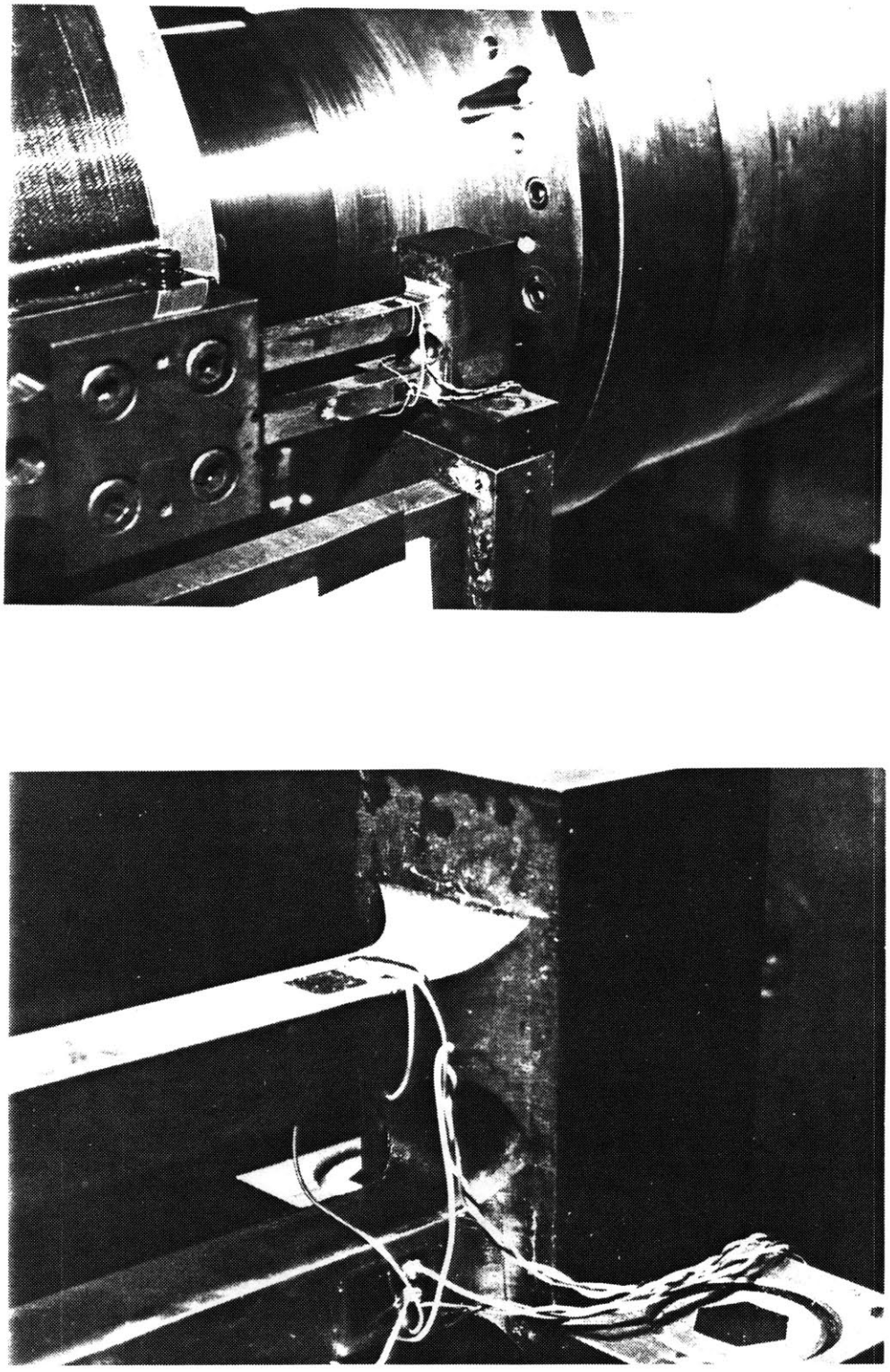

FIGURE V.2.1 DRIVE END BEARING SUPPORT SPRINGS WITH ATTACHED STRAIN GAGES

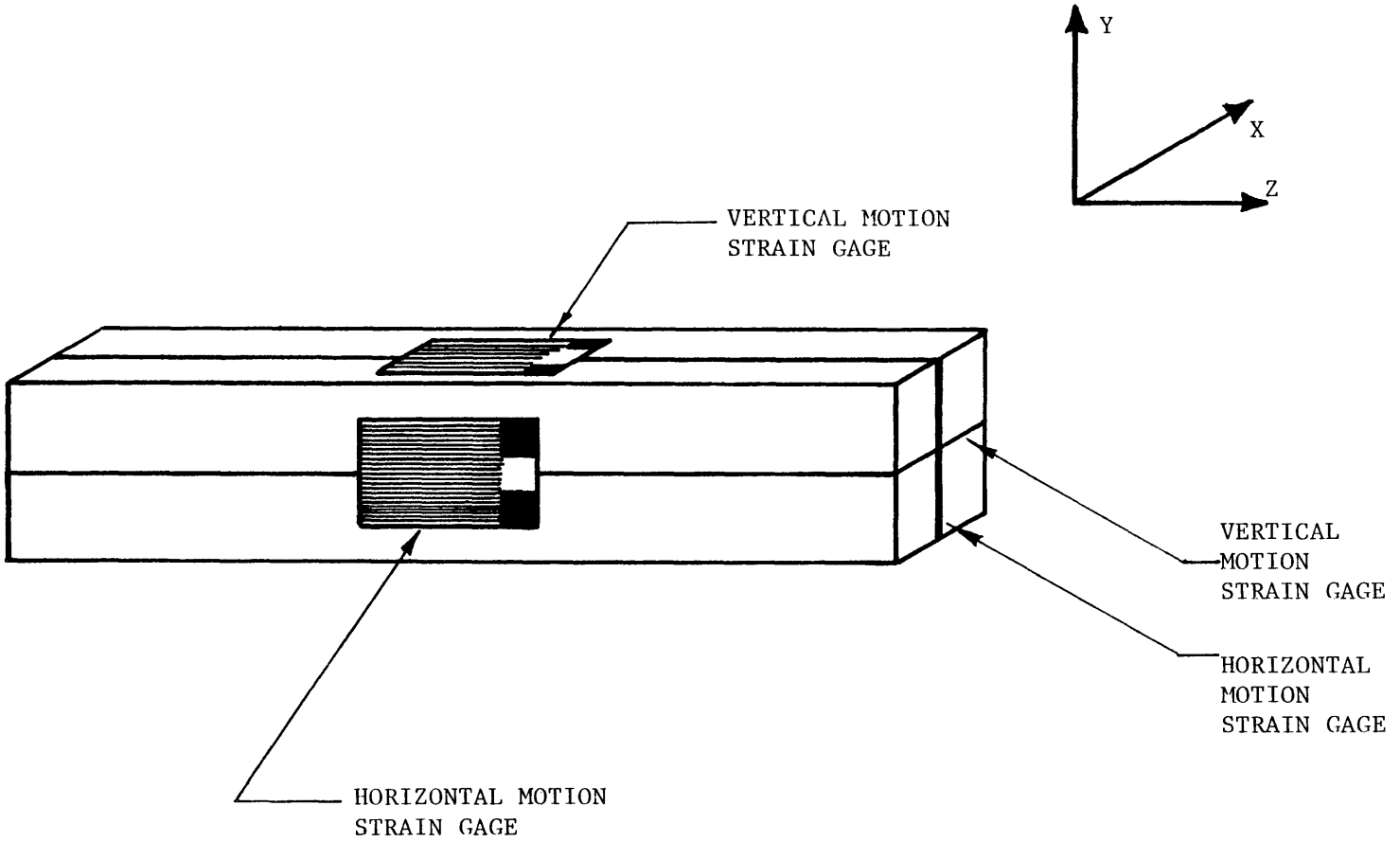

FIGURE V.2.2 SECTION OF SPRING WITH ATTACHED STRAIN GAGES

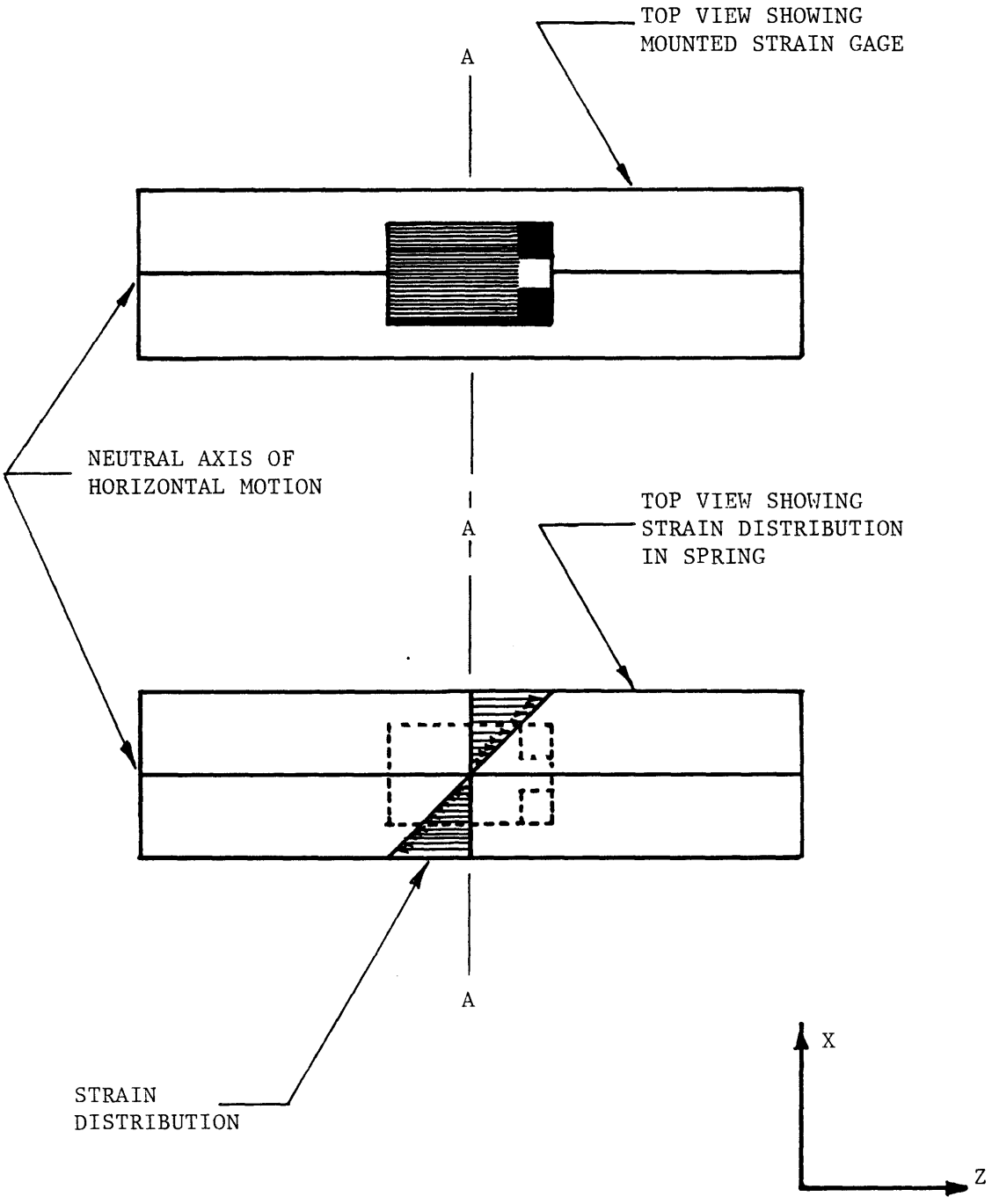

FIGURE V.2.3 TOP VIEWS OF SPRING WITH STRAIN GAGE

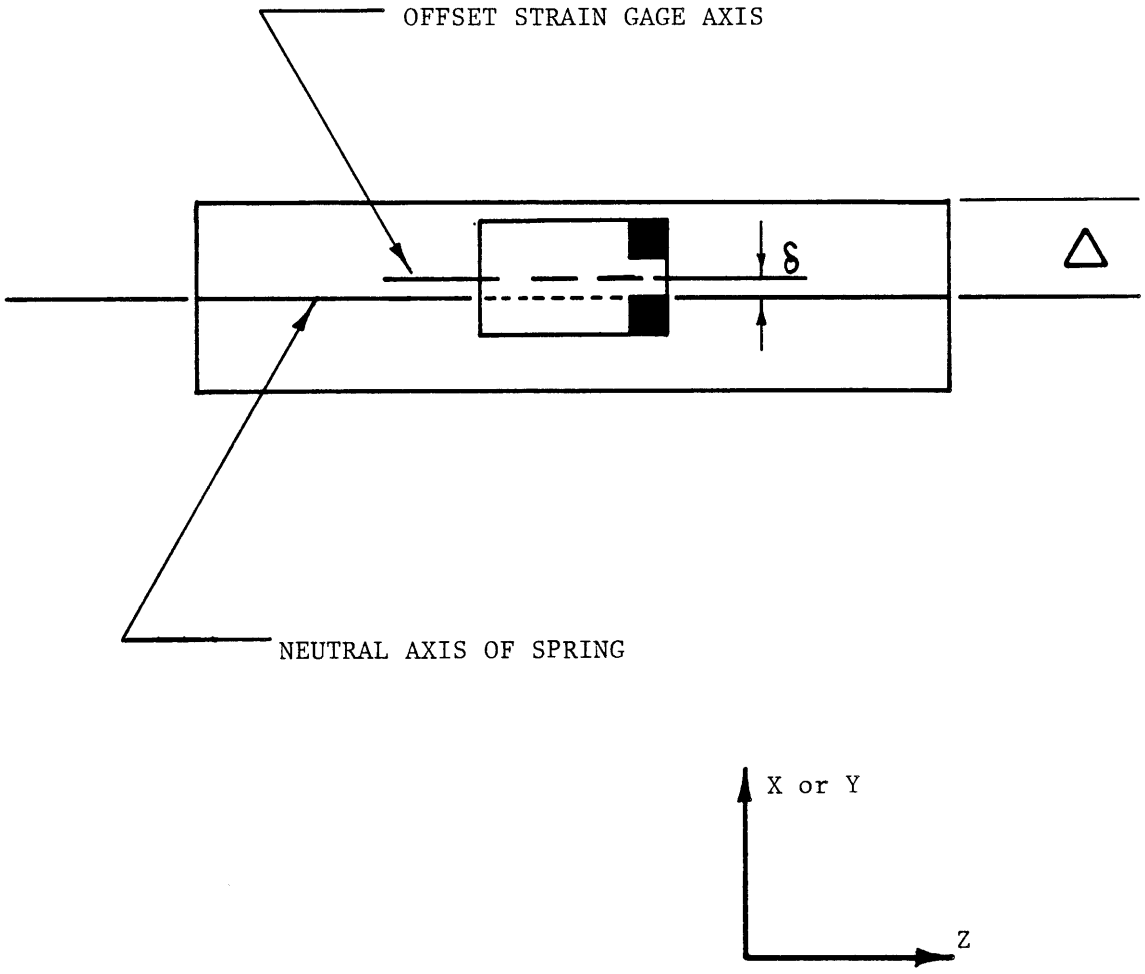

FIGURE V.2.4 STRAIN GAGE OFFSET CROSS-COUPLING ERROR

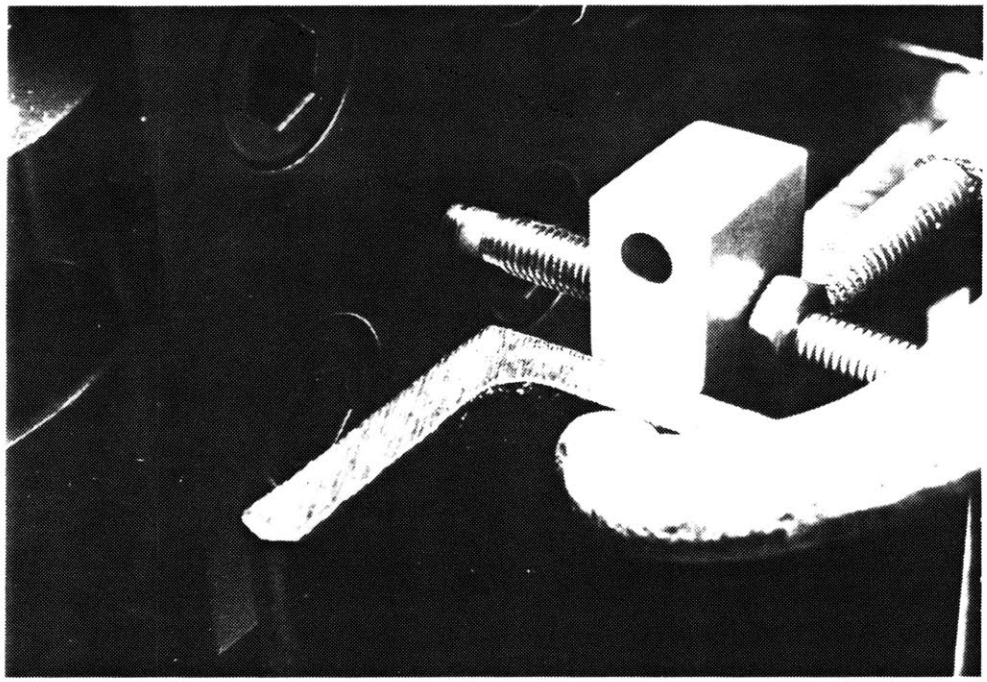

FIGURE V.2.5 STRAIN GAGE CALIBRATION USING A PROXIMITY PROBE

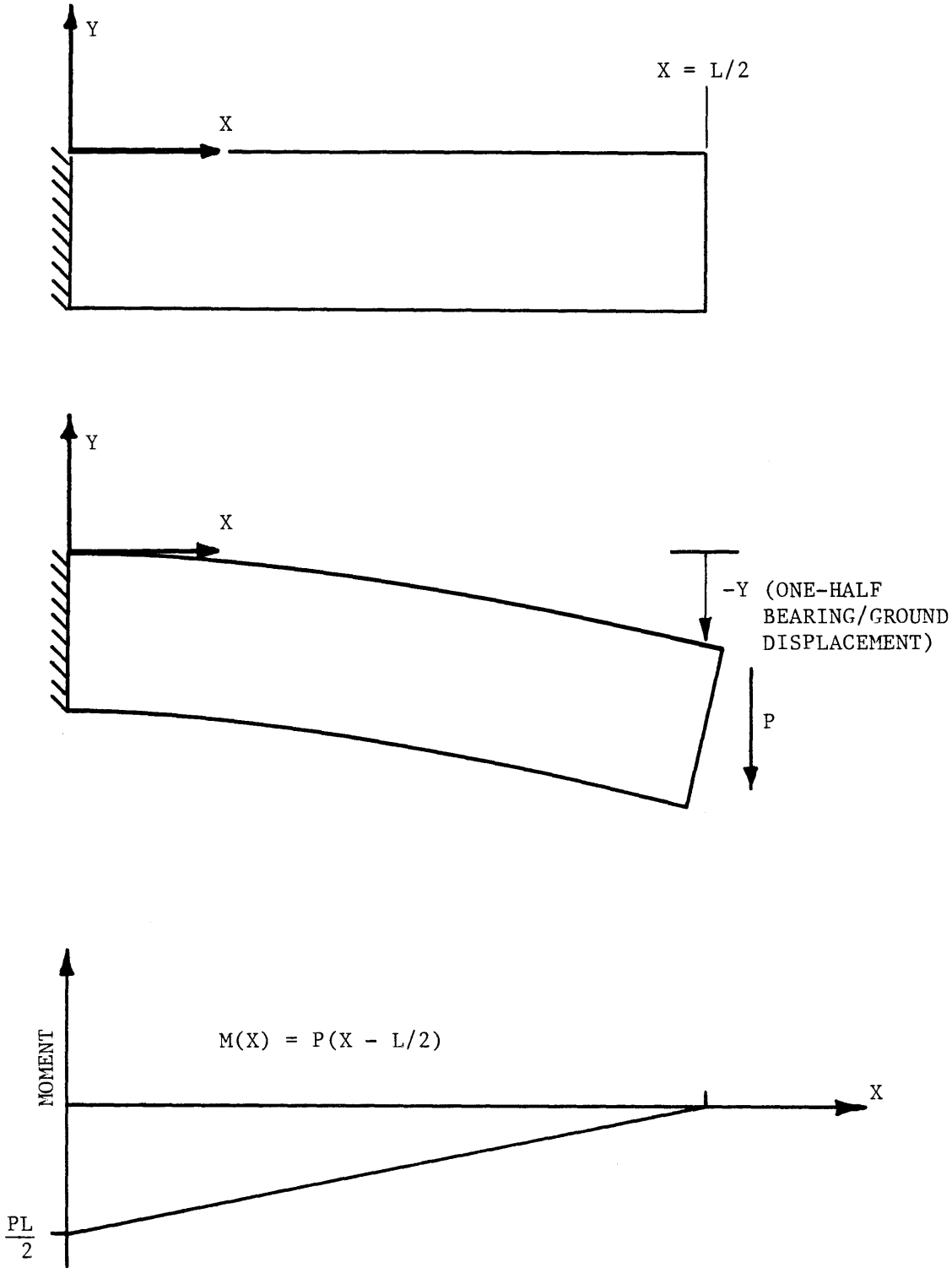

FIGURE V.2.6 SPRING DEFLECTION

V.2.2 ROTOR/BEARING MOTION

Rotor/bearing motion was measured using Bently-Nevada 7200 series, 5-millimeter proximity probes. Each probe has an oscillator/demodulator called a proximitor (see figure V.2.7). The proximitor sends a radio frequency signal to the probe. The probe consists of an induction coil encased in a protective housing. The induction coil induces eddy currents in the target material which dissipates I^2R power. The power loss is a function of the distance between the probe tip and the target material. The proximitor measures the power loss, and for given material properties can output probe/target distance in DC voltage (200 millivolts per mil displacement) over a range of 70 mils for the AISI 4340 steel rotor shaft. Since the clearance between the shaft journal and the bearing pads is 20 mils maximum on the diameter, a 70 mil range for the probe is acceptable.

In order to measure true rotor/bearing motion, it is desirable to measure at the axial center plane of the bearing. A probe could have been mounted between two adjacent tilting pads in the vertical direction only. However, the clearance between pads is small enough that some I^2R power from the proximitors would be dissipated in the pads in addition to the target surface and cause errors in vibration measurement. The nearest location where the probe tip can have adequate sideways clearance is outside of the aluminum oil seals located four inches away

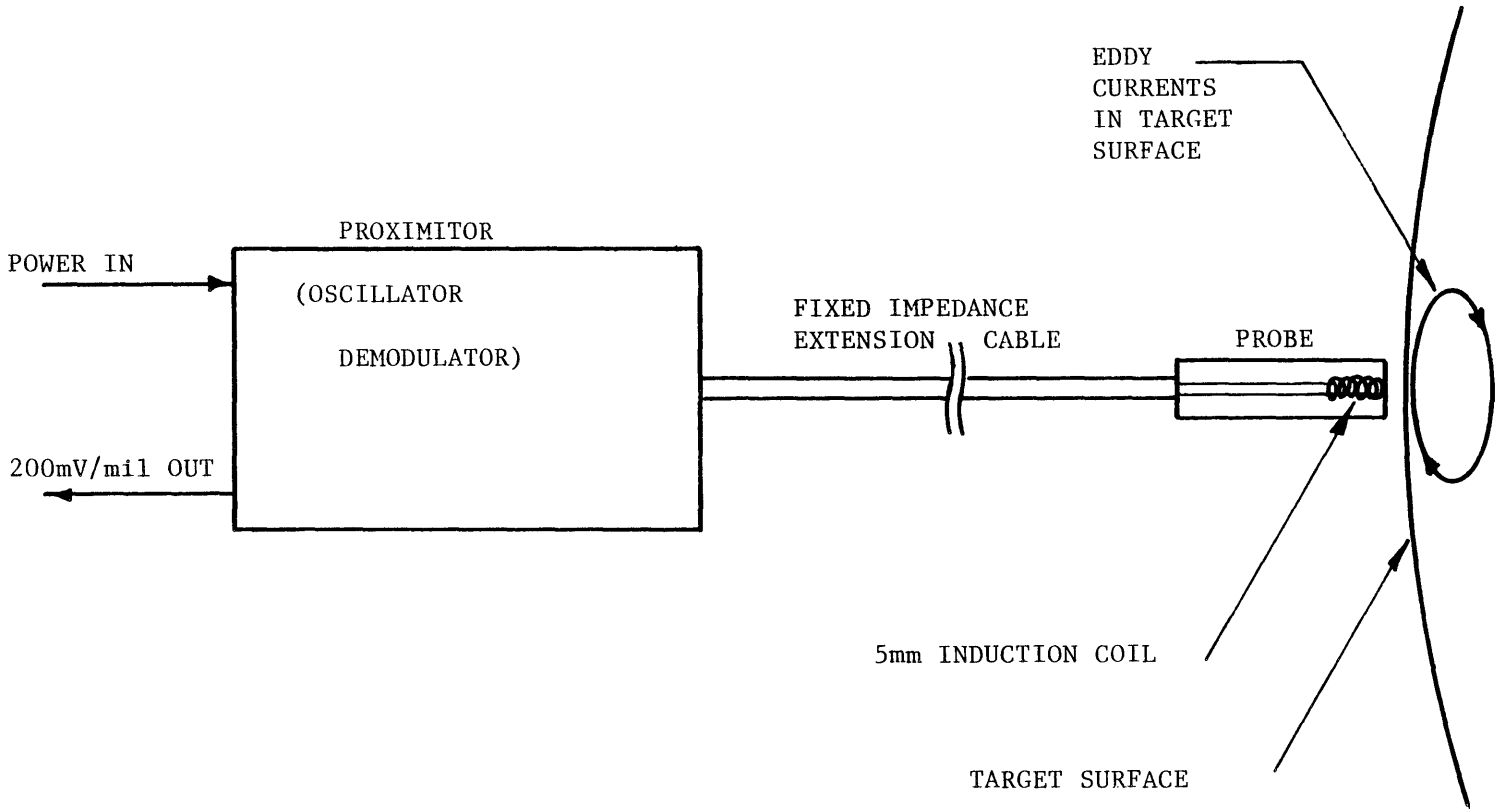

FIGURE V.2.7 PROXIMITOR AND PROBE

from the bearing center plane. The proximity probes are mounted in the X- and Y-directions at each bearing oil seal nearest the free end (see figure V.2.8). Herein lies a source of measurement error. To first order, this fractional error (see figure V.2.9) is equal to

$$\text{error} = 4.0 \sin\theta \text{ inches} \qquad \text{(V.2.11)}$$

where, for a rigid rotor, the maximum θ value for deflection relative to the other end in the rocking mode is approximately

$$\theta \cong \tan^{-1}\left[\frac{\text{(max. spring deflection drive end)-(max. spring deflection free end)}}{\text{bearing/bearing distance}}\right]$$

$$\cong \tan^{-1}\left[\frac{\Delta_a - \Delta_b}{96 \text{ in}}\right] \cong \frac{\Delta_a - \Delta_b}{100 \text{ in}}$$

assuming $\theta << 1$ radian. (V.2.12)

So the fractional error is,

$$\text{error} = 0.04(\Delta_a - \Delta_b) \qquad \text{(V.2.13)}$$

Therefore, the maximum error is 4 percent of the true rotor/bearing motion since $|\Delta_a - \Delta_b|$ is expected to be 10 mils. The key is that, as the rotor becomes better balanced in the rocking mode, the absolute error is reduced proportionately. The error should not therefore affect balancing except by making the process more iterative; however, the error should be considered in setting limits for severe

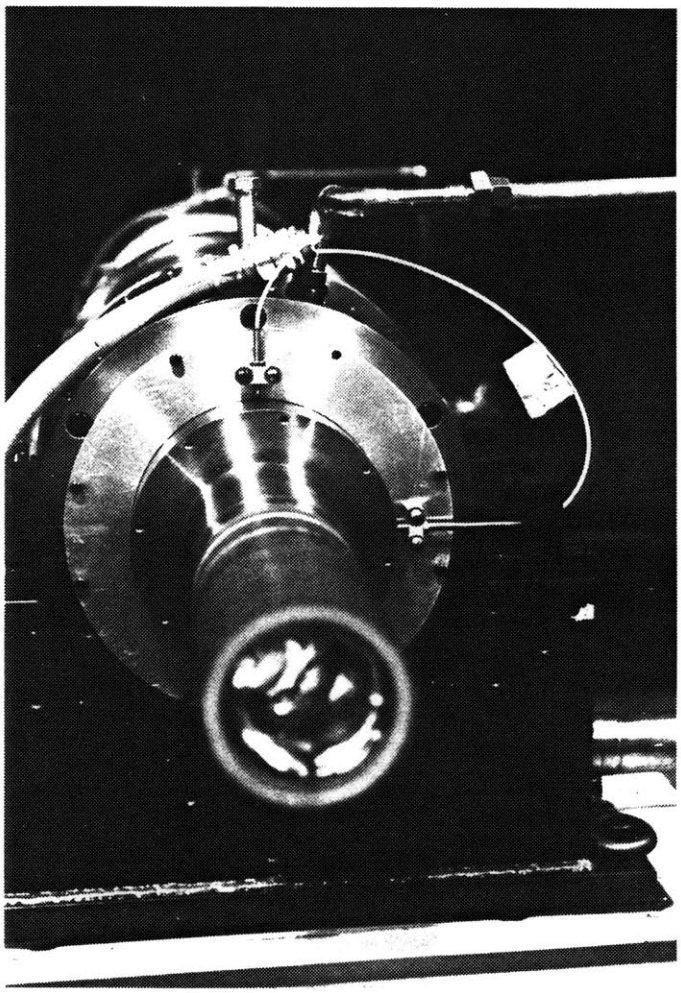

FIGURE V.2.8 FREE END X- AND Y-DIRECTION PROXIMITY PROBES

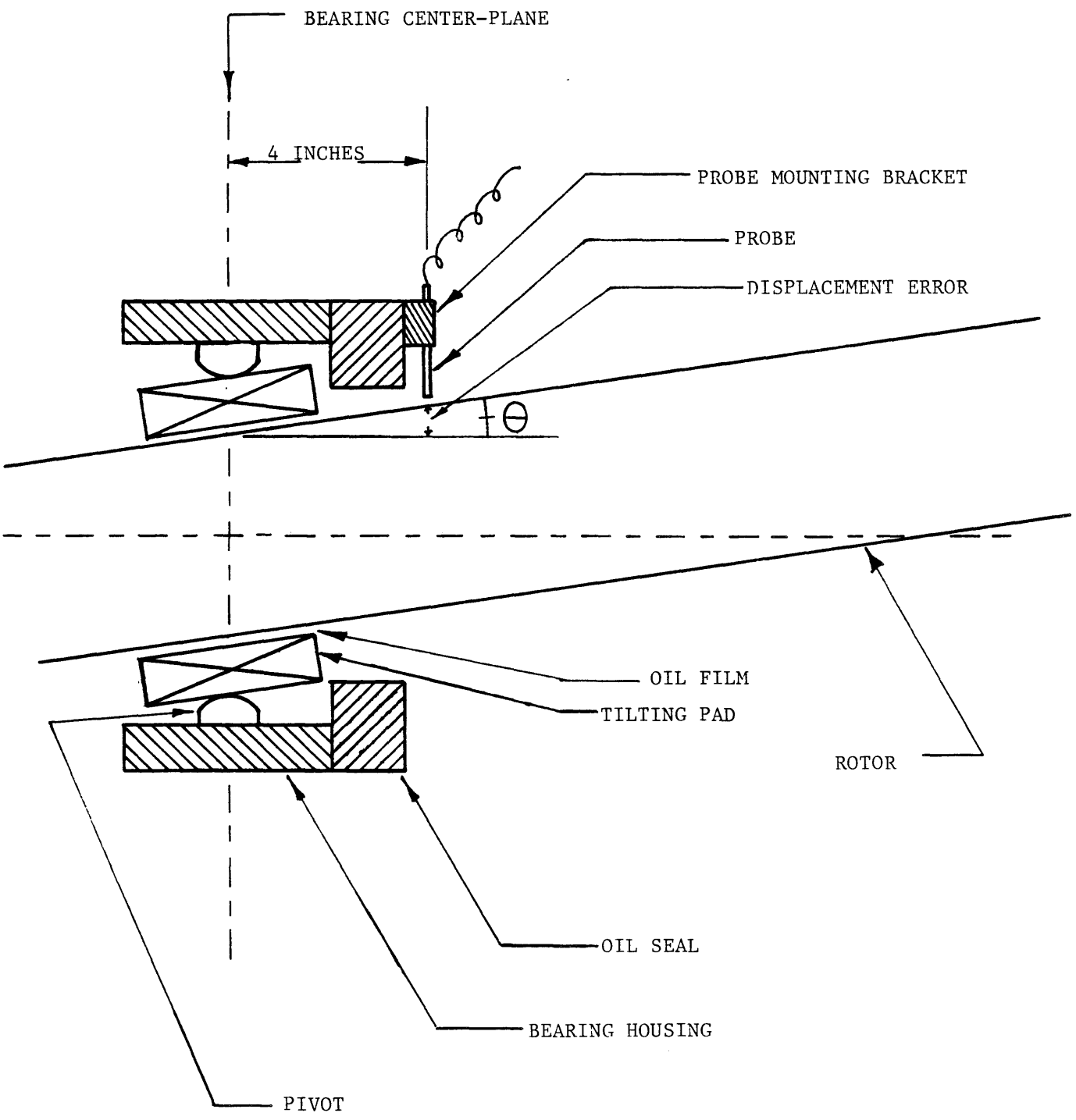

FIGURE V.2.9 PROXIMITOR MEASUREMENT ERROR AT BEARING

vibration. One should allow 0.5 mils less rotor/bearing motion than that estimated to cause system damage.

V.2.3 BEARING RUB VIBRATION

Past experience has shown that, when rotor parts rub stationary parts, the resulting vibration is usually excited in the megahertz range [private discussion with Prof. R. Lyon]. The probes are in a good location to detect this type of vibration. Unfortunately, the probes have a cutoff frequency at 10,000 hertz.

A reliable method of detecting this vibration is to use a standard accelerometer. Most accelerometers are designed to operate in the megahertz range [6:92-6]. We could build a megahertz range band pass filter and sample the strength of the vibration frequency passed. If the signal surpassed a certain power density in the normally quiet megahertz region of bearing housing vibrations, then the rotor could be shut off automatically.

V.3 ANGULAR POSITION MEASUREMENT

In order to measure phase angle and rotational speed, we built a sensor to detect when a chosen reference mark on the rotor aligned with a chosen stationary reference. The rotating reference was the A-pole center. The stationary reference was the positive X-direction. To measure phase angle an assumption is made here that the angular velocity is constant. This assumption is justified because: 1) the balancing runs are made at fixed speeds and 2) the inertia is high compared to any variations in damping.

A TRW #OPB708 light-emitting-diode, photon-base transistor pair was used as a photo pickup. We painted the drive coupling flat black and attached a piece of white tape, one inch wide along the circumference. The LED beams a small light at the rotating target surface. When the black surface passes through the target area, little light is reflected. When the white surface passes through the target area, light is reflected to the transistor base. The photons act as a base current which regulates the collector current in proportion to the amount of light hitting the base and the beta value of the transistor. This relationship is

$$i_c = \beta i_b \qquad (V.3.1)$$

where,

i_c = collector current,
i_b = base current.

Furthermore (see figure V.3.1), the voltage drop across the transistor, when it passes current will be linear and the slope, is

$$\frac{dV}{dt} = \frac{i_c}{C} \frac{\beta i_b}{C} \qquad (V.3.2)$$

The only capacitance which the circuit sees here is the line capacitance. The line capacitance measured (1050 picofarads) was necessarily high because the signal processing circuits are located 20 feet distant from the pickup. The high capacitance in this circuit makes the voltage slope in figure V.3.1 small. Especially if the reflective tape becomes dirty, then at high speeds the voltage pulse might drop off slowly enough to create phase error.

In addition, we have some error at the trailing end of the reflective tape. At this point the transistor is switched off, and we have an RC circuit in which the voltage rise is exponential.

$$V = 15e^{-t/\tau} \text{ volts} \qquad (V.3.3)$$

where the time constant is,

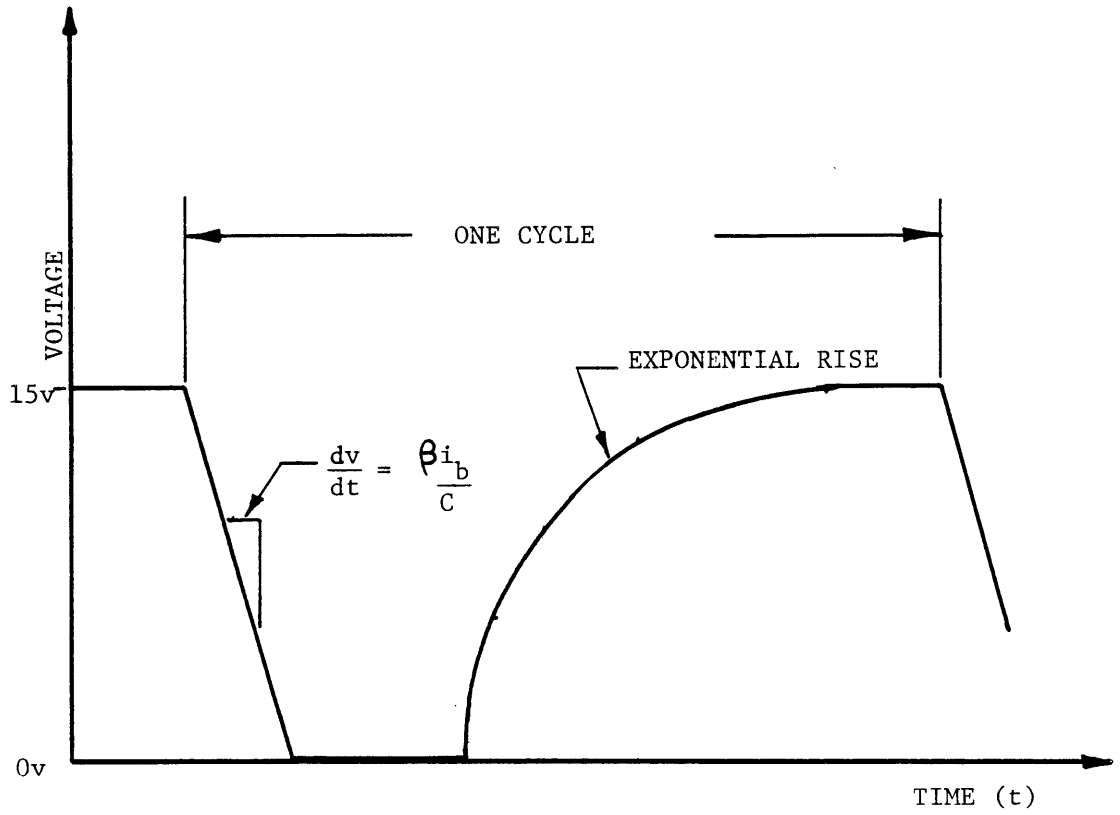

FIGURE V.3.1 IDEALIZED WAVEFORM OF THE ANGULAR POSITION PULSE

$$\tau = RC = 0.29 \text{ milliseconds} \qquad (V.3.4)$$

In order to drive the signal more accurately through the 20-foot cable we added an amplifier at the probe using another transistor. The signal is amplified by an amount, beta, which is roughly equal to 100. Therefore the leading slope of the pulse is 100 times steeper. This waveform definition is important so that the signal processing circuits can distinguish the pulse from noise without phase error.

V.4 SIGNAL PROCESSING

V.4.1 INTRODUCTION

The signal processing circuits are included in one physical location and do the following:

* filter DC lateral vibration signals,

* calibrate probe and strain gage signals to the industry standard of 200 millivolts per mil of deflection,

* sum the bearing/ground and rotor/bearing motions,

* output bearing/ground, rotor/bearing, and rotor/ground motion for each bearing in the X- and Y-directions,

* output angular position,

* output digital speed to an LED readout,

* output analog speed and vibration amplitude for plotting magnitude verses speed, and

* shut down the prime mover in case of dangerous vibration amplitudes.

The remainder of section V.4 explains the circuit designs. See the circuit diagrams and circuit layouts included in Appendix B.

V.4.2 PACKAGING

For simplicity, all of the signal processing circuits were built into a single box. Easy access for calibration and ease of use were important design factors. Many of the signals will carry low power 60-hertz signals when the rotor is turned at synchronous speed. It is important therefore to isolate the circuits from 60-hertz ground noise. We use two small transformers within the electronics package to step down the 120-VAC wall current to 30 VAC. The transformed voltage is rectified, filtered, and regulated to 15 VDC, -15VDC, and -24VDC. A floating ground is used throughout, and the box itself is isolated from this floating ground. The signals are output from the box through ground-isolated, BNC-type connectors. It is important to use coaxial

wire for signal leads so that the leads also have the same floating ground. To guarantee this requirement, all equipment connected via BNC cables should have floating ground.

The package used to house all of the signal processing circuits is shown in figure V.4.1. We used a card rack so that the circuits could be combined with racks for instrumentation on other parts of the rotor in a single cabinet. The cards slide out from the rear. The important circuit layouts and wiring diagrams for these cards are included in Appendix B. Note that the trim-pots are mounted on the rear of the cards for easy accessibility. The BNC output connectors, power light, vibration trip switch light, and trip switch reset are located on the front panel. A Jones strip attached to the underside of the box handles all of the transducer signals, digital RPM pulses, and prime mover shut-down signal wires.

V.4.3 STRAIN GAGE EXCITATION, MEASUREMENT, AND CALIBRATION

Two 350-ohm strain gages form one half of a bridge circuit. Two 350-ohm precision resistors form the other half of the bridge. The bridge is separated. The two strain gages are attached to the bearing support and the two precision resistors remain in the electronics

WILN-OTTE CO.
DIGITAL SPEED READOUT

SIGNAL
PROCESSING
PACKAGE

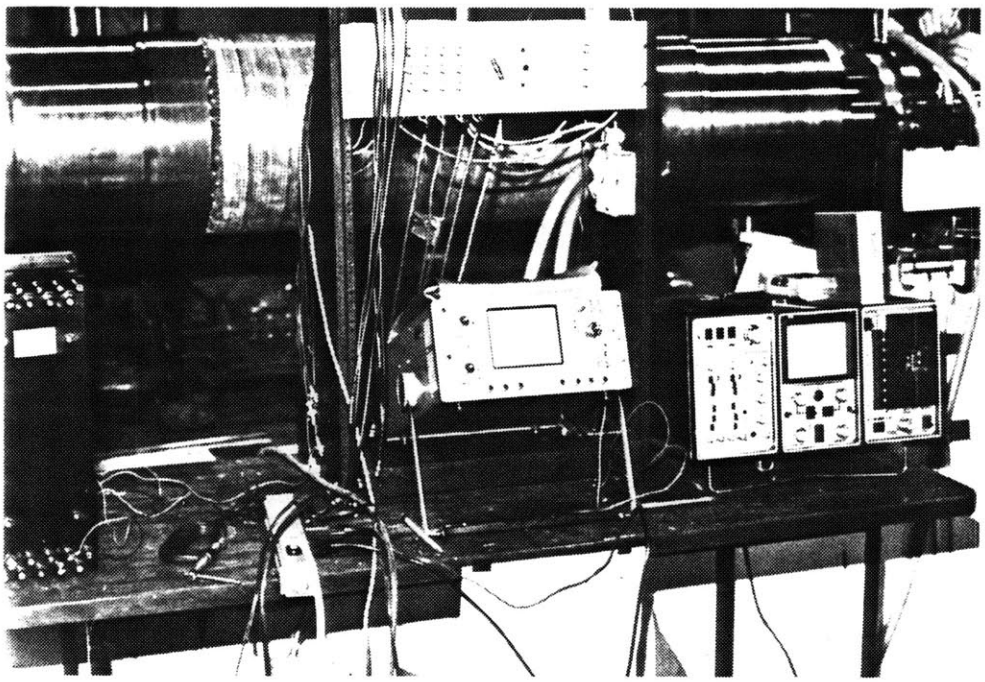

TEKTRONICS
ANALOG
OSCILLOSCOPE

NICOLET
DIGITAL
OSCILLOSCOPE

FIGURE V.4.1 SIGNAL PROCESSING PACKAGE WITH RELATED PERIPHERALS

package. Three twenty-foot coaxial wires of fixed, equal, impedance attach the two bridge halves.

The overall plan involves letting the strain gages measure strain which is linearly proportional to bearing/ground deflection. The strain for a fixed voltage excitation outputs a voltage which is in turn multiplied by a gain to give us 200 millivolts per mil deflection.

We built the circuit described except that fine calibration adjustments are made by adjusting the voltage input to the gages via a trim-pot mounted on the circuit board. A gross adjustment on the voltage-out of the bridge circuit is made by using an integrated decade gain amplifier set in this case to a gain of 1000.

The calibration procedure was performed with the rotor turning at a slow speed of 600 RPM, static unbalance was added to the rotor to induce vibration. A spare proximity probe measured the true bearing motion to ground. (The physical set-up in figure V.2.5 was used for calibrating the X-direction strain gages.) Both traces were fed into an oscilloscope. A new voltage-in at the trim-pot wiper was calculated using the ratio of true probe amplitude to measured strain gage amplitude. This ratio multiplied by the old voltage-in gave the new voltage-in.

At this point in the circuit we have a signal which outputs 200 millivolts per mil of deflection. This signal has some possibly high value of DC offset. To eliminate the offset we built a high-pass RC

filter which passes, with negligible attenuation, vibrations above 3.0 hertz.

It was necessary to bring the signal to the BNC connector on the front panel of the box. In order not to load the system, we added a buffer (shown in the circuit diagram as an operational amplifier). Impedance of the measuring device was assumed to be one megaohm such as with most oscilloscopes. Input current compensation was added to the operational amplifier circuit. This addition was needed to compensate for loading due to the resistor in the high pass filter before the operational amplifier.

To make a power supply of variable voltage within a decade range of 1.0 to 10.0 volts and enough current (up to 35 milliamps) to power one bridge, we used a precision 10-volt regulator chip. The accuracy of the supply determines the accuracy of the output directly. Therefore, the original 15-volt power supply which still has some 60-hertz ripple after rectification and filtering was not used directly. The 10-volt supply is then applied across a trim-pot. The wiper voltage is fed into an operational amplifier acting as a buffer so that we do not load the trim-pot. It is marginal whether the operational amplifier will saturate at the required current. To provide the required current the buffer drives a transistor from the 15-volt power supply.

V.4.4 PROXIMITOR EXCITATION, MEASUREMENT, AND CALIBRATION

This sub-section deals with the probe and oscillator/demodulator as a single unit which from this point will be called the proximitor. The interaction between these two parts is discussed in sub-section V.2.2. The proximitor is powered by a -24 VDC (20-milliamp) power supply. Power for all four proximitors is handled by one of two inboard power supplies. The proximitor as a unit transduces rotor/probe distance into proportional DC voltage. The proximitors are factory calibrated for an AISI 4140 steel target material. The gain of these units is 200 millivolts per mil of deflection. These proximitors, like the strain gages, have DC voltage offsets. To eliminate the offsets, exactly the same circuitry is used in conditioning and buffering the signal as was used in the strain gage circuits. The error due to non-linearity in the expected vibration range is 3 percent [34:p1-5] (see figure V.4.2).

A calibration of one proximitor was made by using a jig which held the probe several fixed distances away from a piece of AISI 4140 target material. The actual distance was measured with feeler gages which gave a calibration to within one half of a mil. Next, pairs of probes were mounted in the same plane to an offset shaft mounted in a lathe. Then,

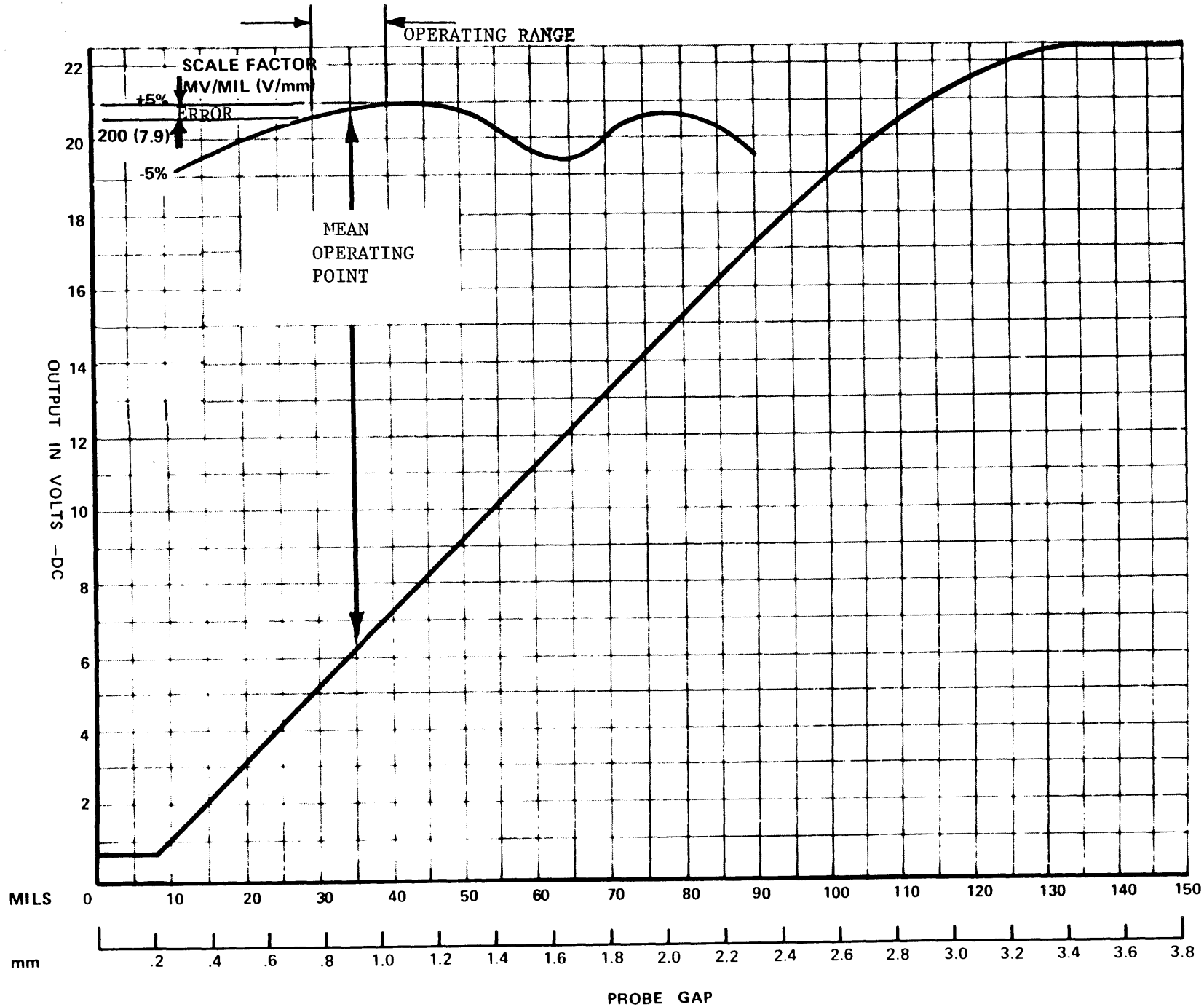

FIGURE V.4.2 PROXIMITOR ERROR DUE TO NON-LINEARITY [34]

using the balance box circuitry and the Nicolet, we found no measurable difference between probes.

An assumption is inherently made that the mechanical, electrical, and magnetic runout of the rotor is zero. If this assumption is false, the circuitry will not compensate for the runout. Two possibilities exist. Firstly, one can rent a microprocessor-based device from Bently-Nevada Co. for $1200.00 per month which will automatically subtract the runout. Secondly, if it is acceptable to analyze the data after a run is completed, we can record the runout at very slow (but constant) rotor speed on the nicolet. Using a Fortran program at the Joint Computer Facility we can match the curves to have the same period with zero phase angle and then subtract the curves point by point.

V.4.5 SUMMING CIRCUIT

The summing circuit was built with the intention of outputting a voltage to the front panel which is proportional to the rotor/ground motion at each bearing in a given X- and Y-direction. This summing may be done by adding the voltages from the rotor/bearing motion and the bearing/ground motion separately for each orthogonal direction at each bearing. Of course the voltages in a circuit cannot be added directly as currents can. Therefore, we built a summing circuit using an

operational amplifier. Both inputs were given equal gain using precision resistors to maintain the 200-millivolts-per-mil calibration.

V.4.6 ANGULAR POSITION PULSE CONDITIONING

The angular position relative to any of the lateral vibration signals is given by a one-pulse-per-revolution signal. The origin of the pulse is explained in section V.3. It is a rough pulse when it reaches the conditioning circuits. The pulse begins at the photo pickup having the form of figure V.3.1. This pulse signal may have some superimposed noise which would confuse a high speed integrated logic chip. The added noise can cause the signal to cross the voltage threshold which makes the chip invert its output thereby creating extra pulses. The circuits described in this sub-section manipulate the raw pulse signal and eliminate problems due to noise.

The pulse signal has four uses. First, the pulsing signal is fed into a digital speed readout unit made by Wiln-Otte Co. Dirt on the leading edge of the reflective tape or superimposed noise could cause the unit to output an incorrect speed. Second, the pulse is used for an analog oscilloscope z-axis input for X-Y plots. For this application the pulse must have a particular shape and size. Third, the pulse is used in balancing as a pointer to locate the A-pole position on a

vibration plot. In this way the phase angle may be determined. Last, the pulse signal is converted to an analog voltage signal proportional to the speed. This voltage is designed to drive an analog X-Y plotter. The design of this last conditioning circuit is discussed in the next sub-section.

All of the uses for the pulse signal described require some common circuitry. The raw signal is fed into an CMOS 4585 integrated-circuit Schmitt trigger. This circuit adds hysteresis so that any small oscillations on the waveform are ignored. The output of this chip is a low-power, 15-volt square wave. The wave repeats once per cycle. Next the signal was buffered by a CMOS 4050B inverting chip. At this point in the circuit the signal is tapped for the z-axis oscilloscope connection and the balancing phase marker. The design needs for these two are the same. The desired waveform shape is shown in figure V.4.3. The waveform is acceptable for the balancing phase marker where the initial spike locates the A-pole, but the shape design was really dictated by the z-axis needs.

The primary purpose of having an oscilloscope z-axis in the rotor application is to identify the whirl direction on an X-Y lissajous figure. If the horizontal and vertical critical speeds are separated, then the lissajous patterns constructed by using X- and Y-direction rotor/ground vibration signals flatten which indicates cyclic stressing of the rotor. If the critical speeds are separated far apart, then the rotor may actually whirl synchronously backwards between the critical speeds and incidentally become unstable.

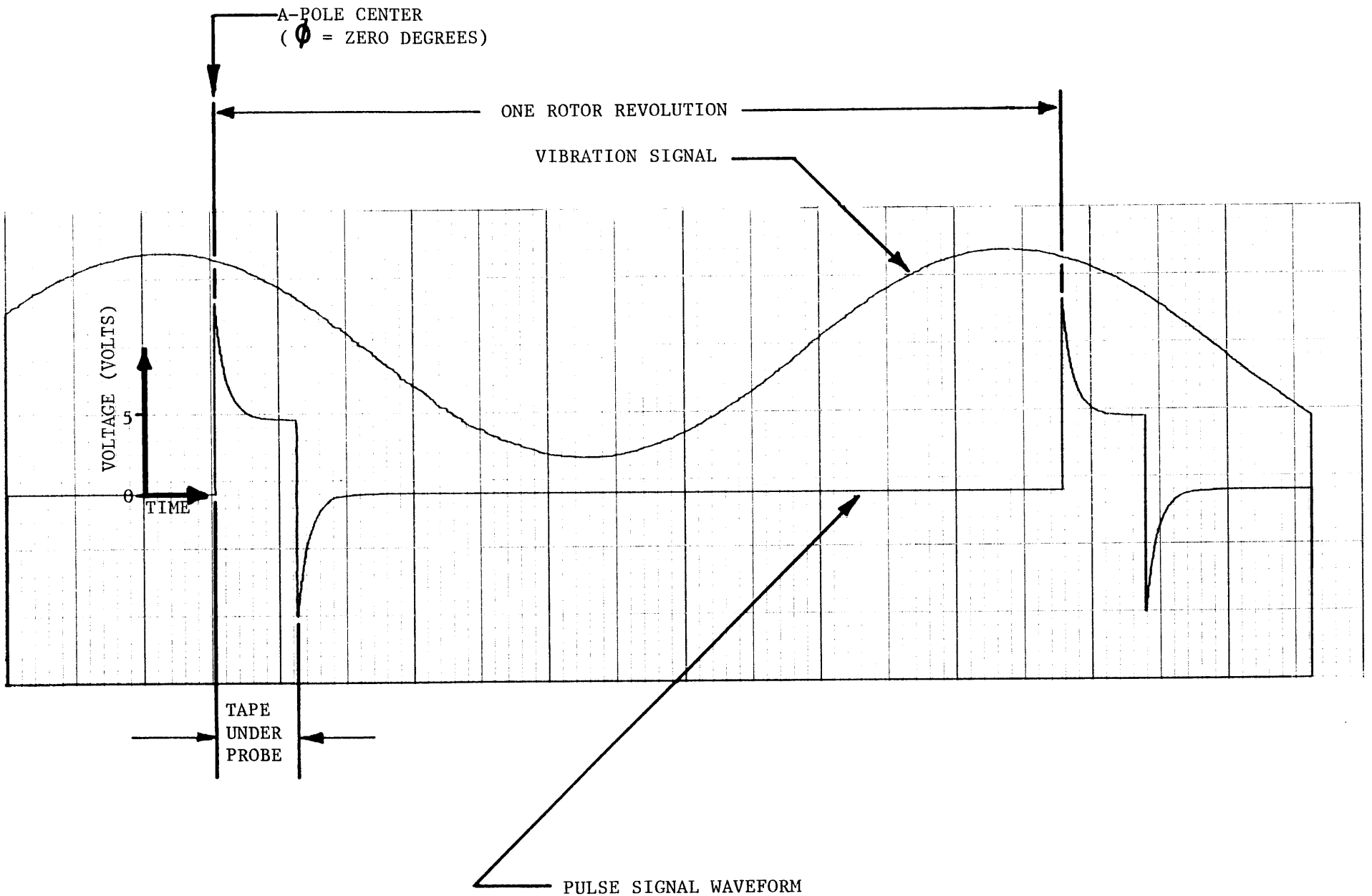

FIGURE V.4.3 PULSE WAVEFORM OF PHASE MARKER

A method of detecting backwards whirl is necessary. At small rotor speeds the direction can be seen directly on an X-Y plot. However, when the rotor is whirling quickly, the instantaneous position or direction of the beam cannot be deduced. Instead the intensity of the lissajous trace is attenuated as a function of a voltage input to the oscilloscope. A z-axis input of 15-volts on a Tektronics analog oscilloscope eliminates the trace completely, whereas less voltage causes less attenuation. The circuit is simple and uses two resistors, a capacitor, and a diode. The desired waveform is a periodic voltage ramp of negative slope beginning at 15 volts. Figure V.4.3 shows how this ramp was approximated. The circuit elements were adjusted by trial and error with an offset mock rotor turned in a lathe at 1800 RPM. The resulting lissajous traces are shown in figure V.4.4. The signal is tapped to a front panel BNC connector to be used for both the balancing phase angle pulse and the z-axis pulse.

The pulse for the Wiln-Otte Co. speed readout device was directed from the CMOS 4050B chip to the Jones Strip via a 220 kilohm resistor to protect the chip from shorts.

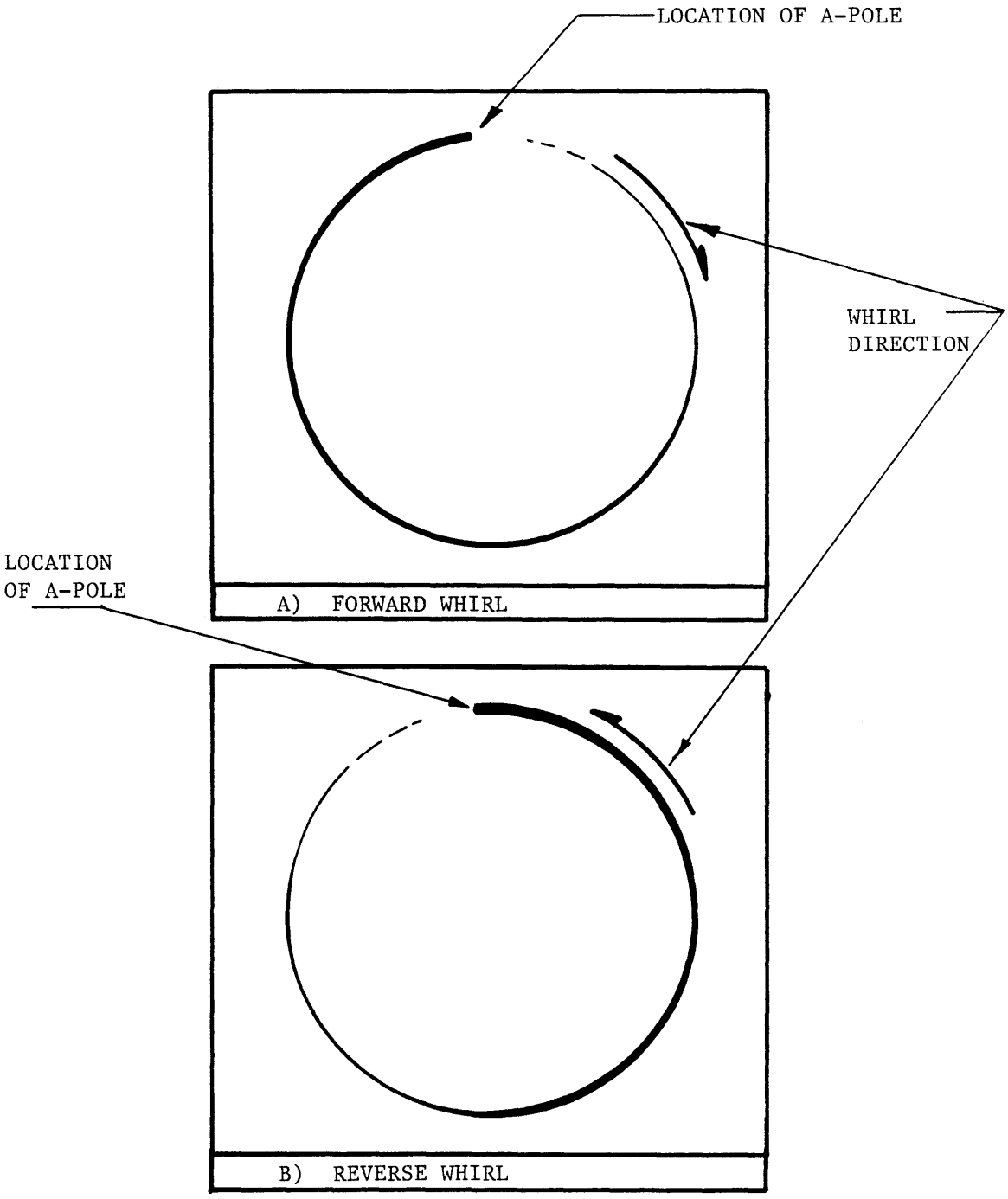

FIGURE V.4.4 OSCILLOSCOPE TRACES OF FORWARD AND BACKWARD WHIRL

V.4.7 ANALOG MAGNITUDE AND SPEED OUTPUTS

It was desired to monitor vibration magnitude verses speed as we accelerated the rotor. In order to do so by using an inexpensive analog plotter, we designed two circuits. One circuit output an analog voltage proportional to rotor speed. The second circuit output an analog voltage proportional to the magnitude of any given lateral vibration signal. The signals were buffered to drive an x-y plotter and then output to the front panel. The magnitude circuit has an input BNC connector on the front panel so that any one of the vibration signals may be monitored.

The analog rotor speed circuit is built as follows. The repeating pulse from the CMOS 4050B chip is fed into a CMOS 4528B multivibrator logic chip. The CMOS 4028B forms a rectangular pulse of constant width set at 8.0 milliseconds by adjusting an external R-C circuit. It begins a new pulse whenever it sees a positive slope on the signal input. As the rotor increases in speed, the rectangular pulse becomes a proportionately larger portion of each period waveform. We use a three-pole Butterworth filter to average the amplitude of this periodic waveform above 10 hertz. This average DC voltage is then proportional to rotor speed. Since the rectangular pulse is 15 volts high and 8.0 milliseconds wide it will equal one full period at 7500 RPM. Therefore,

the analog speed output for speeds greater than 600 RPM (10 hertz) is 500 RPM per volt.

The vibration magnitude circuit is built as follows. The general design is that of a peak detector which tries to follow the envelope of the vibration. We want the output signal to follow fast changes in vibration amplitude yet not follow the actual vibration waveform. A trade-off is involved here (see figure V.4.5). If the time constant RC is too large, the detector will not follow a rapidly decaying vibration. If the time constant is too small, the detector signal will follow the input vibration signal. The time constant was chosen experimentally by using the offset mock rotor.

The input signal is fed from one of the vibration outputs on the front panel, through a BNC cable, to a front panel connector, to the peak detector circuit. The output signal was fed through a low input current, high input impedance, 308 operational amplifier buffer circuit to a front panel BNC connector.

V.4.8 VIBRATION LIMIT CIRCUITS

To protect the rotor during balancing and extended operation, a need exists to limit vibration since large or asynchronous vibrations

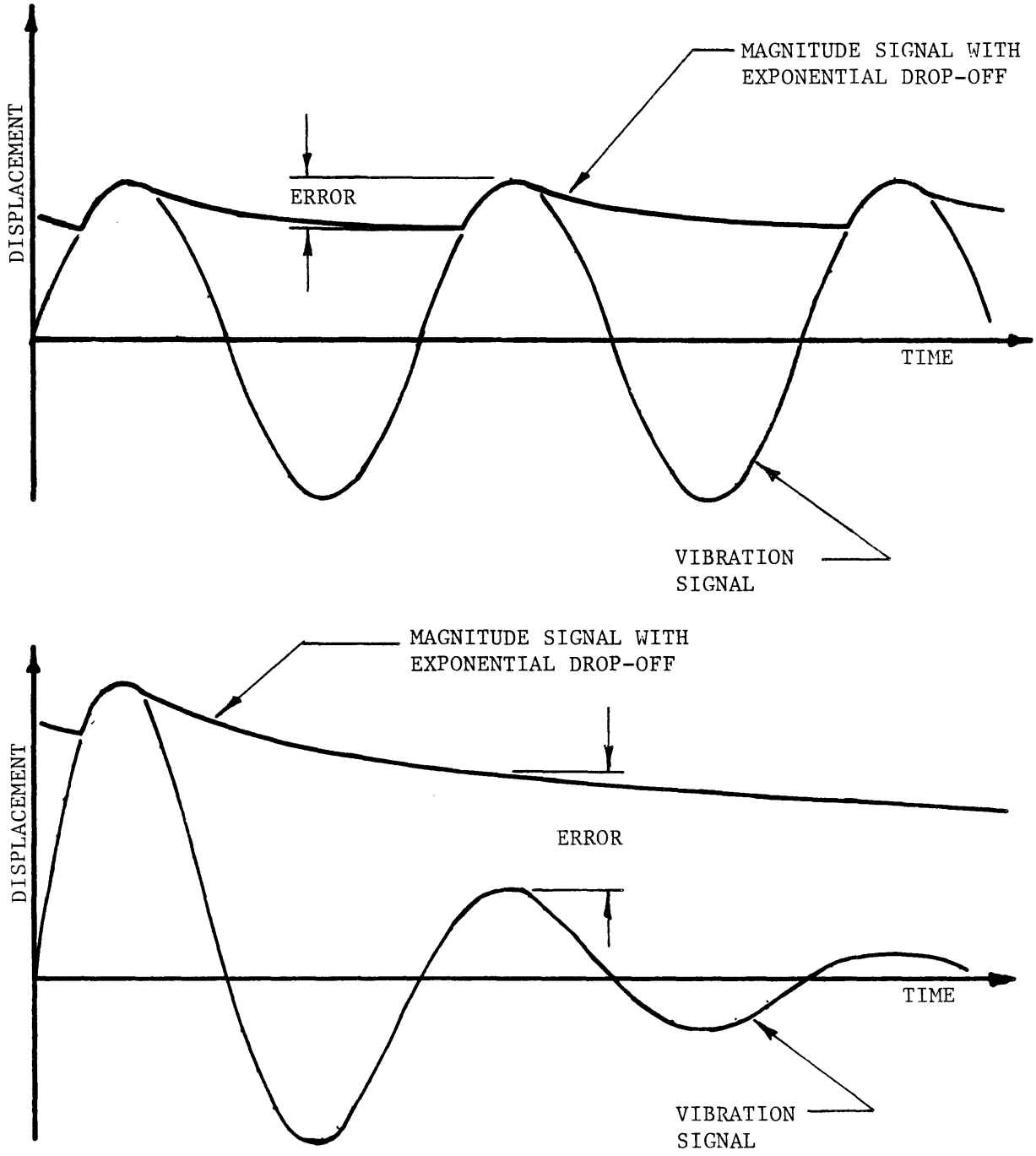

FIGURE V.4.5 ERROR IN THE VIBRATION MAGNITUDE SIGNAL

can be destructive. The general design criteria is to have a circuit which immediately cuts off torque to the rotor and allows it to decelerate away from danger. The specific design goals follow:

* automated shut-down,
* minimal time delay between occurrence of a dangerous vibration and rotor deceleration,
* an operating range from 600 RPM to overspeed,
* individually adjustable trip limits,
* a flag signaling these circuits as the cause of rotor shut-down,
* a reset in order to resume rotor operation.

A total of eight circuits were constructed to monitor eight separate vibrations. The circuits are built as follows: The output of a vibration signal is fed internally to an Analog Devices #AD536AJ RMS-DC converter. The time constant of this converter is set to 100 milliseconds with external capacitors. A short noise pulse of short duration relative to a cycle period is eliminated by the converter. This DC signal is then sent to an integrated-circuit 339 comparator. Whenever the DC signal is above a set reference voltage, the comparator outputs a 15-volt signal; otherwise the comparator outputs zero voltage.

The reference voltage is set by a trim-pot which is tied to the comparator output. The voltage level has hysteresis. If the comparator goes high, reference voltage drops. In this way the comparator never fluctuates. It is on, or it is off. In order to set the voltage limit, the trim-pot wiper voltage to ground should be adjusted.

All of the comparator outputs are tied together. The combined signal goes to a relay which, in the case of the spin tests and balancing, stops the electric motor which drives the hydraulic supply pump to the spin motor. The relay is a double-pole-double-throw switch. Through the normally closed contacts, current flows from the control booth. If this current is interrupted the spin motor shuts down. A latching circuit is included in the relay circuit so that when the vibration exceeds a limit the relay latches itself closed and a flag in the form of a front panel LED is switched on. In order to unlatch the relay, a manual reset switch is located on the front panel.

APPENDIX A

HARDWARE DRAWINGS AND PHOTOGRAPHS

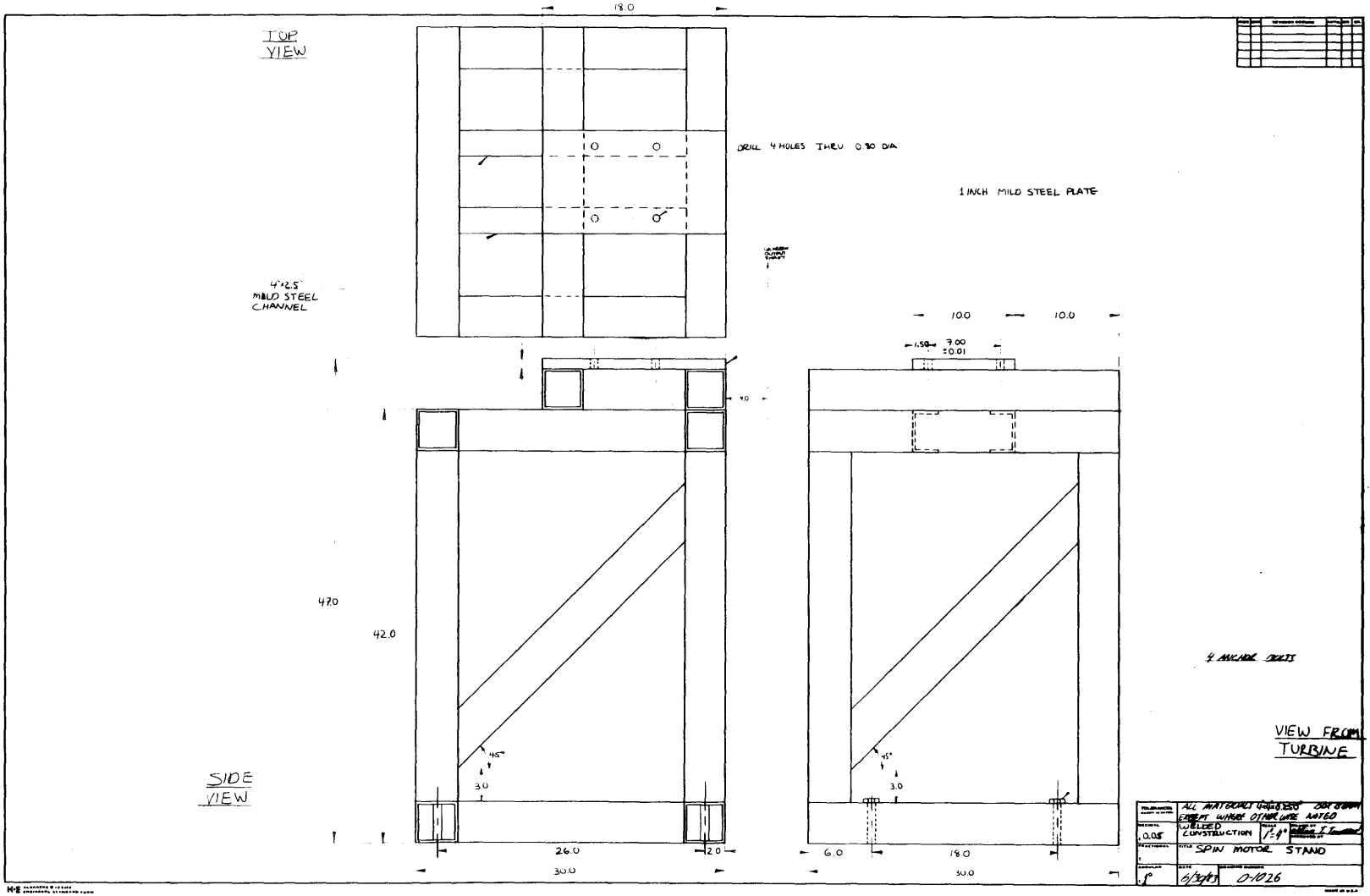

FIGURE A.1 SPIN MOTOR STAND DRAWING

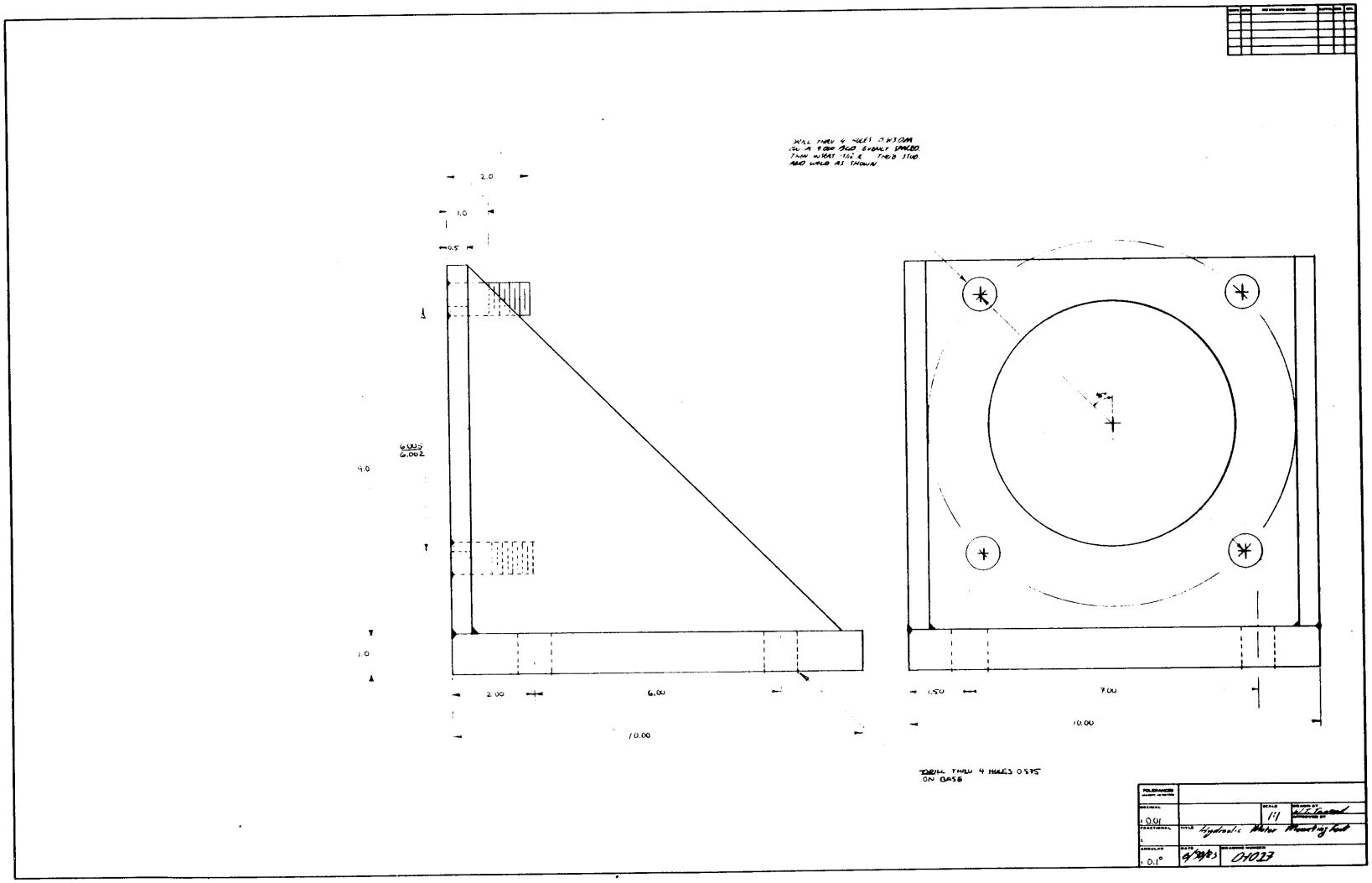

FIGURE A.2 SPIN MOTOR FOOT DRAWING

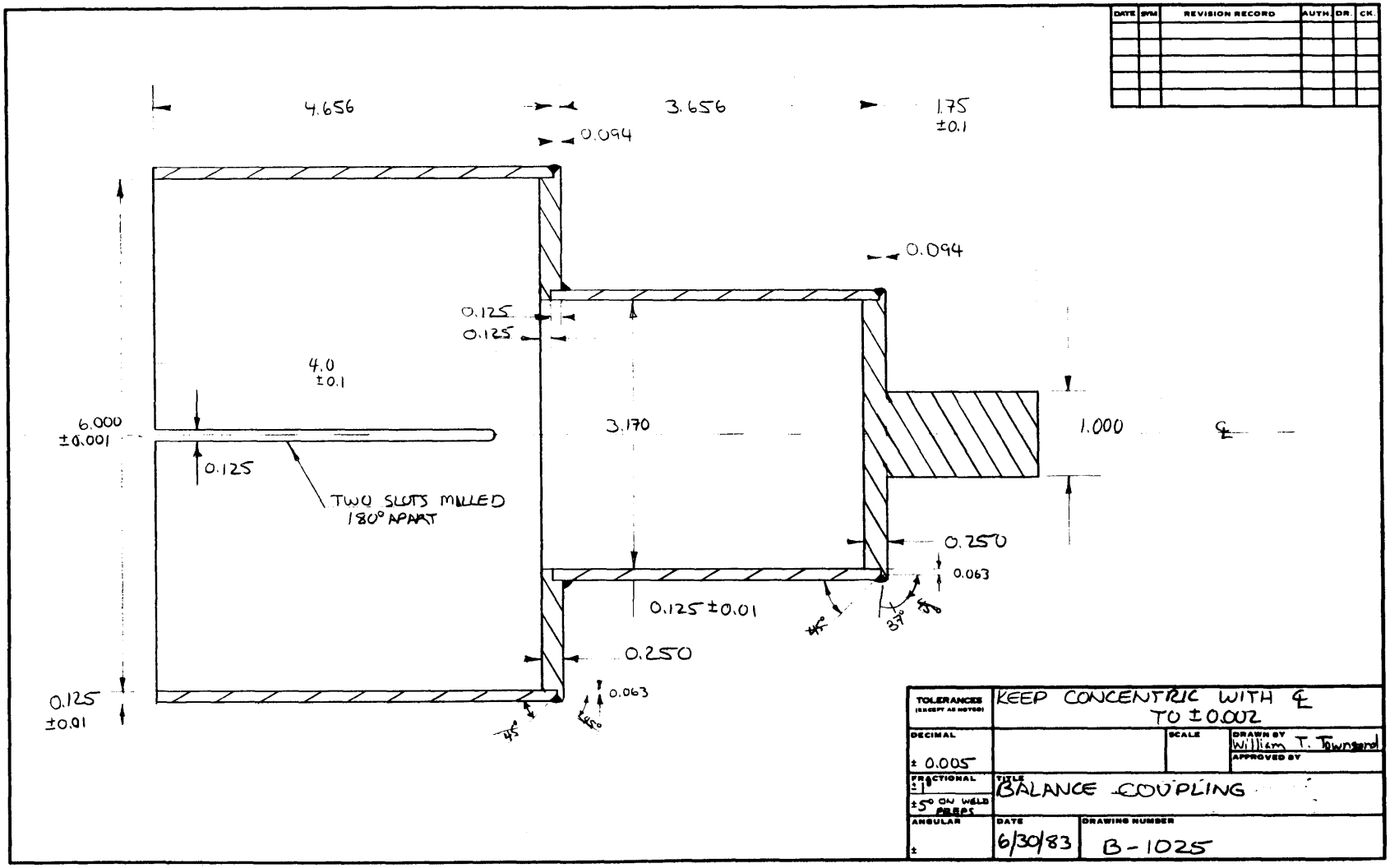

FIGURE A.3 DRAWING OF ROTOR END OF DRIVE COUPLING

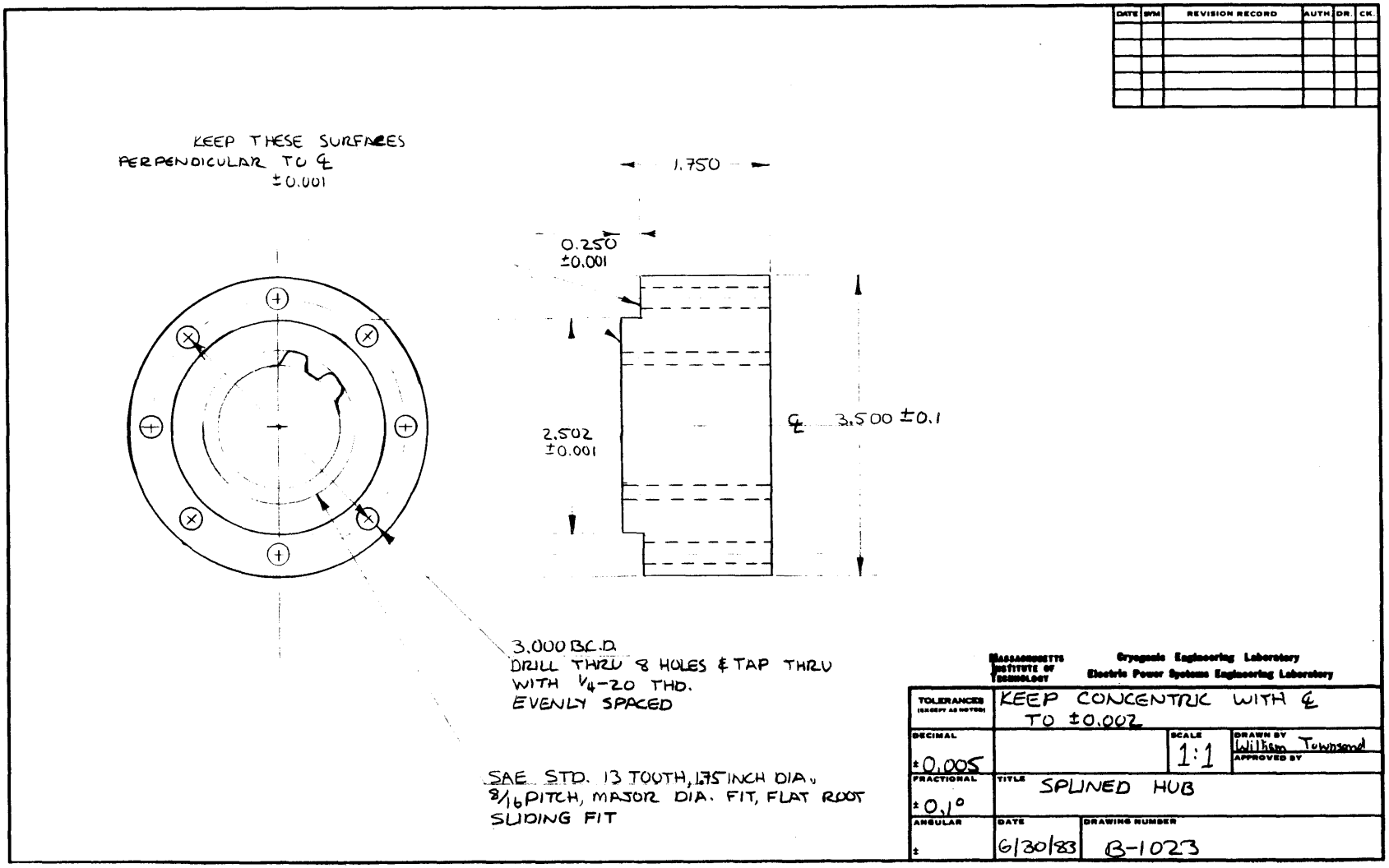

FIGURE A.4 DRAWING OF INTERNALLY SPLINED HUB

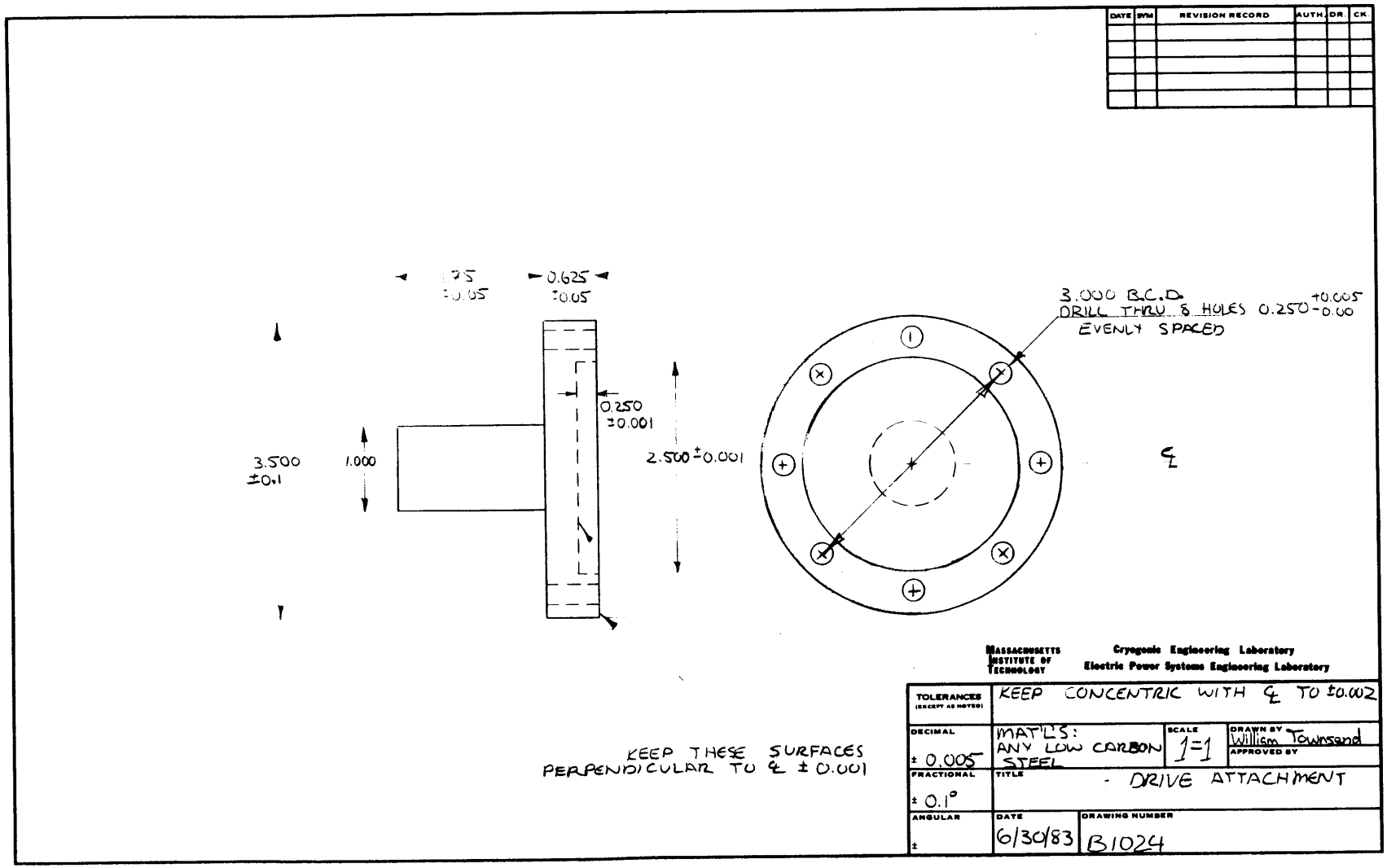

FIGURE A.5 DRAWING OF MATING PIECE FOR THE INTERNALLY SPLINED HUB

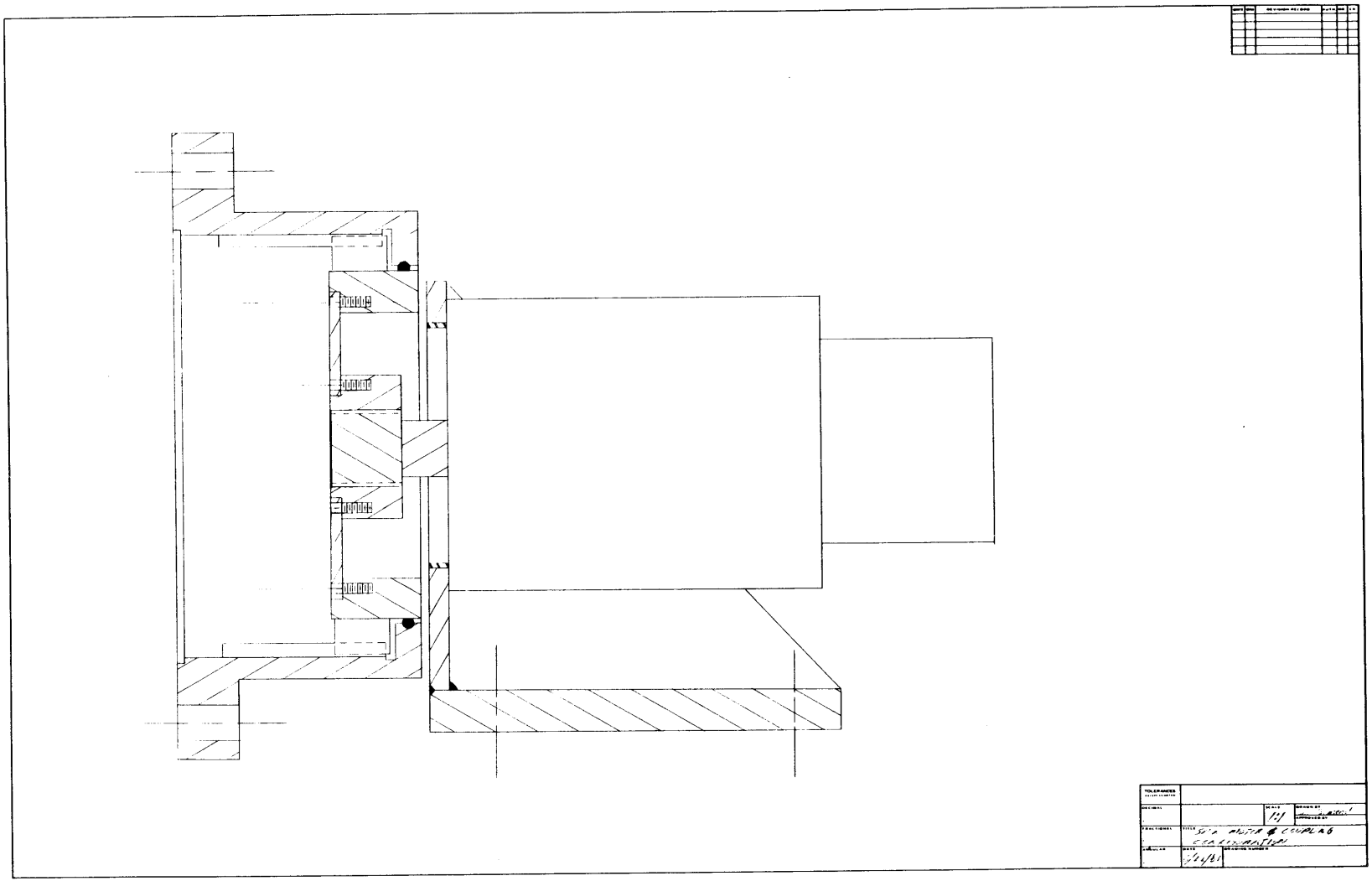

FIGURE A.6 SPIN MOTOR ARRANGEMENT FOR POST-BALANCING SPIN TESTS

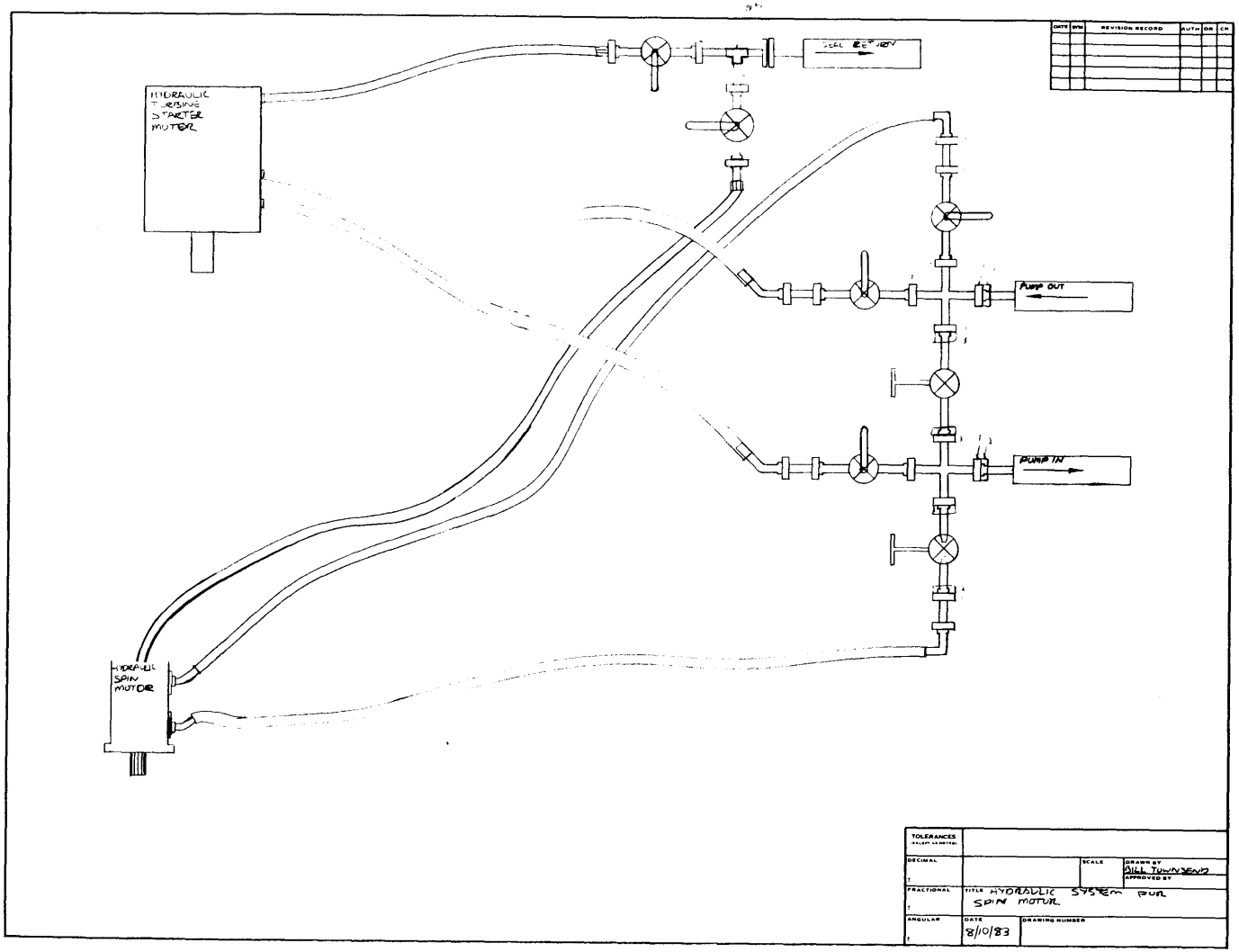

FIGURE A.7 SCHEMATICS OF SPIN MOTOR HYDRAULIC SUPPLY

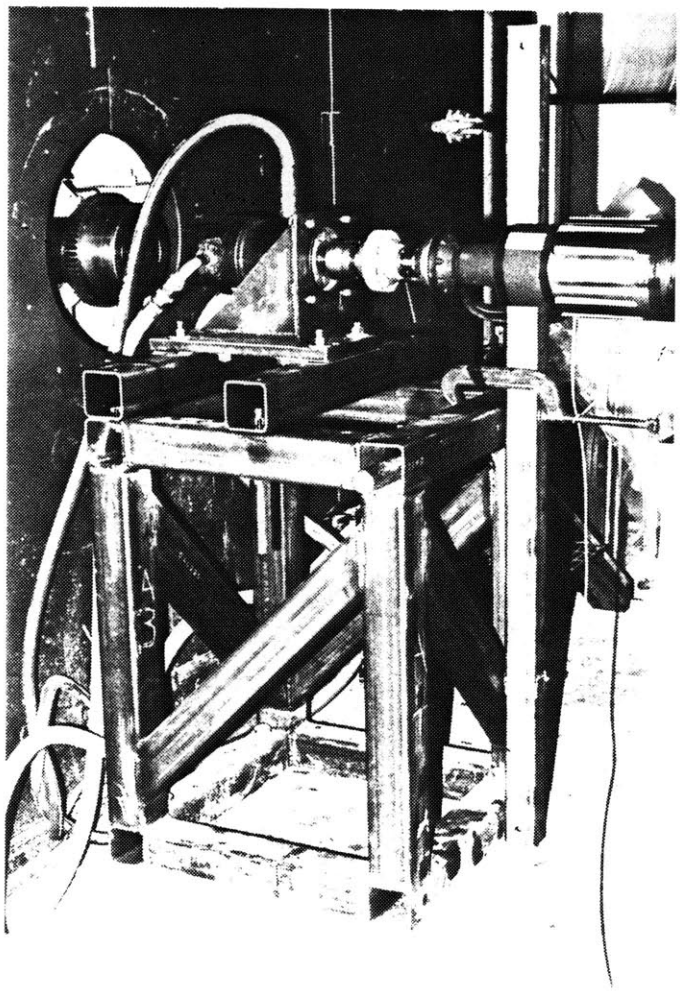

FIGURE A.8 SPIN MOTOR STAND

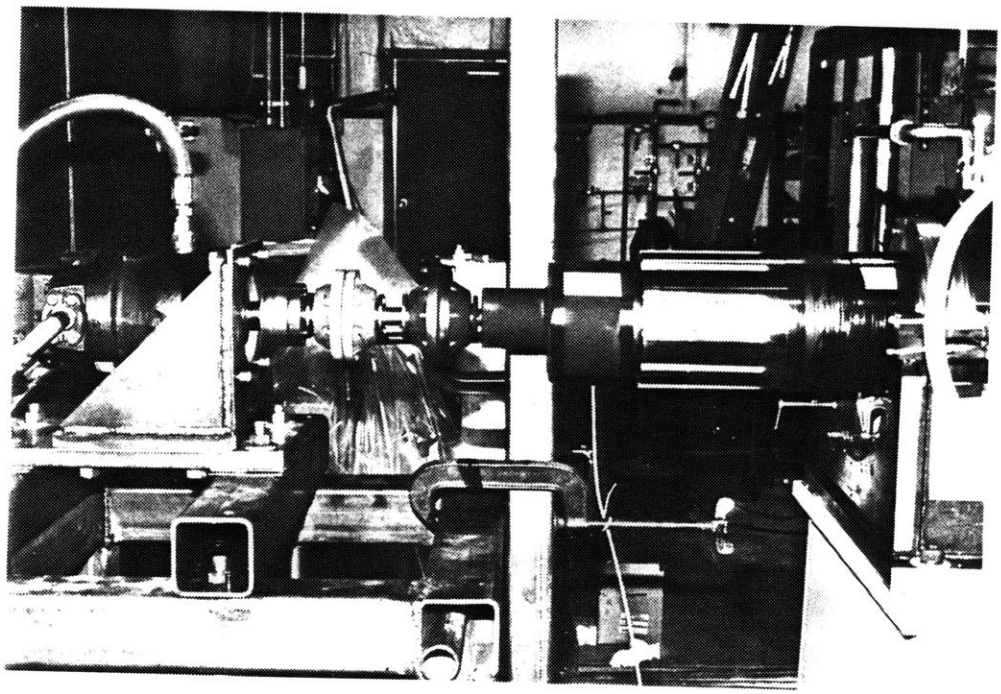

FIGURE A.9 INSTALLED DRIVE COUPLING

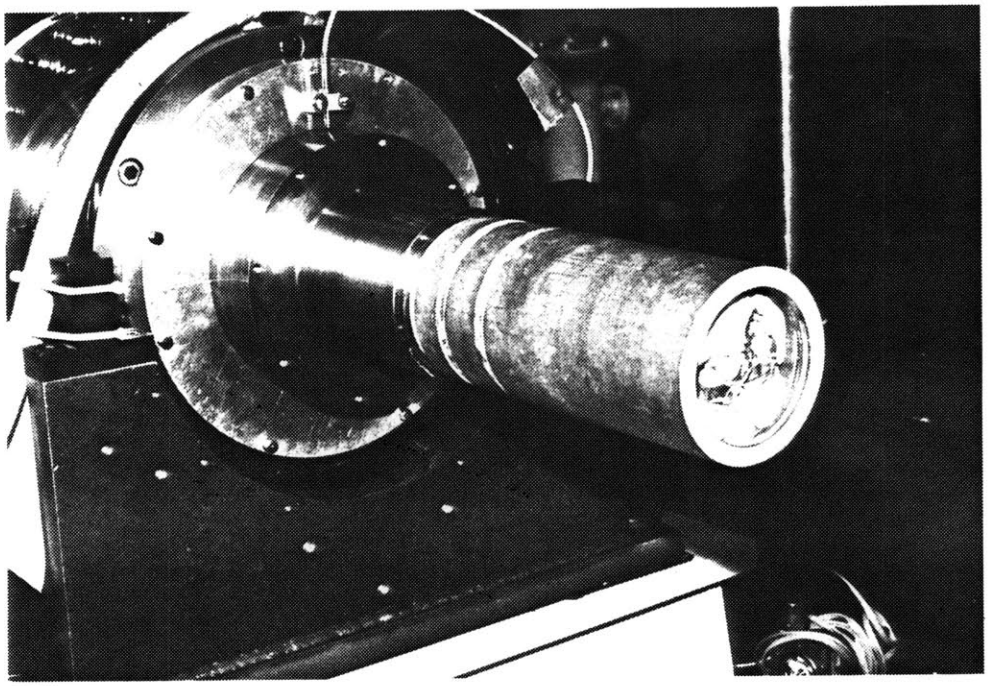

FIGURE A.10 TEMPORARY SUPPORT FOR THE FIELD LEADS

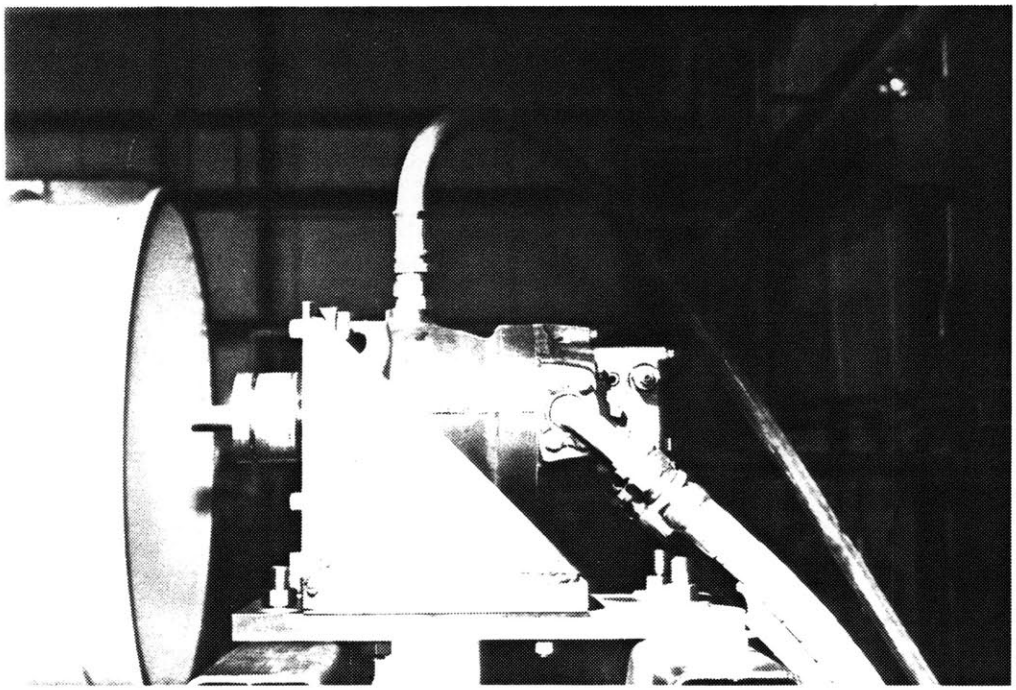

FIGURE A.11 SPIN MOTOR AND FOOT

CALCULATION OF THE LATERAL FORCE TRANSMITTED BY THE DRIVE COUPLING

The drive coupling can transmit lateral forces to the rotor and cause apparent unbalance. We made efforts to minimize these forces by designing the drive coupling to be very compliant laterally. In the following, we calculate the force and moment, fixed in the stationary plane, which would be transmitted to the rotor if the rotor axis of rotation were misaligned by, Δ , equal to 10 mils from the spin motor output shaft axis of rotation.

There are two rubber coupling halves (see figure IV.2.1). The coupling sets are assumed to have infinite stiffness in shear. The angular stiffness was measured to be 1200 in-lbs/rad. The distance between coupling center-planes, l, is 5.5 inches. A rotating moment will therefore be

$$m = k\theta \cong k \frac{\Delta}{\ell} = \frac{1200\ \Delta}{5.5} = 220\ \Delta \text{ in-lbs} \qquad (A.1)$$

The rotating force will be

$$F = k \frac{\Delta}{\ell^2} = 40\Delta \text{ lbs} \qquad (A.2)$$

So for a 10 mil deflection,

M = 2.2 in-lbs, and

F = 0.40 lbs.

APPENDIX B

CIRCUIT DIAGRAMS AND LAYOUTS

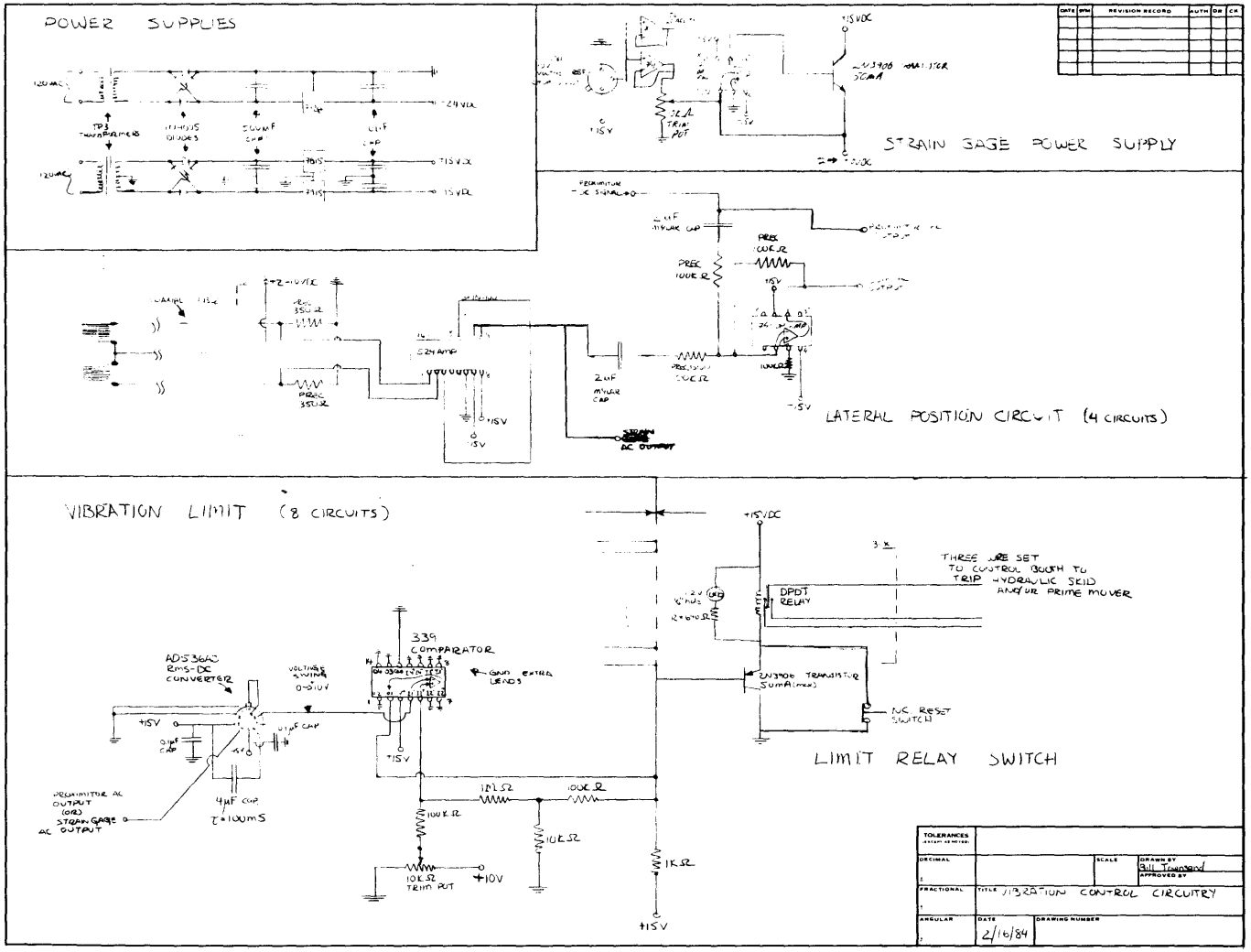

FIGURE B.1 INDIVIDUAL SIGNAL CIRCUITS AND POWER SUPPLIES

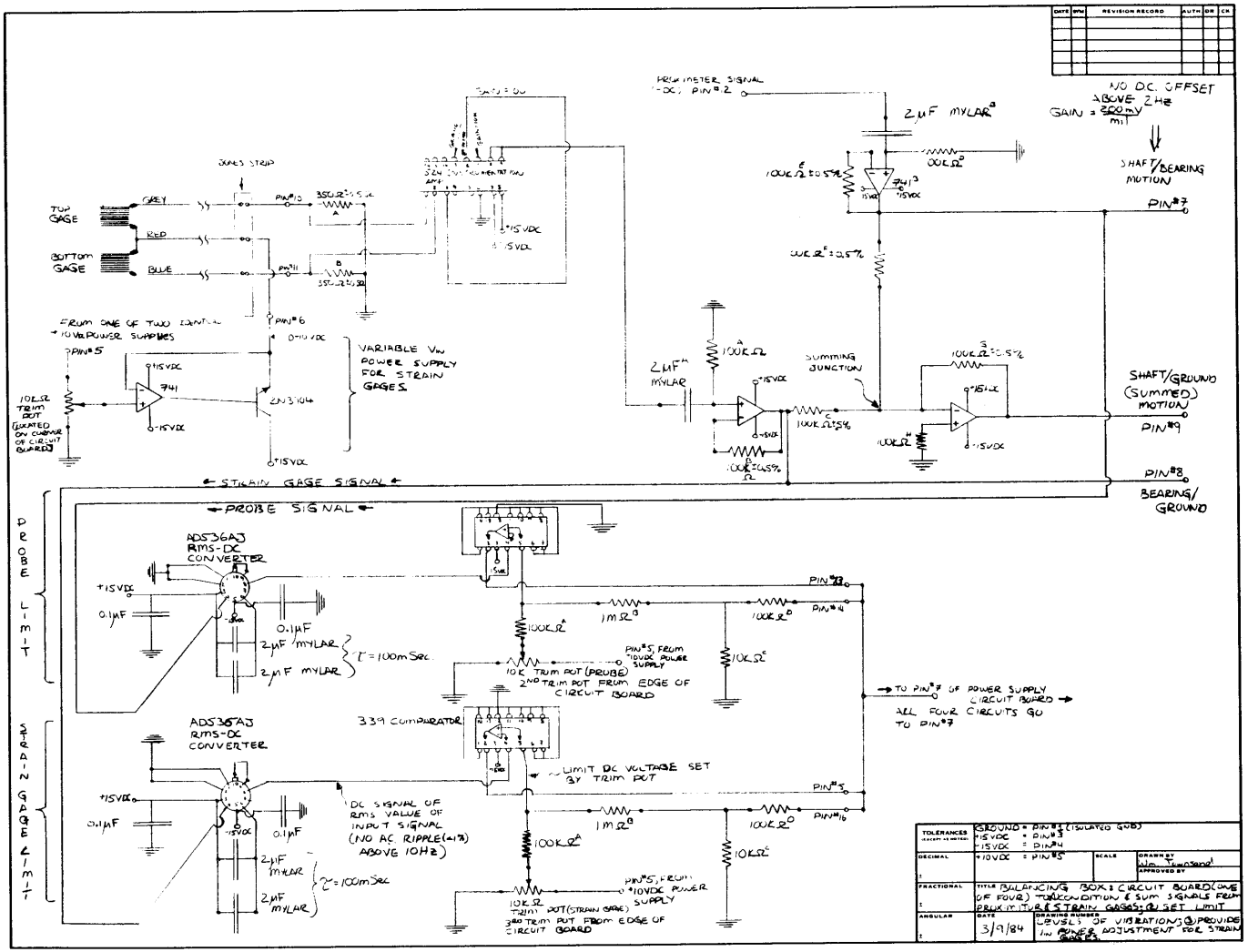

FIGURE B.2 SIGNAL CIRCUITS AS ARRANGED ON THE CIRCUIT BOARDS

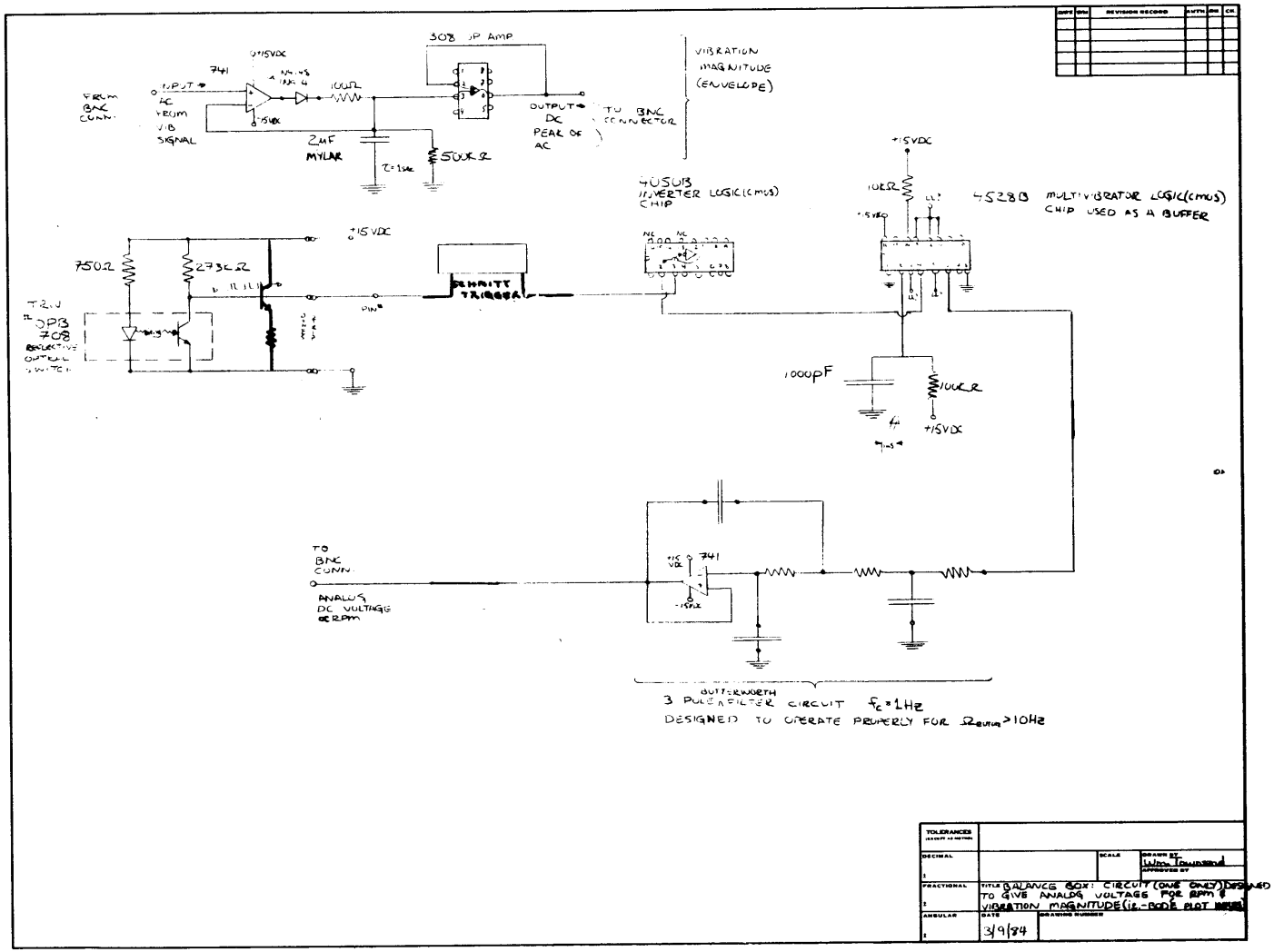

FIGURE B.3 ROTOR ROTATION AND ANALOG CIRCUITS

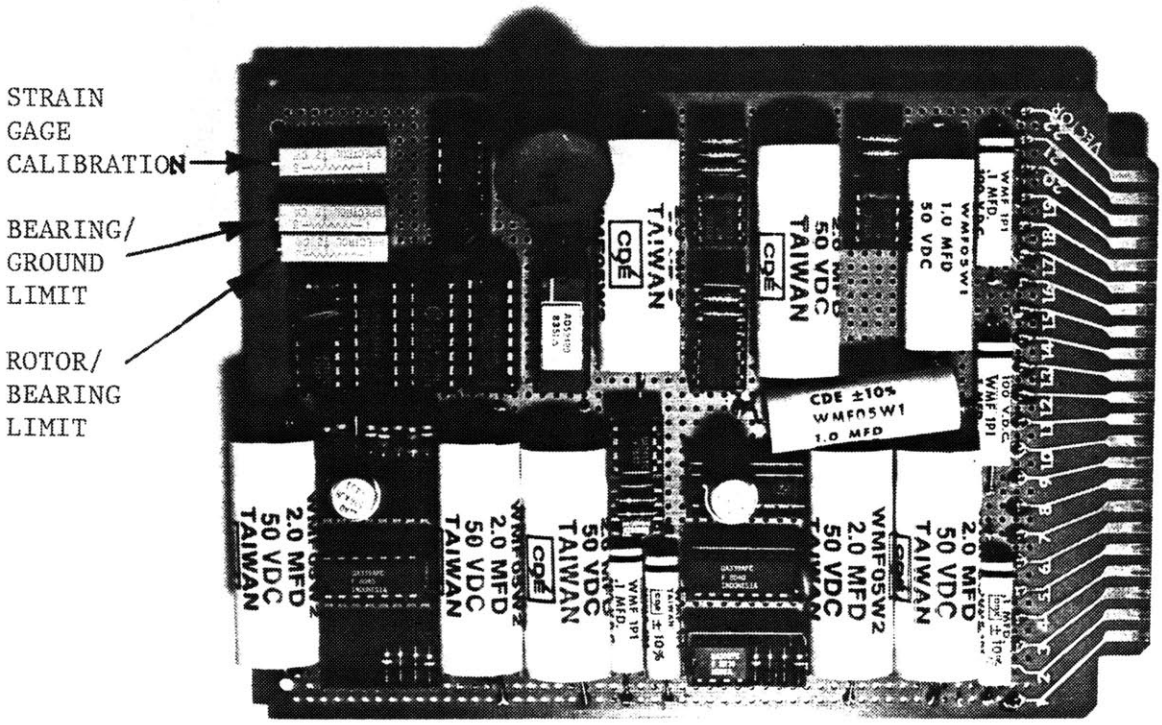

FIGURE B.4 LATERAL VIBRATION CIRCUIT BOARD

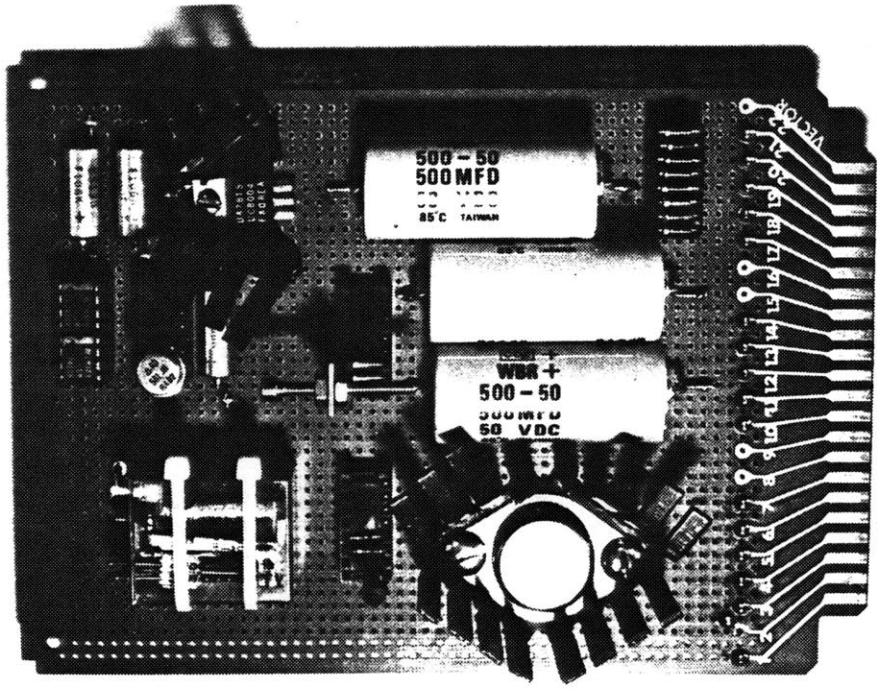

FIGURE B.5 CIRCUIT BOARD WITH LIMIT RELAY, VOLTAGE REGULATORS, AND MAGNITUDE-VERSUS-SPEED CIRCUIT

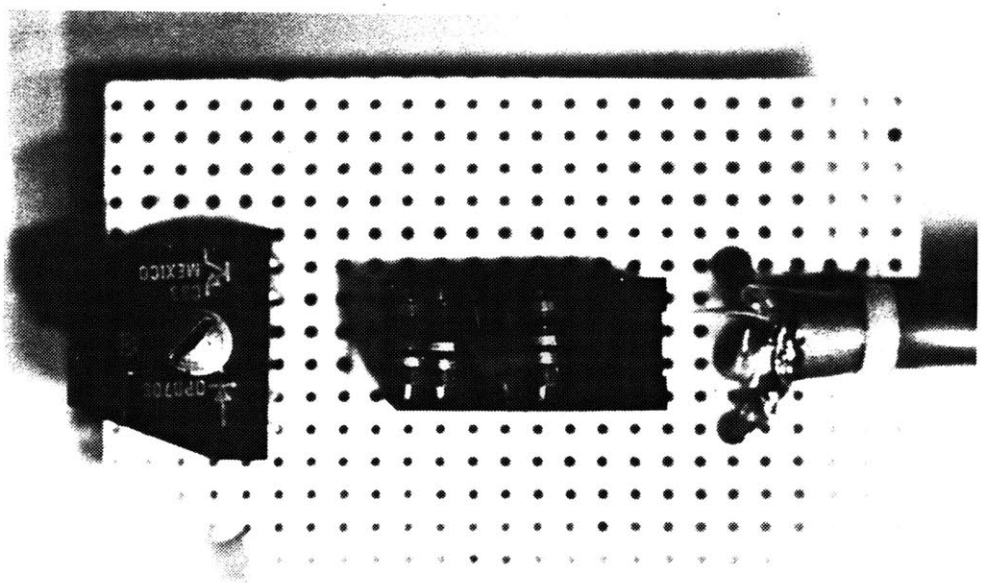

FIGURE B.6 PHOTO DETECTOR

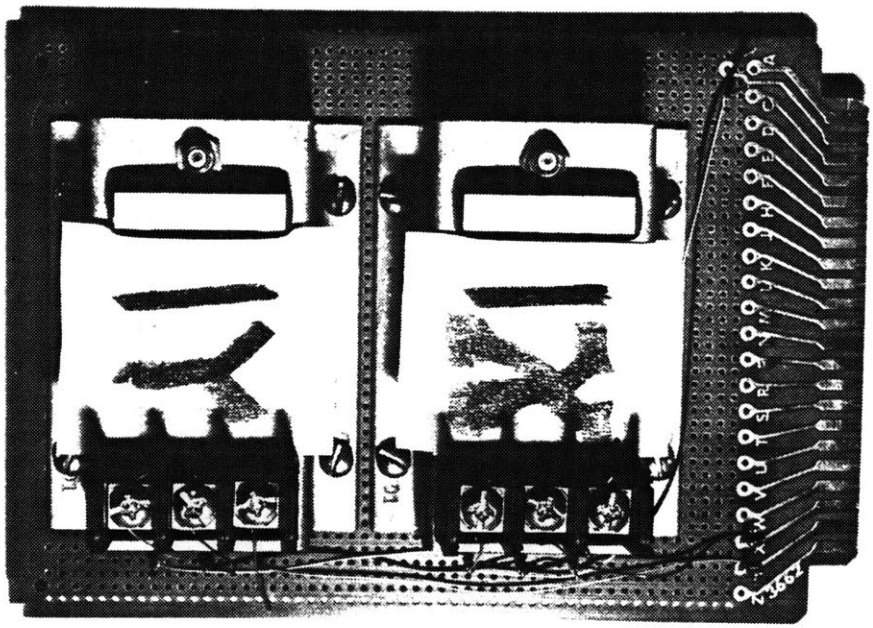

FIGURE B.7 CIRCUIT-BOARD-MOUNTED PROXIMITORS

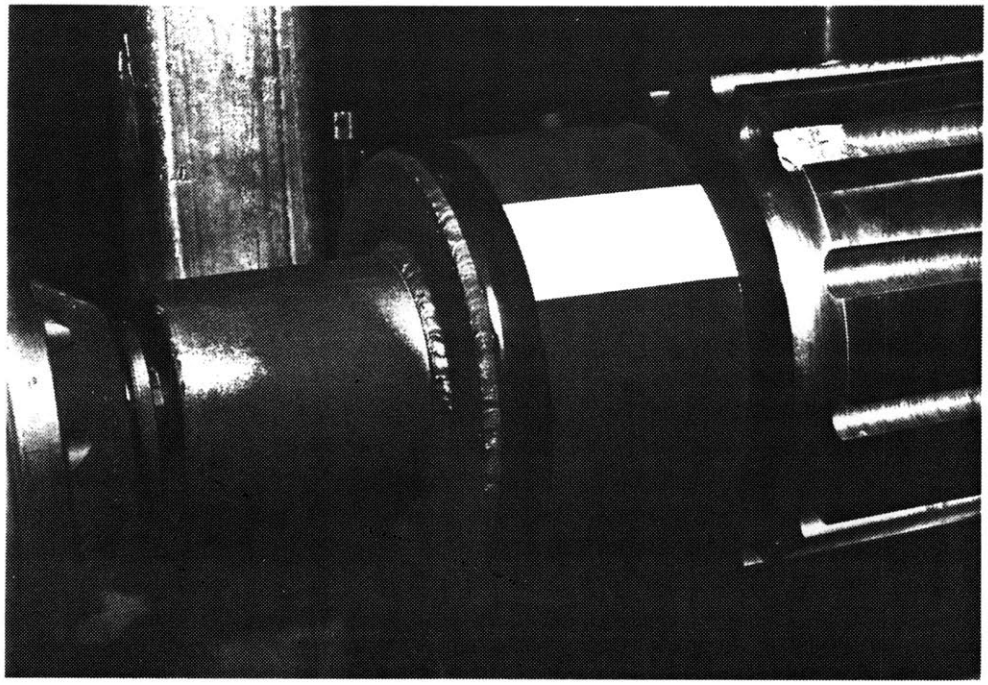

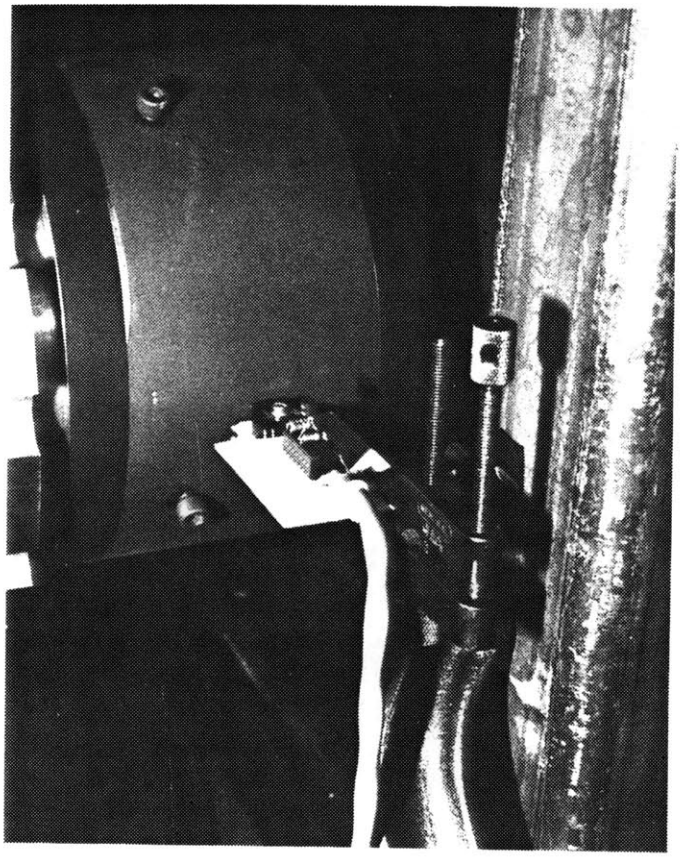

FIGURE B.8 MOUNTED PHOTO DETECTOR

APPENDIX C

JCF FORTRAN PROGRAM LISTINGS

```
      program main
C
C             PROGRAM TO READ DATA FROM NICOLET DIGITAL
C             OSCILLOSCOPE INTO VAX COMPUTER
C
      dimension pvolt(0:2047), vvolt(0:2047)
      dimension plt(2,2048)
      CHARACTER*10 FNAME
      CHARACTER*6 DIGITS
      CHARACTER*4 TYPE
      CHARACTER*3 CODE
      COMMON/FILE/ FNAME
      COMMON/CODE/ X,CODE
      WRITE (6,*) 'IS "SET TERM/NOECHO" ?'
10    WRITE (6,*) 'RECALL DATA FROM DISC TO SCOPE MEMORY'
      PAUSE 'TYPE "CONTINUE" WHEN READY'
      CALL RECEIVE
      call convert (pvolt, vvolt)
C       STORE THE VIBRATION DATA, NOW IN DECIMAL F-FORMAT, IN A FILE CALLEI
C       'BALNIC1.DAT'.  THE INCREMENTING VERSIONS WILL KEEP THE FILES
C       IDENTIFIED
      open (unit=1, status='new', file='balnic1.dat')
      write (1,39) (pvolt(i), vvolt(i), i=1,2048)
 39   format (10x,f15.10,10x,f15.10)
      close (unit=1, status='keep')
      stop
      end
```

```
      SUBROUTINE RECEIVE
C
C               SUBROUTINE TO RECEIVE NORMALIZATION INFO IN ASCII AND
C               DATA FOR ONE CURVE IN PRINTABLE BINARY FROM NICOLET
C
      character*2 string(0:4095), term
      COMMON/REC/ IPN4,PN6,IVN4,VN6
      COMMON/STRING/ STRING
      COMMON/TIME/ VN7
C               RECEIVE TWO NORMALIZATION SETS, ONE FOR EACH CHANNEL
      WRITE (6,*) 'RECEIVING NORMALIZATION'
      WRITE (6,*) CHAR(1)
      WRITE (6,*) 'E1N2'
      WRITE (6,*) '00002'
      WRITE (6,*) CHAR(2)
      READ (5,100) IVN1,IVN2,IVN3,IVN4,IVN5,VN6,VN7
100   FORMAT (3I1,2I5,2E7.1)
      READ (5,100) IPN1,IPN2,IPN3,IPN4,IPN5,PN6,PN7
      READ (5,101) TERM
101   FORMAT (A2)
C               RECEIVE 2048 TWO CHARACTER PRINTABLE BINARY WORDS
C               IN 64 GROUPS OF 32
C               IN ORDER NOT TO EXCEED 78 CHARACTER VAX INPUT BUFFER
      WRITE (6,*) 'START RECEIVING DATA'
      I = 0
C               LOAD STARTING ADDRESS
      WRITE (6,*) CHAR(1)
      WRITE (6,*) 'E3D1'
      WRITE (6,*) 'I0001'
      WRITE (6,*) CHAR(2)
      WRITE (6,102) I
102   FORMAT (I4)
      WRITE (6,*) CHAR(3)
      READ (5,101) TERM
      DO 80 I=0,4064,32
C               RECEIVE 32 WORDS
      WRITE (6,*) CHAR(1)
      WRITE (6,*) 'E3D2'
      WRITE (6,*) '00032'
      WRITE (6,*) CHAR(2)
      READ (5,103) (STRING(J),J=I,I+31)
103   FORMAT (32A2)
      READ (5,101) TERM
80    CONTINUE
      WRITE (6,*) 'END RECEIVING DATA'
      RETURN
      END
```

```
      subroutine convert (pvolt,vvolt)
C
C               SUBROUTINE TO TAKE PRINTABLE BINARY P-V VOLTAGE DATA,
C               TRANSLATE IT TO INTEGER,
C               AND NORMALIZE IT TO FLOATING POINT
C
      DIMENSION PVOLT(0:2047),VVOLT(0:2047)
      CHARACTER*2 STRING(0:4095)
      COMMON/REC/ IPN4,PN6,IVN4,VN6
      COMMON/STRING/ STRING
C               TRANSLATE PRINTABLE BINARY TO INTEGER
      WRITE (6,*) 'TRANSLATING TO INTEGER AND NORMALIZING'
      J = 0
      M = 0
      N = 0
      DO 90 I=0,4095
      IHIGH = ICHAR(STRING(I)(1:1)) - 32
      ILOW = ICHAR(STRING(I)(2:2)) - 32
      INT = 64*IHIGH + ILOW
C               NICOLET DATA WITH RANGE -2048 TO +2047 IS TWO'S
C               COMPLIMENT BINARY.  THUS IF NUMBER IS GREATER THAN
C               2047, IT IS ACTUALLY NEGATIVE AND 4096 MUST BE
C               SUBTRACTED FROM IT TO FIND ACTUAL NUMBER.
      IF (INT.GT.2047) INT=INT-4096
C               NORMALIZE INTEGERS TO FLOATING POINT
      IF (J.GE.1) GO TO 60
      J = 1
      VVOLT(M) = VN6*(INT-IVN4)
      M = M + 1
      GO TO 90
60    J = 0
      PVOLT(N) = PN6*(INT-IPN4)
      N = N + 1
90    CONTINUE
      RETURN
      END
```

```
      program bplotx
      character*15 filename
      dimension plt(2,2048)
      PRINT*, 'TYPE THE DATA FILENAME TO BE PLOTTED'
C      READ DATA WHICH WAS FED TO THE JCF BY THE NICOLET OSICILLOSCOPE
      READ *, FILENAME
      OPEN (UNIT=1, STATUS='OLD', FILE=FILENAME)
      READ (1,38) ((PLT(I,J), I=1,2), J=1,2048)
 38   FORMAT (2(10X,F15.10))
      CLOSE (UNIT=1)
C       DELTA IS THE SENSITIVITY FOR IDENTIFYING THE CYCLE PULSE.  IT DETEC
C       A VOLTAGE RISE OF DELTA = VOLTAGE / 20.0 WITHIN TWO DATA POINTS.
       delta =0.02
C       SCALE THE VIBRATION DATA TO MILS OF ROTOR DEFLECTION
C       AND SCALE THE PULSE CURVE TO A SMALL VALUE.
      DO 90 J=1, 2048
      PLT(2,J) = PLT(2,J)/0.200
      PLT(1,J) = PLT(1,J)/20.0
 90   CONTINUE
C       LOCATE LEADING EDGE OF FIRST CYCLE PULSE
      X = 0.0
      N = 4
      DO 91 J=1,2000
      N = N+1
      X = PLT(1,J+5) - PLT(1,J+3)
      IF (X-DELTA) 91,91,92
 91   CONTINUE
C       REDEFINE THE NUMBER OF DATA POINTS.  THE FIRST DATA POINT IS TO
C       CORRESPOND TO THE LEADING EDGE OF THE FIRST CYCLE PULSE.
 92   NPTS = 2048-N
      M = 0
      DO 93 J=1,NPTS
      M = J+N
      PLT(1,J) = PLT(1,M)
      PLT(2,J) = PLT(2,M)
 93   CONTINUE
C       FIND THE NUMBER OF POINTS PER CYCLE
      X = 0.0
      N = 100
      DO 94 J=101,NPTS
      N = N+1
      X = PLT(1,J) - PLT(1,J-2)
      IF (X-DELTA)  94,94,95
 94   CONTINUE
 95   XN = N
      XNPTS = NPTS
C       THE NUMBER OF CYCLES ON THE PLOT WILL NOW BE :
      FTIME = XNPTS/XN
C      CREATE A HDCOPY.PLT FILE
      CALL PICTR (PLT,2,
     1 'NUMBER OF ROTOR CYCLES.  AT 0.0, PHI=0.0
     1      ROTOR DEFLECTION IN MILS          ',
     1 XSCL,2,NPTS,0,00,0014,1,FTIME,LOOK)
      STOP
      END
```

APPENDIX D

MISCELLANEOUS CALCULATIONS

APPENDIX D.1 CALCULATION OF HELIUM TUBE STABILITY

A given helium tube may become unstable if the rotor reaches the helium tube critical speed. The worst case is considered to be the tubes which carry the copper field leads.

The deflection, δ , of these tubes was previously calculated [10] to be

$$\delta = \frac{5qL^4}{384EI} \qquad (D.1.1)$$

where,

$q = m \cdot e =$ (mass of the tubes and field leads per inch)× (distance to the bearing/bearing center line)

$= 13.25\ lb_f/in$

$L =$ unsupported length $= 8$ inches

$E =$ elastic modulus of steel $= 30 \times 10^6$ psi

$I =$ moment of inertia $= 0.005\ in^4$

The stiffness is

$$k = \frac{F}{\delta} = \frac{m \cdot e \cdot \Omega^2}{\delta} \qquad (D.1.2)$$

The critical speed is

$$\omega_n = \sqrt{k/m} = \sqrt{\frac{\frac{m \cdot e \cdot \Omega^2}{\delta}}{m}} = \sqrt{e/\delta}\ \Omega \qquad (D.1.3)$$

If we combine (D.1.1) and (D.1.3), then

$$\omega_n = \sqrt{\frac{384EIe}{5q\ L^4}}\ \Omega = 50{,}000\ \text{RPM} \quad .$$

APPENDIX D.2 FLUID CAUSED INSTABILITY

In general the effect of partially filling a rotor with liquid is to: 1) decrease the critical speed, and 2) to create a zone of instability at supercritical speed.

For the 10 MVA rotor the reduction in critical speed is negligible (0.12 percent) because the mass of helium liquid is so low compared to the rotor mass. Whether an instability will occur cannot be determined because the system damping has not been quantified. However, a range of rotor speed within which an instability might occur can be quantified as

$$3170 < \Omega < 3190 \text{ RPM} .$$

We used Wolf's notation [47] and the model of figure D.2.1 in the analysis.

m_L = 7.5 lbm = mass of liquid needed to fill the rotor

m_R = 3243 lbm = mass of rotor (without flywheel, which is the worst case)

$\mu = m_L/m_R = 0.00231$

$F = \omega/\omega_0$ = dimensionless whirl frequency

$S = \Omega/\omega_0$ = dimensionless rotor speed

ω_0 = 1980 = ADINA estimation of the first critical speed

Wolf developed a characteristic equation for a rotor partially filled with a fluid.

$$(\gamma+\mu)F^4 + 2\alpha SF^3 + (\alpha S^2-\gamma) + 2(\gamma+1)SF - (\gamma+1)S^2 = 0 \quad , \quad (D.2.1)$$

where

$$\gamma = \frac{\left[\left(\frac{a}{b}\right)^2 + 1\right]}{\left[\left(\frac{a}{b}\right)^2 - 1\right]} = 1.52 \qquad (D.2.2)$$

and,

$$\alpha = (\gamma + 2\mu + 1) = 2.525 \quad . \qquad (D.2.3)$$

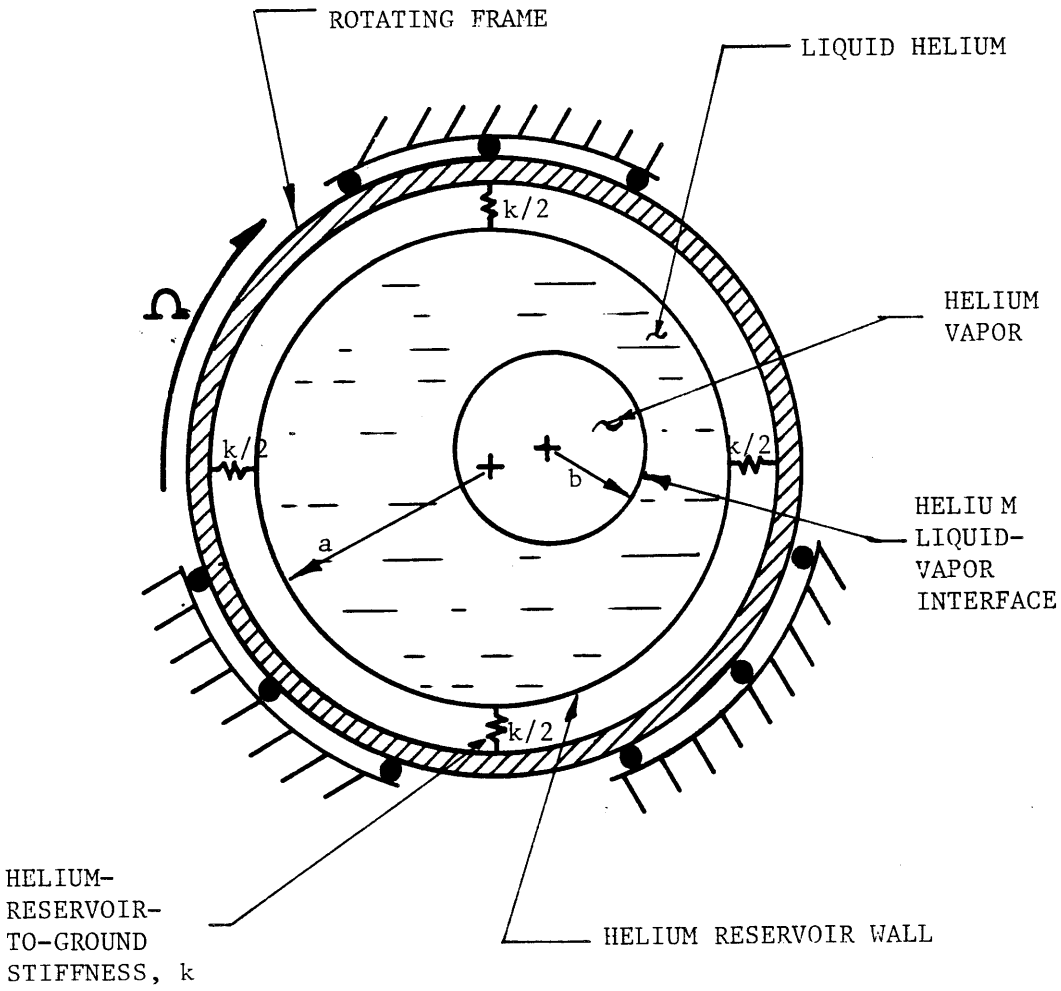

FIGURE D.2.1 MODEL OF LIQUID HELIUM IN THE RESERVOIRS

We put D.2.1 into standard quadratic form.

$$[\alpha F^2 - \gamma - 1]S^2 + [-2\alpha F^3 + 2(\gamma+1)F]S + [(\gamma+\mu)F^4 - \gamma F^2] = 0 \quad \text{(D.2.4)}$$

We solved for S numerically given different values of F ($0 < F > 4$) and plotted only the real roots of D.2.4 (see figure D.2.1). When the roots of D.2.4 are imaginary, the system has positive exponential terms and a zone of instability exists. In figure D.2.2 the zone of instability is shown graphically.

APPENDIX D.3 Estimation of Assembly Induced Unbalance

If at the end planes we reassemble the low-speed-balanced rotor as shown in figure III.5.1, then due to assembly tolerances an estimation of the induced unbalance follows. For small Δ ,

$$e = \ell_B \frac{\Delta}{D} \quad . \qquad \text{(D.3.1)}$$

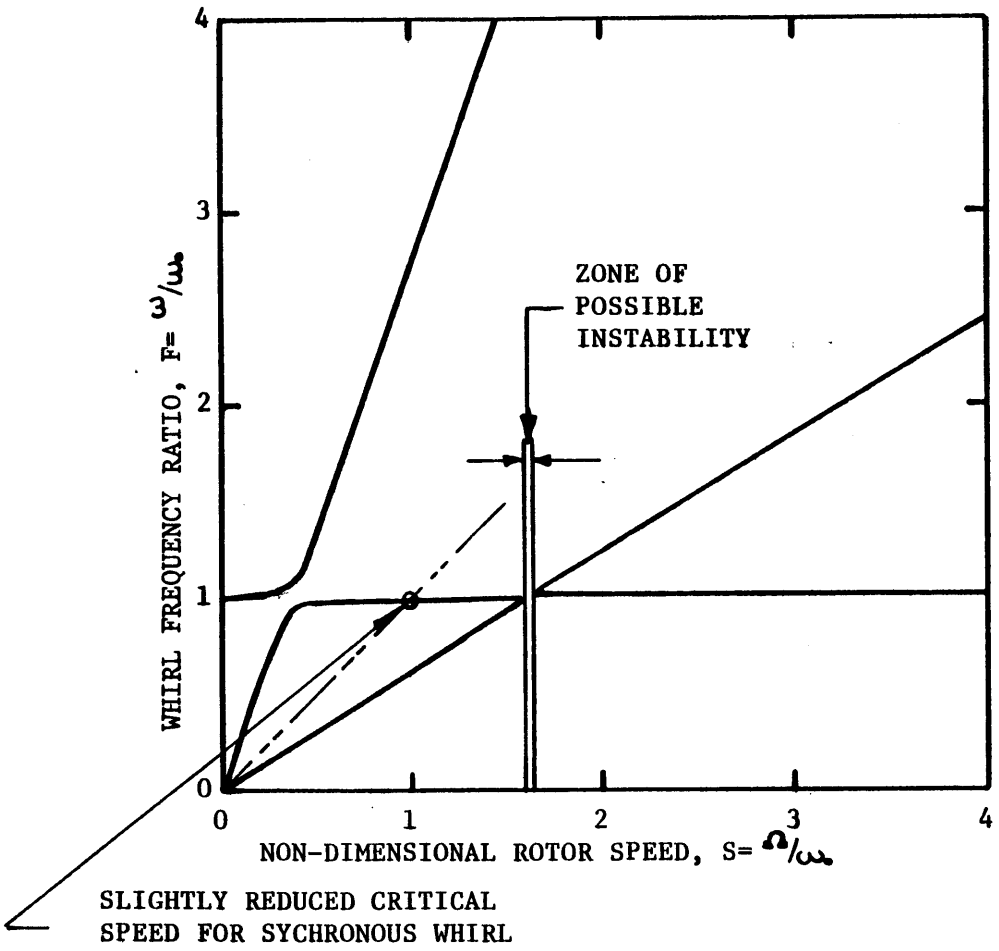

FIGURE D.2.2 FLUID WHIRL INSTABILITY

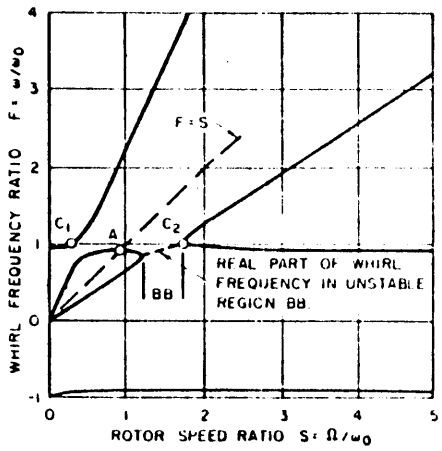

Fig. 4 Whirl diagram for test rotor with $\mu = 0.206$ and $\gamma = 2.6$

EXAMPLE FROM WOLF'S PAPER [47] FOR A LIQUID, USED IN AN EXPERIMENT, WHICH DEVELOPED AN INSTABILITY.

The unbalance, U, (if we assume no compliance in the rotor system) would be

$$U = m_{ACT} e \quad . \tag{D.3.2}$$

where,

m_{ACT} = 2000 lbm = mass of the active section and reservoir.

So,

$$U = m_{ACT} \ell_B \frac{\Delta}{D} = 1250\ \Delta \tag{D.3.3}$$

Therefore, if Δ is 0.002 inches which is feasible) then the unbalance would be 2.5 inch-pounds (see figure D.3.1).

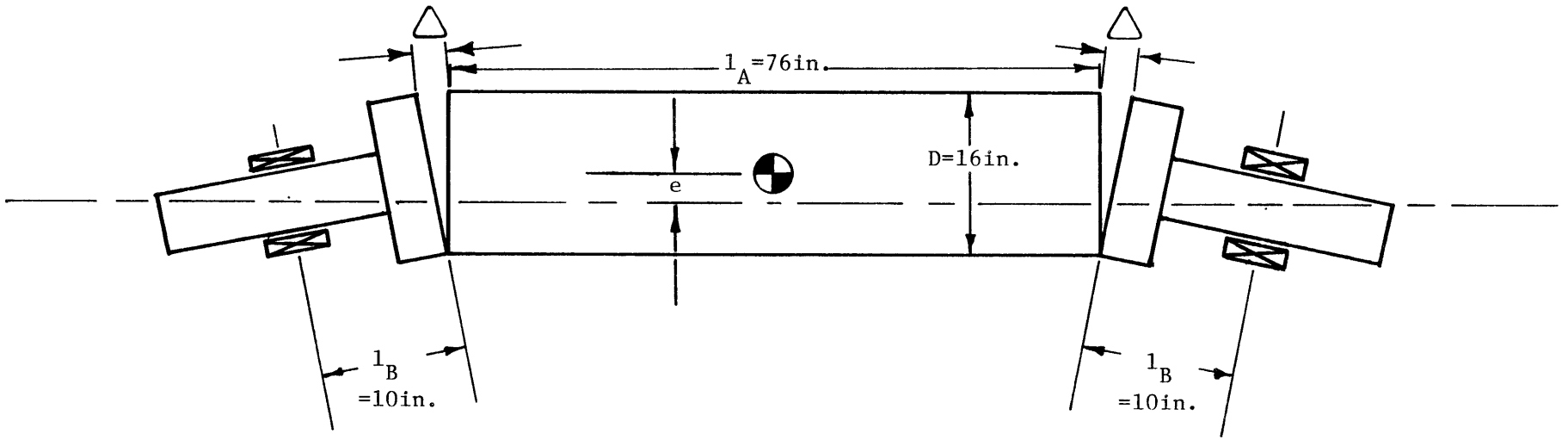

FIGURE D.3.1 UNBALANCE CAUSED BY MISALIGNED ROTOR ASSEMBLY

BIBLIOGRAPHY

1. Badgley, R. H. "Recent Developments in Multiplane-Multispeed Balancing of Flexible Rotors in the United States," in Dynamics of Rotors, edited by F. I. Niordson (IUTAM Symposium, Lyngby, Denmark, August 12-16, 1974; Berlin: Springer, 1975), pp. 1-26.

2. Barrett, L. E., Gunter, J. E., and Allaire, P. E. "Optimum Bearing and Support Damping for Unbalance Response and Stability of Rotating Machinery," ASME paper, No. 77-GT-27, Gas Turbine Conference, Philadelphia, PA, Dec. 15, 1976. Reprinted in "Rotor Dynamics & Rotor-Bearing Course Notes," edited by E. J. Gunter (Charlottesville, VA: Rotor Dyunamics Laboratory, Department of Mechanical and Aerospace Engineering, Univ. of Virginia, [1982]), sect. 2:3.

3. Bishop, R. E. D., and Gladwell, G. M. L. "The Vibration and Balancing of an Unbalanced Flexible Rotor," J. Mech. Engng. Sci., 1, no. 1(1959).

4. Bishop, R. E. D., and Parkinson, A. G. "On the Use of Balancing Machines for Flexible Rotors," Trans. ASME, J. Engng. Industry, 94(B2)(1972).

5. Idem. "On the Isolation of Modes in the Balancing of Flexible Shafts," Proc. Inst. Engrs., 177(London, 1963).

6. Broch, J. T. The Application of the Bruel and Kjaer Measuring Systems to Mechanical Vibration and Shock Measurements. Revised edition. Soborg, Denmark: K. Larsen & Son, 1976.

7. Bucciarelli, L. L. "On the Instability of Rotating Shafts Due to Internal Damping," Trans. ASME, J. Appl. Mechs., 49(1982), pp. 425-428.

8. Bucciarelli, L. L., and A. Rangarajan Dynamic Analysis of a Magnetically Suspended Energy Storage Wheel. U.S. Dept. of Energy, DOE/ET/20279-102(1980).

9. Capriz, G. "Self-Excited Vibrations of Rotors," in Dynamics of Rotors, op. cit., pp. 128-141.

10. Chafe, J. N. "Helium Flow System for A 10 MVA Superconducting Generator." Master's thesis, MIT, June, 1984.

11. Choy, K. C., Gunter, E. J., and Allaire, P. E. "Fast Fourier Transform Analysis of Rotor-Bearing Systems." Reprinted in "Rotor Dynamics & Rotor-Bearing Course Notes," op. cit., sect. 4:5

12. Crandall, S. H. "The Physical Nature of Rotor Instability Mechanisms." Unpublished paper distributed privately, n.d.

13. Crandall, S. H., Karnopp, D. C., Kurtz, E. F., and Pridmore-Brown, D. C. Dynamics of Mechanical and Electromechanical Systems. New York: McGraw-Hill, 1968.

14. Den Hartog, J. P. "The Balancing of flexible Rotors," Air and Space Instruments. Edited by S. Lees. (Draper Anniversary Volume) New York: McGraw-Hill, 1963.

15. Idem. Mechanical Vibrations. 4th edition. New York: McGraw-Hill, 1956.

16. Flack, R. D., Leader, M. E., and Gunter, E. J. "An Experimental Investigation on the Response of a Flexible Rotor Mounted in Pressure Dam Bearings," Trans. ASME, J. of Mech. Design, 102(Oct., 1980).

17. Gunter, E. J. "Rotor-Bearing Stability," Proceedings of the First Turbomachinery Symposium, reprinted in "Rotor Dynamics & Rotor-Bearing Course Notes," op. cit., sect. 2:1.

18. Gunter, E. J., Barrett, L. E., and Allaire, P. E. "Design and Applications of Squeeze Film Dampers for Turbomachinery Stabilization," Proceedings of the Fourth Turbomachinery Symposium. Reprinted in "Rotor Dynamics & Rotor-Bearing Course Notes," op. cit., sect. 2:5.

19. Hamblen, D. G. "Hunting Oscillations in Superconducting Alternators," IEEE PES, C 75 145-8(Winter, 1974).

20. Holman, J. P., and Gajda, J. P. Experimental Methods for Engineers. 3rd edition. New York: McGraw-Hill, 1978.

21. Holmes, R. "Vibration and Its Control in Rotating Systems," in Dynamics of Rotors," op. cit., pp. 156-181

22. Kellenberger, W. "Limits to Modal Balancing of Flexible Rotors," in Dynamics of Rotors, op. cit., pp. 206-243.

23. Idem. "Should a Flexible Rotor be Balanced in N or (N+2) Planes?", Trans. ASME, J. Engng. Industry, 94(B2)(1972).

24. Kirk, R. G., de Choudhury, P., and Gunter, E. J. "The Effect of Support Flexibility on the Stability of Rotors Mounted in Plain Cylindrical Journal Bearings," in Dynamics of Rotors, op. cit., pp. 244-298. Reprinted in "Rotor Dynamics & Rotor-Bearing Course Notes," op. cit., sect.

25. Loewy, R. G., and Piarulli, V. J. Dynamics of Rotating Shafts. Washington, D. C.: The Shock and Vibration Information Center, United States Department of Defense, 1969.

26. Lord, S. M. "Analysis of Lateral Viberation Modes of a Superconducting Generator." Master's thesis, MIT, Sept., 1979.

27. Lund, J. W. "Response Characteristics of a Rotor with Flexible, Dample Supports," in Dynamics of Rotors, op. cit., pp. 319-349.

28. Lund, J. W., and Tonneson, J. "Analysis and Experiments on Multiplane Balancing of a Flexible Rotor," ASME paper 71-VIBR-74, Vibration Conference, Toronto, Canada, 1971.

29. Marks' Standard Handbook for Mechanical Engineers. Edited by T. Baumeister, E. A. Avallone, and T. Baumeister III. 8th edition. New York: McGraw-Hill, 1978.

30. Muszynska, A. "Nonlinear Excited and Self-Excited Precessional Vibrations of Symmetrical Rotors," in Dynamics of Rotors, op. cit., pp. 380-412.

31. Nicholas, J. C., Gunter, E. J., and Allaire, P. E. "Stiffness and Damping Coefficients for the Five-Pad Tilting-Pad Bearing," ASLE preprint, no. 77-LC-3A-2, ASLE/ASME Lubrication Conference, Kansis City, MO, Oct. 3-5, 1977. Reprinted in "Rotor Dynamics & Rotor-Bearing Course Notes," op. cit., sect. 1:4.

32. Nicholas, J. C., Gunter, E. J., and Barrett, L. E. "The Influence of Tilting Pad Bearing Characteristics on the Stability of High Speed Rotor-Bearing Systems." Reprinted in "Rotor Dynamics & Rotor-Bearing Course Notes," op. cit., sect. 2:4.

33. Ogata, K. Modern Control Engineering. Englewood Cliffs, N.J.: Prentice-Hall, 1970.

34. "Operating and Maintenance Manual, 7200 Series: Nontouching, Eddy Current Proximity Transducer." Revised edition. (7200 P/P, 8026800) Minden, Nev.: Bently-Nevada Co., July, 1981.

35. Parkinson, A. G. "Balancing of Flexible Rotors," in Dynamics of Rotors, op. cit., pp. 413-435.

36. Parkinson, A. G., and Bishop, R. E. D. "Residual Vibration in Modal Balancing," J. Mech. Engng. Sci., 7, no. 1(1965).

37. Roark, R. J., and Young, W. C. Formulas for Stress and Strain. 5th edition. New York: McGraw-Hill, 1975.

38. Salamone, D. J., and Gunter, E. J. "Synchronous Unbalance Response of an Overhung Rotor with Disk Skew," Engineering for Power, 102:4(1960), pp. 749-755. Reprinted in "Rotor Dynamics & Rotor-Bearing Course Notes," op. cit., sect. 4:8.

39. Schweitzer, G. "Stabalization of Self-Excited Rotor Vibrations by an Active Damper," in Dynamics of Rotors, op. cit., pp. 472-493.

40. Simpson, J. W. "Vibration Analysis of a Superconducting Generator Rotor on Flexible Supports." Master's thesis, MIT, June, 1982.

41. Smith, J. L., et al. "Superconductors in Large Synchronous Machines." Final Report for the Electric Power Research Inst., Research Project 92-2, Sept. 1975.

42. Tepper, K. A. "Mechanical Design of the Rotor of a Fault-Worthy 10-MVA Superconducting Generator." Ph. D. thesis, MIT, Sept., 1980.

43. Tessarzik, J. M., Badgley, R. H., and Anderson, W. J. "Flexible Roter Balancing by the Exact Point-Speed Influence Coefficient Method." ASME paper 71-Vibr-91, Vibration Conference, Toronto, Ontario, 1971.

44. Tessarzik, J. M., Badgley, R. H., and Fleming, D. P. "Experimental Evaluation of Multiplane-Multispeed Rotor Balancing through Multiple Critical Speeds." ASME paper 75-DET-73, Design Engineering Technical Conference, Washington, D. C., Sept., 1975.

45. Tessarzik, J. M., Chiang, T., and Badgley, R. H. "Suppression of Rotor-Bearing System Vibrations through Flexible Bearing Support Damping." ASME paper 75-DET-117, Design Engineering Technology Conference, Washington, D. C., Sept., 1975.

46. Tonneson, J. "Further Experiments on Balancing of a High-Speed Flexible Rotor," ASME paper 73-Det-99, Design Engineering Technical Conference, Cincinnati, Ohio, 1973

47. Wolf, J. A., Jr. "Whirl Dynamics of a Rotor Partially Filled with Liquid," Trans. ASME, J. Appl. Mechs., 35(1968), pp. 676-682.